

# Spatial Filtering for Scale Bridging and Its Application to Transport in Dense Particle Beds

Stefan Radl<sup>1</sup>, Federico Municchi

Institute of Process and Particle Engineering, Graz University of Technology, Graz, Austria

<sup>1</sup>Corresponding author: e-mail address: radl@tugraz.at

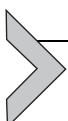
## Contents

1. Introduction and Trends	154
1.1 Filtering as Strategy for Scale Bridging	154
1.2 Hierarchy of Models and Their Connection	156
1.3 Computational Strategies for Solving the Model Equations	160
1.4 Aspects From Data Science	164
2. Mathematical Formulation	165
2.1 Euler–Euler Models	165
2.2 Euler–Lagrange Models	165
2.3 Governing Equations for Momentum Transport	168
2.4 Governing Equations for Scalar Transport in the Continuous Phase	172
2.5 Closure Laws Required at the Mesolevel	174
2.6 Closure Laws Required at the Macrolevel	179
3. Algorithmic Aspects	183
3.1 Flow Simulators	183
3.2 Filtering Tools	185
4. Verification Strategies	191
4.1 Verification Strategy for Filtering Tools	191
4.2 Selected Verification Cases for Benchmarking Particle-Resolved DNS	192
5. Recent Developments for Closures Describing Transfer Rates in Mesoscale Models	198
5.1 Effects Due to Differences in the Mean Particle Speed: The Fluid-Mediated Particle–Particle Drag	198
5.2 Effects Due to Particle Agitation	199
5.3 Cross Effects	199
5.4 Variability of the Exchange Coefficients	200
5.5 Wall Effects	203
6. Recent Developments for Closures Describing Mesoscale Phenomena	209
6.1 Sequential Fluid and Particle Coarsening	210
6.2 Non-Boussinesq Stress Models	212

6.3	Closures for Cohesive Systems	212
6.4	Closures Based on a Deconvolution Approach	214
7.	Conclusion and Outlook	215
7.1	Research Direction 1: Advanced Euler–Lagrange Models	217
7.2	Research Direction 2: Broader Application of Filtering Tools	217
7.3	Research Direction 3: Exploration of Intraparticle Transport Phenomena	219
Acknowledgments		220
Appendix. Derivation of an Euler–Lagrange Theory of Dispersed Multiphase Flows		220
A.1	Definitions and basic results	221
A.2	Derivation of the volume-averaged governing equations	223
A.3	Approximations of the volume-averaged governing equations	228
References		229

## Abstract

The method of spatial filtering as a universal approach to support closure development for models of dense fluid–particle systems is presented. Starting from a set of governing equations, an overview of closures that are required at different levels of a model hierarchy is provided. A focus is on closures to be used in mesoscale models, highlighting recent developments that aim at the description of the variability of exchange coefficients, as well as wall effects. Furthermore, attempts to describe the anisotropy of mesoscale stresses, as well as the effect of cohesive particle–particle interactions in the context of macroscale models are summarized. Computational aspects, together with selected verification cases are documented to stimulate a broader use of the filtering approach. Finally, three future research directions that appear most fruitful are outlined. These final thoughts may help to establish more reliable and robust multiphase flow models for reactive systems.



## 1. INTRODUCTION AND TRENDS

### 1.1 Filtering as Strategy for Scale Bridging

Efforts to model the performance of chemical reactors have taken a turn once detailed flow models became available: nowadays, modelling and simulation of flow plays a central role in the development of equipment in the chemical industry, being an integral part of many roadmaps and perspectives (2017). This is especially true for dense fluid–particle flows that are in the focus of this chapter. Such multiphase flows are central to many industrial applications such as (i) the wide range of processes that rely on fluidization, (ii) packed bed reactors, (iii) solids handling and conveying, or (iv) particle fractionation and separation to name just a few examples.

Certainly, the influential perspective of Sundaresan was an eye-opener for many researchers and resulted in a number of breakthrough papers in

the field of chemical engineering and fluid mechanics (Sundaresan, 2000). Key statements in this perspective—e.g., related to the fact that “...work is under way in several research groups to include the effect of particle-size distribution...”—are still valid today. It stresses the fact that differences in particle size—on the first view a trivial twist in the parameters that describe a gas–particle system—add significant complexity when attempting to model transport phenomena in dense particulate systems. This is an addition to complex flow structures that arise spontaneously due the inherent instability of the fluidized state (Fullmer and Hrenya, 2017): an ensemble of homogeneously dispersed particles will spontaneously form clusters when allowed to sediment freely. Thus, one has to generally except that particles in relevant flow situations have a spatially nonuniform distribution (this is even the case in packed beds!). This is the exact reason why spatial averaging over a region with a certain size (or “filtering”) plays such an important role for these multiphase flows: in order to arrive at a meaningful description, one must deeply appreciate the difference between local and average quantities.

Since the mathematics behind spatial averaging has been summarized quite extensively (Whitaker, 1999), it appears that little needs to be said about how to apply filtering in the field of chemical engineering. Unfortunately, the opposite is true: filtering has attracted renewed interest in the wake of a specific type of flow simulations: large-scale Euler–Lagrange (EL) simulations of dense gas–particle flows became increasingly fashionable over the past 5 years (Capelatro and Desjardins, 2013; Radl and Sundaresan, 2014). Adopting the EL strategy over the commonly used Euler–Euler approach (EE; often also called “two-fluid model,”) appears to be a trivial modification. But this is not the case, as can be shown by two important facts:

- (i) EL models necessitate closures on a per-particle level, while EE models are based on closures that describe ensemble-average quantities and
- (ii) EL models enable simulations of cohesive systems, and systems in which intraparticle transport processes play a central role.

Next, a brief description of the hierarchy of models is introduced in Section 1.2. Closures derived by filtering can be classified within this hierarchy. One could call models that are based on such a hierarchy “multiscale models” (van der Hoef et al., 2008). Since the exact definition of “multiscale” differs between different authors, and is largely irrelevant for the present contribution, this wording is dropped in what follows—it is enough to accept that filtering is a universal strategy that can be used to connect models at various levels of the hierarchy introduced in Section 1.2. In Section 1.3, an outline of the computational techniques often employed in the solution of these models is provided.

Data science challenges arising from filtering operations are briefly discussed in [Section 1.4](#).

The remaining of this chapter is structured as follows: [Section 2](#) summarizes models, as well as the most relevant types of closures laws that are employed to describe dense gas–particle suspensions. [Section 3](#) discusses some algorithmic aspects with a focus on postprocessing tools for spatial averaging. [Section 4](#) is dedicated to ideas on how to verify the implementation of such algorithms. In [Sections 5 and 6](#) recent developments in the field of mesoscale models are summarized. Specifically, a reflection on newly proposed closure laws that are required as input to these models, as well as closures that can be developed on the basis of such models is provided. [Section 7](#) completes this chapter with a conclusion and an outlook.

## 1.2 Hierarchy of Models and Their Connection

### 1.2.1 Chemistry and Material Models

An overview of models used in typical simulations of reactive gas–particle suspension flows is provided in [Fig. 1](#). First, an essential classification must be made, specifically in (i) chemistry and materials models, as well as (ii) multiphase flow models. For the description of models in category (i) a unified nomenclature was recently developed ([de Baas and Rosso, 2015](#)). These models

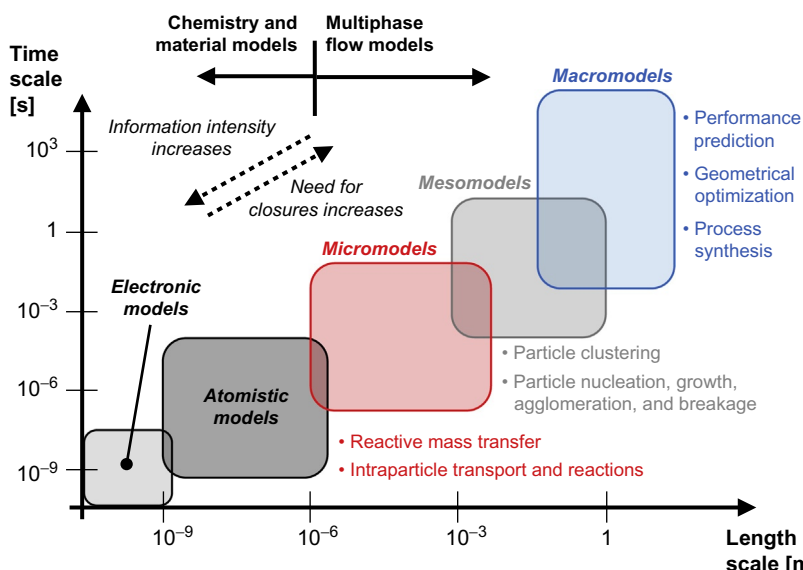


**Fig. 1** Overview of models used in typical reactive fluid–particle flow applications categorized by a typical time and length scale.

describe phenomena occurring on a subatom to a super-molecular scale, and hence are predominantly used by chemists and physicists. Chemistry and material models can be subcategorized into (a) electronic, (b) atomistic, (c) mesoscopic,<sup>a</sup> as well as (d) continuum models (for clarity, subcategories c and d are not indicated in Fig. 1). A classical application of electronic and atomistic models is the development of reaction mechanisms and associated kinetics. Thus, the result of simulations using these models is an understanding of how chemical reactions proceed, which typically includes reaction stoichiometry, reaction enthalpies, and rate laws. Another application is the direct simulation of diffusion via atomistic models, e.g., tracking the motion of a molecule in a matrix consisting of other molecules.

### 1.2.2 Flow Models

Multiphase flow models are built on top of materials models, and use the *output* of chemistry and material property models to close the governing equations. An overview of relevant applications of flow models was provided recently by Pannala et al. (2011).

Multiphase flow models typically follow a less strict nomenclature as that introduced for chemistry and material models (de Baas and Rosso, 2015). In most cases, flow models are categorized based on the size of the phenomena they describe (Padding, 2013). For example, the NanoSim project (2017) adopted a nomenclature that relied on the name of a typical item (e.g., a particle) to define a model (see Fig. 2).

Even simpler definitions are widely used in the context of fluid–particle systems, often leading to confusion. For example, the process model categories introduced by Padding (2013) are based on the assumption that atoms are the smallest entities. However, when describing suspension flows in engineering applications, it would be more natural to consider particles as being the smallest entities. When following such an engineering concept, the following categories of models are typically used, a wording which is also adopted in the present work:

- (1) “Micro”(scale) models are concerned with phenomena that happen on a subparticle or particle scale. The publications of Khinast and coworkers (Lekhal et al., 2001a, b) dealing with drying of particles (i.e., intraparticle transport of heat and mass) are a prime example of such models. Another example in the same category is the large body of direct numerical

<sup>a</sup> Not to be confused with the wording “mesoscale models” (Fox, 2012), a wording that is adapted in what follows for flow models.

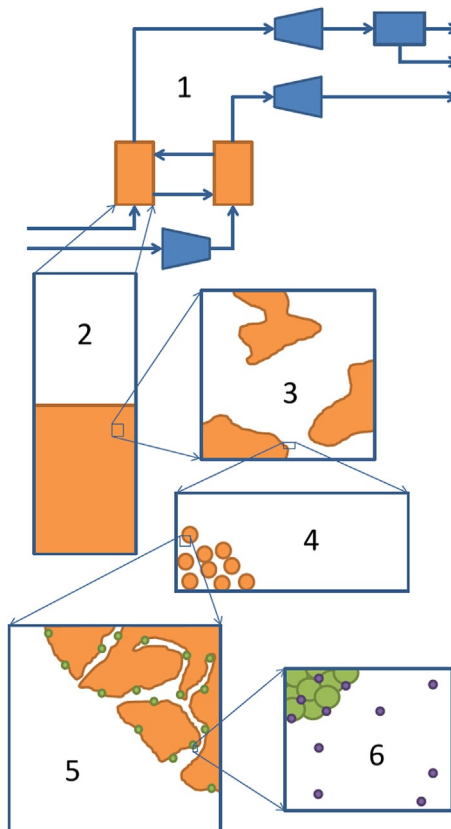


**Fig. 2** An example for the definition of a multiscale model in the context of process models (this definition was developed during the NanoSim project (2017) and distinguishes six scales: (1) system scale, (2) equipment scale, (3) cluster scale, (4) particle scale, (5) intraparticle pore scale, and (6) atomistic scale. *Figure adapted from NanoSim—a multiscale simulation-based design platform for cost-effective CO<sub>2</sub> capture processes using nano-structured materials (Annex I—Description of work). Trondheim, Norway, 2013.*

simulation (DNS) models that have been used to predict fluid–particle transfer rates of momentum, heat, and mass (Deen and Kuipers, 2014a; Feng and Michaelides, 2009; Municchi and Radl, 2017; Sun et al., 2015). Most “microscale” models do not allow particles to move (Holloway et al., 2012; Lekhal et al., 2001a), e.g., transport phenomena within a particle are separated from the particle’s convective transport. However, some studies assign a specific speed to individual particles, but freeze their relative position (Holloway et al., 2010), or allow particles to

move freely in order to capture effects due to either (i) the perturbed microstructure or (ii) the inhomogeneous distribution of the particles in the computational domain (Derksen, 2014b; Derksen and Sundaresan, 2007; Uhlmann and Doychev, 2014).

- (2) “*Meso*”(scale) models describe phenomena on intermediate scales. In the context of particulate systems this includes phenomena that are governed by the behavior of an *ensemble* of particles (Fox, 2012, 2017). A well-known example of a mesoscale model is the celebrated Boltzmann equation to describe the evolution of a particle cloud in space, time, and velocity coordinates. For fluid–particle systems involving particles that are allowed to change their properties—also referred to as particle-internal coordinates, e.g., size, density—the so-called generalized population balance equation is the relevant mesoscale model for the particle phase (Fox, 2012). The core variable that describes this mesoscale model is the number density function (NDF). This model can be solved by a variety of solution strategies, e.g., a moment-based (Eulerian) method or a Lagrangian method that approximates the NDF with a finite number of computational parcels (i.e., “packages of particles”). The latter strategy typically requires tracking a large number of particles or parcels. An idea is to exploit Graphic Processing Units (GPUs) to reduce the computation time when using a Lagrangian method (Radeke et al., 2010; Radl et al., 2011) to evaluate a mesoscale model.
- (3) “*Macro*”(scale) models aim on describing phenomena that occur on an equipment scale. Often, such models may even describe a whole system (e.g., a connection of mixers, splitter, reactors, and separators). Thus, they aim on picturing effects that originate from the connectivity of multiple pieces of process equipment. While the governing equations that define such macroscale flow models are meanwhile established (Schneiderbauer, 2017), fundamental questions still remain how to formulate physically realistic closures for these equations. This is especially true for reactive systems in which closures for average heat (Lane et al., 2016) and species transport, as well as the consumption/production rate of chemically reacting species must be considered (Agrawal et al., 2013; Holloway and Sundaresan, 2012). The adaptation of these closures in models is slow, and only recently first steps have been made to build rigorous macromodels for reactive systems (Zhu et al., 2016). Macro-scale flow models for polydisperse systems are equally challenging, and only the subgroup of bidisperse systems has been analyzed so far in greater detail (Holloway and Sundaresan, 2014; Holloway et al., 2011).

### 1.2.3 Connection of Models

There is a key need for the connection of individual simulation tools, a fact that is now widely accepted by different research communities ([Rantanen and Khinast, 2015](#)). Such connection tools should mainly stimulate the convergence of disciplines (e.g., pharmaceutical science and engineering), and hence their main task is to provide a single “language” for information and knowledge exchange. Simulation tools—together with such “connectors”—then define a unified simulation framework with the vision to concertize efforts of researchers that use different tools. A popular example of such a framework is KNIME ([Berthold et al., 2008](#)), which uses a graphical interface to document workflows that connect a large variety of simulators and tools. Also, the framework tool “Porto” ([Hagelien et al., 2015](#)) has followed similar ideas. Most relevant for the present text is the tool CPPPO ([Municchi et al., 2016](#)), which realizes highly efficient spatial averaging of field data to support researchers during closure development. Next, an attempt to summarize computational solution strategies for solving the underlying model equations is made. This is done to illustrate the sources of data which are available to connection tools.

## 1.3 Computational Strategies for Solving the Model Equations

Based on a well-established set of equations that describe the motion of fluids and particles (see [Section 2](#)), a large array of computational strategies has been developed for their solution. The key challenge when evaluating the model equations is to consider the interaction of a large number of discrete entities (i.e., the particles) with a fluid (and vice versa), as well as with themselves. This requires thoughts on how to solve a large system of equations efficiently. Traditionally, an Euler–Euler (EE)-based description was followed ([Anderson and Jackson, 1967](#)), and this type of models is still under active development. However, a general trend toward an Euler–Lagrange (EL)-based description is observable. This is certainly motivated by the need to account for variable particle properties that are of central importance for chemical engineering applications, as well as polydisperse flows in a much wider context.

[Table 1](#) provides a summary of the most significant developments in computational strategies to solve EE and EL models. A clear focus is thereby on Euler–Lagrange methods. It is important to note that these computational approaches can be used at different levels of the model hierarchy detailed in [Section 1.2](#).

**Table 1** Overview of Computational Approaches for Simulating Fluid–Particle Flows

Approach and Representative Publication(s)	Particle (or Parcel) Collision Tracking	Enduring Contact Treatment	(Short) Collision Treatment	Particle–Turbulence Interaction	Advantages and Drawbacks
1. Euler–Euler approach (Anderson and Jackson, 1967; Desjardins et al., 2008; Ding and Gidaspow, 1990; Fox, 2008; Iddir and Arastoopour, 2005; Jackson, 2000; Kong and Fox, 2017; Kong et al., 2017; Passalacqua and Fox, 2011; Schneiderbauer et al., 2012b; Yuan and Fox, 2011)	—	Mature “frictional” models, no rolling, cohesion in principle possible	Yes, KTGF-based	Yes	+ widely applicable + mature numerical models – treatment of particle-based properties (size, composition) adds significant complexity
2. Euler–Lagrange: Parcel-based, no parcel collision tracking (e.g., MP-PIC, DDPM) (Cloete et al., 2012; Popoff and Braun, 2007; Rourke and Snider, 2014; Snider, 2001)	No	Heuristic particle pressure terms (friction is challenging), no rolling, no cohesion	Yes, Heuristic or KTGF-based	No	+ adding particle-based properties is easy – poor performance for extremely dense flows
3. Euler–Lagrange: Parcel-based with statistical parcel collision tracking (Sommerfeld, 2003)	Yes, but only statistical	No	Yes, using “virtual particles”	Yes, but only fluid-to-particle	+ adding particle-based properties is easy – poor performance for moderately dense flows
4. Euler–Lagrange: Parcel-based with parcel collision tracking (e.g., “DPM”) (Bierwisch et al., 2009; Patankar and Joseph, 2001; Radl et al., 2011; Sakai and Koshizuka, 2009)	Yes	Yes, rolling and cohesion in principle possible	Yes, but poor performance	No	+ adding particle-based properties is easy – parcel collisions in dilute flows are challenging

*Continued*

**Table 1** Overview of Computational Approaches for Simulating Fluid–Particle Flows—cont'd

Approach and Representative Publication(s)	Particle (or Parcel)		(Short) Collision Treatment	Particle–Turbulence Interaction	Advantages and Drawbacks
	Collision Tracking	Enduring Contact Treatment			
5. Euler–Lagrange: Particle collision tracking, fluid flow is not resolved <a href="#">(Capecelatro and Desjardins, 2013; Capecelatro et al., 2014; Girardi et al., 2016; Goniva et al., 2012; Jajcevic et al., 2013; Kloss et al., 2012; Oschmann et al., 2016; Radl and Sundaresan, 2014; Wu et al., 2017)</a>	Yes	Yes, rolling and cohesion models	Yes, direct	Yes	+ widely applicable + direct consideration of particle-based properties (intraparticle profiles can be considered) – closures at the particle level required, which are not well developed – high computational cost
6. Euler–Lagrange: Particle collision tracking, fluid flow is resolved <a href="#">(Deen and Kuipers, 2014a, b; Derkx and Sundaresan, 2007; Schmidt and Nikrityuk, 2012)</a>	Yes	Yes, rolling and cohesion models	Yes, direct	Yes	+ direct calculation of fluid–particle transfer (momentum, heat, mass, etc.) + appealing for nonspherical particles + direct consideration of particle-based properties (intraparticle profiles can be considered) – extremely high computational cost

7. Lagrangian: Parcel-based using per-parcel stress description (“Stress-based DEM”, SDEM) <a href="#">(Egholm, 2007; Egholm et al., 2007)</a>	Yes	Yes, via constitutive laws	No	No	+ dense flows + adding particle-based properties is easy – currently no second phase
8. Lagrangian: Parcel-based using Smoothed Particle Hydrodynamics <a href="#">(Xiong et al., 2011; Yuu and Umekage, 2008)</a>	No	Constitutive law	No	No	+ dense flows + adding particle-based properties is easy – collisions in dilute flows are challenging
9. Euler–Euler/Euler–Lagrange Hybrid <a href="#">(Pirker et al., 2009; Schellander et al., 2013; Schneiderbauer et al., 2016)</a>	No (only test particles)	Same as Euler–Euler approach	Similar to Euler–Euler approach	Yes	+ lower computational cost compared to Euler–Lagrange based approach + adding particle-based properties is easy – complex implementation – limited applicability so far

## 1.4 Aspects From Data Science

Filtering is connected to the manipulation of a large amount of data, and hence it is instructive to consider aspects from data science. Beck et al. (2016) provide an interesting perspective on how to exploit tools from the field of data science in chemical engineering applications. In the context of particle technology applications, the main drivers for such thoughts are the latest developments in the field of (i) particle flow simulators, as well as (ii) imaging techniques (e.g., optical, MRI, or micro CT). These developments lead to an explosion of the available data volume. For example, considering the increasing availability of computational resources, the amount of data generated by simulators (in case dumped to disk in its full extend) would—by far—surpass current resources for data storage. This necessitates deeper thoughts on how to efficiently filter (both temporally and spatially) data, a need that goes beyond calculating simple running averages.

An example of such advanced data analysis, which is of key relevance in the context of the present contribution, is the work of Igci et al. (2008). This work highlighted for the first time the importance of sophisticated data analysis, namely, the consideration of the effect of filter size on spatially averaged statistics. These ideas have also been followed by other groups (Ozel et al., 2013; Parmentier et al., 2011), establishing a new level of physical insight with respect to phenomena that need to be modeled. Considering the sheer amount of data needed to build a comprehensive closure, for example, the effective drag force experienced by a clustered suspension (Radl and Sundaresan, 2014), such data analysis is preferably performed *during* a simulation run. This need is also illustrated by more recent simulations which incorporate more than  $30 \times 10^6$  particles in a single simulation (Capecelatro et al., 2014; Ozel et al., 2016).

An additional thought is related to the interpretation of the large amount of data collected with, for example, detailed suspension flow simulations. Clearly, there is a need to formalize the workflow for such an interpretation in order to automate it to a certain degree. Literature indicates that in other areas such “workflow tools” already exist: for example, KNIME (Berthold et al., 2008) is extensively used in the pharmaceutical industry to define workflows for, e.g., data reading, analysis, and report generation. Similarly, machine learning tools, e.g., Tensorflow (Abadi et al., 2015), are used with increasing frequency to extract knowledge from data.



## 2. MATHEMATICAL FORMULATION

### 2.1 Euler–Euler Models

Euler–Euler (EE) models describe both the fluid and the particulate phase with transport equations on a globally fixed coordinate system—particles are not tracked in space and time. Instead, the distribution of particle phase properties (e.g., speed, size, composition, etc.) is considered.

The accurate solution of Euler–Euler models for polydisperse suspension flow ([Marchisio and Fox, 2013](#)) is still a subject of mathematical research. The reason is that including internal particle coordinates (e.g., the size, density, or moisture content) adds one (or more) dimensions to the governing equations. This leads to a mathematical challenge that is typically not solved directly, but rather simplified first and then solved (e.g., using moment-based methods; [Fox, 2017](#)).

A much more straightforward route (in the context of EE models) can be taken in case one accepts the validity of a mono-sized particle population, where only average particle speeds and the granular temperature are used to describe the true particle velocity distribution ([Ding and Gidaspow, 1990](#); [Gidaspow, 1994](#)). In this case, the governing equations that define such EE models ([Anderson and Jackson, 1967](#)) are comparably easy to solve. Despite those assumptions, EE models are already able to model mesoscale phenomena, e.g., clustering in fluidized beds.

From the perspective of a chemical engineer interested in reacting suspensions, EE models currently impose a key limitation: intraparticle transport phenomena need to be approximated ([Stark et al., 2016](#); [Wurzenberger et al., 2002](#)). This is less attractive for rigorous simulations of transport in a variety of reactive systems that are dominated by such intraparticle effects.

### 2.2 Euler–Lagrange Models

EL models are based on the idea that for each phase the most natural description is chosen: particle motion is described by a Lagrangian approach that tracks each entity individually (either a particle or a parcel), and fluid motion (i.e., the motion of the continuous phase) is described by an Eulerian approach.

For suspensions relevant in this chapter (featuring particle volume fractions up to the close packing limit), the DEM (or “soft-sphere” approach) is employed to track particles and evaluate their interaction. This is motivated

by the ability to model enduring particle–particle collisions. For modelling the interaction of the particles with the fluid phase, two modelling approaches exist: (i) particle-resolved EL models and (ii) particle-unresolved EL models.

### 2.2.1 Particle-Resolved EL Models

These models are EL-based and designed to predict the details of the flow near the fluid–particle interface. These models are discussed in greater detail in [Sections 2.3.1 and 2.4.1](#). These “particle-resolved” (PR) models necessitate significant computational resources to predict the flow since the domain occupied by the fluid phase is discretized into control volumes that are much smaller than the particles (see left panel of [Fig. 3](#)). The use of PR-EL models is justified in case one of the following ideas is followed:

- (i) In case one aims on deriving closure models for, for example, forces acting on individual particles ([Beetstra et al., 2007](#); [Municchi and Radl, 2017](#)).
- (ii) In case no suitable closure model (e.g., to predict the force acting on a particle) for the particle-unresolved (PU) approach (see [Section 2.2.2](#)) exists. This is typically the case when nonspherical and/or deformable particles are involved, or the flow is confined by walls. Examples for the latter include the flow in microchannels ([Di Carlo et al., 2009](#)).

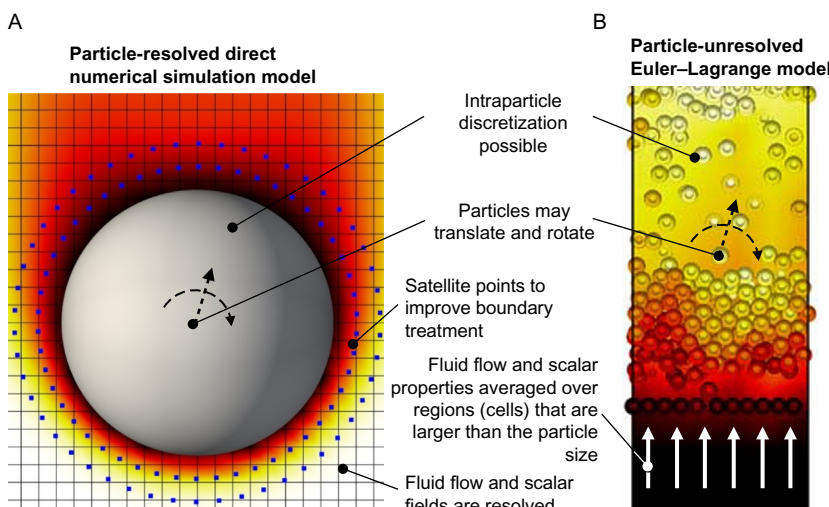


**Fig. 3** Idea behind a “particle-resolved” (PR)-EL model that aims on predicting flow details in the void space of a suspension (left panel), as well as concept of a “particle-unresolved” (PU)-EL model (right panel; colors indicate the distribution of a transported scalar quantity, e.g., the temperature).

- (iii) In case the details of fluid flow significantly affect the behavior of the suspension, and a PU-EL approach would yield unreliable results. This is typically the case for suspensions in which the fluid-to-particle density ratio is in the order of unity or larger. Examples are liquid–particle suspensions, emulsions, or bubbly flows.
- (iv) In case one is interested in the dispersion of small particles in a strongly polydisperse system. This is because small particles will mainly follow the flow around larger particles, necessitating a detailed description of fluid flow in the void space. An example is the modelling of filtration processes (Kolakaluri, 2013; Kolakaluri et al., 2015). Similarly, in case one is interested in how quickly a scalar quantity (e.g., a dissolved substance) is dispersed in the continuous phase of a suspension (Derksen, 2008b), one will favor a PR-EL approach.

## 2.2.2 Particle-Unresolved EL Models

These models are a simplification, where only spatially averaged transport equations for the continuous phase are solved (see right panel of Fig. 3, as well as Fig. 4). While drastically reducing the demand of computational resources to solve the governing equations, PU-EL-based models have lower predictive capabilities. Fortunately, for most systems the adoption of a PU-EL approach is still appropriate. For example, in gas–particle flows the inertia of the continuous phase (i.e., the gas) is negligible compared to that of the particles (an example is a recent work that benchmarked data

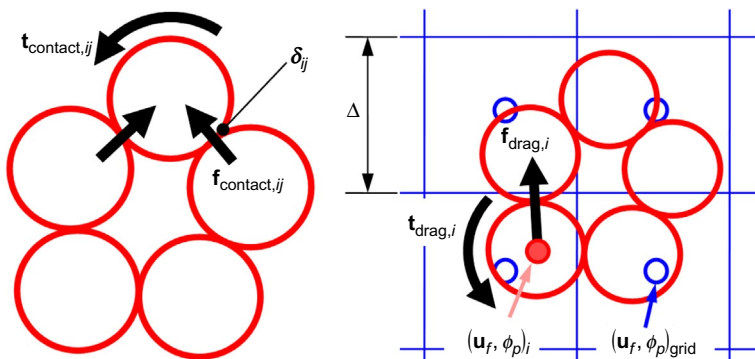


**Fig. 4** Idea behind a PU-EL model using the DEM as the Lagrangian submodel (left panel: illustration of contact force and torque calculation; right panel: illustration of the computational Eulerian grid in blue, as well as particle-based force and torque calculation;  $t$  is a torque,  $f$  is a force,  $\delta$  is an overlap,  $u$  is a velocity,  $\Delta$  is a distance, and  $\phi$  is a volume fraction).

originating from PU-EL and PR-EL for dilute suspensions; [Horwitz et al., 2016](#)). Hence, small-scale fluid velocity fluctuations (that are not directly resolved in PU-EL, but may be modeled) do not critically affect the overall system behavior. Finally, it should be mentioned that often a PU-EL is chosen, simply due to computational limitations, and limited predictive capabilities are accepted.

## 2.3 Governing Equations for Momentum Transport

The governing equations are derived from basic balance equations of mass, momentum, and a scalar quantity (for a rigorous discussion see the [Appendix](#): note that the indication of average quantities is different in this appendix since two levels of spatial averaging are performed in what follows). In particular, in the following equations for the momentum transport in the fluid and particulate phase are summarized, together with the equations for mass conservation in an incompressible fluid. Transport equations of scalar quantities are discussed in [Section 2.4](#).

### 2.3.1 Continuous Phase: Particle-Resolved Approach

Adopting the PR-EL approach the original form of the Navier–Stokes equations for the description of the fluid motion can be used. In the following description, the fluid is assumed to be incompressible having a constant dynamic viscosity  $\mu$ . The transport equations for mass conservation and the acceleration of the fluid can then be formulated as:

$$\nabla \cdot \mathbf{u}^\circ = 0 \quad (1)$$

$$\rho_f [\partial_t \mathbf{u}^\circ + \nabla \cdot (\mathbf{u}^\circ \mathbf{u}^\circ)] = -\nabla p^\circ + \mu \nabla^2 \mathbf{u}^\circ + \rho_f \mathbf{g} + \mathbf{F}^\Omega \quad (2)$$

Here,  $\rho$ ,  $\mu$ ,  $\mathbf{g}$ ,  $p$ , and  $\mathbf{u}$  are the fluid density, dynamic viscosity, gravity, pressure, as well as the fluid velocity, respectively.  $\mathbf{F}^\Omega$  is a volumetric boundary forcing term that is used in some formulations, e.g., when adopting the immersed boundary method (IBM) to solve this transport equation ([Municchi and Radl, 2017](#)). The superscript circle in Eqs. (1) and (2) indicates point variables (i.e., they are not averaged, but local in the sense of the continuum hypothesis), to distinguish them from their local mean counterparts introduced in [Section 2.3.2](#).

In case Eqs. (1) and (2) are solved directly (i.e., all details of the spatio-temporal evolution of the flow are resolved), the approach is called PR-direct numerical simulation (PR-DNS). For cases of particle-resolved simulations characterized by very large Reynolds numbers, turbulence

models to close the stress in the momentum transport equation might be adopted (Dixon, 2017). Despite being resolved on the particle level, those cannot be called DNS, since not all details of the flow are resolved.

### 2.3.2 Continuous Phase: Particle-Unresolved Approach

The following set of governing equations is obtained by replacing point variables as introduced in the PR-EL approach (i.e., the variables used in Section 2.3.1) by local mean variables obtained from an averaging operation. A complete description of this averaging operation can be found in standard texts (Anderson and Jackson, 1967) and is illustrated with equations in Appendix. It is to highlight, that this averaging operation, while similar in its concept, is different from the spatial filtering operation discussed in Section 2.3.5. Thus, local mean variables and filtered quantities shall not be confused. Again, as for the PR-EL approach, the fluid is assumed to be incompressible having a constant dynamic viscosity  $\mu$ . The resulting set of equations for local mean flow quantities reads:

$$\partial_t \phi_f + \nabla \cdot (\phi_f \mathbf{u}) = 0, \quad (3)$$

$$\rho_f \left[ \partial_t (\phi_f \mathbf{u}) + \nabla \cdot (\phi_f \mathbf{u} \mathbf{u}) \right] = -\nabla p + \nabla \cdot \boldsymbol{\tau}_f + \varphi_f \rho_f \mathbf{g} + \boldsymbol{\Phi}_{p \rightarrow f}. \quad (4)$$

Here,  $\phi$  is a volume fraction, and  $\boldsymbol{\tau}$  is a stress tensor. Subscript  $f$  denotes the fluid phase, and subscript  $p$  denotes the particulate phase. The total particle–fluid interaction force per unit volume of the suspension, i.e.,  $\boldsymbol{\Phi}_{p \rightarrow f}$  can be decomposed into a number of force components. The most natural and often adopted choice of decomposition for fluid–particle systems is (i) a generalized buoyancy term, as well as (ii) a drag term. Introducing this decomposition can result to a formulation differing from the above momentum transport equation (Zhou et al., 2010), which is, however, equivalent to Eq. (4). This decomposition is discussed in Section 2.5.1.

The volumetric total particle–fluid interaction force  $\boldsymbol{\Phi}_{p \rightarrow f}$  must be modeled due to the description of momentum transport via local mean variables. Typically, an approach that uses a weighted sum of particle–fluid forces  $\mathbf{f}_{p \rightarrow f}$  acting on a set of particles within a computational cell is adopted. Specifically, one may use:

$$\boldsymbol{\Phi}_{p \rightarrow f, j} = \frac{1}{V_{\text{cell}, j}} \sum_{i \in V_{\text{cell}, j}} w_{ij} \mathbf{f}_{p \rightarrow f, i}. \quad (5)$$

Here,  $V_{\text{cell}, j}$  is the volume of the computational cell  $j$ ,  $i$  is the particle index, and  $w_{ij}$  is a weighting function.

### 2.3.3 Dispersed Phase: Eulerian Description

The fidelity of models for dispersed-phase momentum transport has recently undergone a number of improvements, where the most commonly used formulations are summarized below. The interested reader is referred to the work of Schneiderbauer et al. or Kong and coworkers for a more rigorous formulation (Kong and Fox, 2017; Kong et al., 2017; Schneiderbauer et al., 2012b).

$$\partial_t \varphi_p + \nabla \cdot (\varphi_p \mathbf{v}) = 0 \quad (6)$$

$$\rho_p \left[ \partial_t (\varphi_p \mathbf{v}) + \nabla \cdot (\varphi_p \mathbf{v} \mathbf{v}) \right] = -\varphi_p \nabla p + \nabla \cdot \boldsymbol{\tau}_p + \varphi_p \rho_p \mathbf{g} - \boldsymbol{\Phi}_d \quad (7)$$

Here,  $\mathbf{v}$  is the particle speed, which in this case is a local quantity in the sense of the continuum hypothesis. Note, that in the above equation only the drag component  $\boldsymbol{\Phi}_d$  of the total particle–fluid interaction force  $\boldsymbol{\Phi}_{p \rightarrow f}$  was used. The remaining buoyancy contribution is shown as the first term on the right hand side of Eq. (7). The particle–phase stress tensor  $\boldsymbol{\tau}_p$  used in the above equation must be closed. This is typically done by decomposing it into a kinetic theory-based and frictional contribution (Schneiderbauer et al., 2012b).

An important and often neglected detail when solving the above momentum transport equation is the boundary condition imposed at a wall. The study of Cloete et al. (2016) summarizes recent progress in this field. Specifically, this study suggests that the more rigorous closures for wall treatment derived by Schneiderbauer et al. (2012a) should be used. This removes the need for adjusting the specularity coefficient in the more commonly applied (but less rigorous) set of boundary conditions (Johnson and Jackson, 1987).

### 2.3.4 Dispersed Phase: Lagrangian Description

#### 2.3.4.1 Translational Motion

Assuming a constant particle mass  $m$ , the governing equation for particle motion, i.e., Newton’s equations of motion, reduces to the following ordinary differential equation for each particle  $i$ :

$$m_i d_t \mathbf{v}_i = \sum_j \mathbf{f}_{j,i} \quad (8)$$

The remaining challenge is to close all forces  $\mathbf{f}_{j,i}$  that originate from different physical phenomena  $j$ . In parallel to the above evolution equation for the particle speed, the particle position needs to be updated:

$$d_t \mathbf{x}_i = \mathbf{v}_i \quad (9)$$

### 2.3.4.2 Rotational Motion

The balance of angular momentum requires that (in a global coordinate system):

$$d_t (\mathbf{I}_i \cdot \boldsymbol{\omega}_i) = \sum_j \mathbf{t}_{j,i} \quad (10)$$

The torque  $\mathbf{t}_{j,i}$  originating from various physical phenomena must be closed, which may benefit from the already known forces  $\mathbf{f}_{j,i}$ . The moment of inertia tensor  $\mathbf{I}_i$  simplifies to an identity tensor for spherical particles, and hence can be pulled out of the time derivative in Eq. (10) for such simplified systems. Consequently, the above ordinary differential equation can be solved similar to that for translational motion.

However, an important note must be made with respect to Eq. (10): this equation is still valid, but less useful for nonspherical particles. This is since the tensor  $\mathbf{I}_i$  characterizing the moment of inertia becomes time dependent in the global coordinate system. It is hence more convenient to track rotational particle motion in a frame of reference that is aligned with the (current) principal axes of inertia of each particle. In such a reference frame the moment of inertia tensor ( $\mathbf{I}'_i$ ) is constant and diagonal. Therefore, one can exploit the following expression to relate time derivatives in a global and a body-fixed frame of reference:

$$d_t ()|_{\text{global}} = d_{t'} ()|_{\text{body}} + \boldsymbol{\omega}'_i \times () \quad (11)$$

Here the prime indicates quantities in the particle's frame of reference. Under the above assumption that the body frame of reference is aligned with the principal axes, one arrives at the celebrated Euler equations (Fan and Ahmadi, 1995):

$$\mathbf{I}'_i \cdot d_{t'} (\boldsymbol{\omega}'_i) + \boldsymbol{\omega}'_i \times (\mathbf{I}'_i \cdot \boldsymbol{\omega}'_i) = \sum_j \mathbf{t}'_{j,i} \quad (12)$$

This ordinary differential equation can be integrated in time in a straightforward manner. It remains to update the angular position of the particle,

which is achieved most efficiently by time integration schemes that rely on quaternions (Lu et al., 2015).

### 2.3.5 Transport Equations for Macroscale Models

Transport equations for macroscale models are similar in form to their counterparts in mesoscale models (see Sections 2.3.2–2.3.4). Certainly, the individual terms in macroscale models describe very different physics, and in essence the following key differences have to be considered: (i) filtered quantities are considered in the balance equations and (ii) different closures need to be used for stresses and interphase exchange terms. The latter may require the solution of additional transport equations, e.g., to predict mesoscale velocity fluctuations in the gas and particle phase. A beautiful presentation of the resulting set of equations has been recently documented by Schneiderbauer (2017)—the interested reader is referred to this publication as a first read on the subject.

## 2.4 Governing Equations for Scalar Transport in the Continuous Phase

### 2.4.1 Particle-Resolved Approach

After accepting the assumption of a continuous phase that has constant physical properties (i.e., density, viscosity, heat capacity, etc.), the transport equation for a scalar quantity  $\theta$  reads as:

$$\partial_t \theta^\circ + \nabla \cdot (\mathbf{u}^\circ \theta^\circ) = D_f \nabla^2 \theta^\circ + \mathbf{F}_\theta^\Omega. \quad (13)$$

In analogy to the presentation in Section 2.3.1,  $\mathbf{F}_\theta^\Omega$  is a volumetric boundary forcing term that is used in some formulations (Municchi and Radl, 2017), and the superscript circle is used to identify point variables.  $D_f$  is a scalar diffusivity in the continuous phase, e.g., for thermal transport it is the thermal diffusivity  $a_f = \lambda_f / (\rho_f c_p, \beta)$ , where  $\lambda$  and  $c_p$  are heat conductivity and heat capacity, respectively. Eq. (13) can be modified to consider homogeneous chemical reactions in a straightforward manner, given the flow, temperature, and concentration field are well resolved.

Frequently used boundary conditions are the classical fixed value or fixed flux condition at the particle surface, as well as specialized conditions for periodic boxes (Municchi and Radl, 2017; Sun et al., 2015).

Finally, it should be noted that in case appreciable changes of the fluid physical properties occur (e.g., the fluid density is affected by temperature, pressure, or species concentration), both momentum and scalar transport equations have to be extended (Dixon, 2017). While such an extension is

relatively straightforward, it typically introduces a large number of additional dimensionless parameters that need to be considered.

In some applications (e.g., when modelling the droplet concentration in a gas; [Askarishahi et al., 2017](#)), it helps to view the scalar quantity to be tracked as a mass loading (i.e., consider the mass of scalar per unit mass of carrier fluid phase). Then, and when accepting a fixed density of the carrier phase, the scalar transport equation for the mass loading (i.e., a transport equation similar to [Eq. 13](#)) is exact in the sense that it accounts for density variations due to changes in the scalar concentration.

### **2.4.2 Particle-Unresolved Approach**

Adopting the same assumptions as in [Section 2.4.1](#), one arrives at the following transport equation for scalar local mean quantities:

$$\partial_t (\phi_f \theta) + \nabla \cdot (\phi_f \mathbf{u} \theta) = \nabla \cdot [\mathbf{D}_{\text{eff},f} \cdot \nabla (\phi_f \theta)] + \Phi_{\theta,p \rightarrow f}. \quad (14)$$

The most significant change compared to the particle-resolved approach is that an effective diffusivity tensor  $\mathbf{D}_{\text{eff}}$  must be considered instead of a scalar molecular diffusivity. Only in some simple situations this tensor may mutate to a scalar effective diffusivity. Corresponding closure models for the effective diffusivity—to be used in fixed bed applications—are well documented in literature ([Delgado, 2006](#)). In contrast, literature on the effect of particle relative motion on the effective diffusivity is rather scarce ([Derksen, 2008a, b](#)). As expected and shown by [Derksen \(2009\)](#), particle relative motion in fluidized beds accelerates scalar dispersion.

The volumetric scalar interface exchange rate  $\Phi_{\theta,p \rightarrow f}$  is modeled in analogy to the volumetric fluid–particle interaction force. Closure models for  $\Phi_{\theta,p \rightarrow f}$  useful to study heat and mass transfer, are summarized in [Section 2.5](#).

Finally, a filtered version of the above scalar transport equation can be derived ([Agrawal et al., 2013](#)), a procedure which is formally identical to that for the momentum equation (see [Section 2.3.5](#)). The same applies to systems with heterogeneous chemical reactions ([Holloway and Sundaresan, 2012](#)). Similar challenges as for momentum transport arise when seeking for closures to the filtered scalar transport equation: the interphase exchange term needs to be modified, and an additional dispersion term has to be included. These challenges are currently about to be addressed in ongoing research activities ([Cloete et al., 2017b](#), under review).

## 2.5 Closure Laws Required at the Mesolevel

### 2.5.1 Momentum Transfer: Drag and Buoyancy

#### 2.5.1.1 Splitting the Fluid–Particle Interaction Force

Next, the most commonly employed splitting of the total fluid–particle interaction force  $\mathbf{f}_{f \rightarrow p}$  is discussed. Note, this force is simply the negative of the particle–fluid force  $\mathbf{f}_{p \rightarrow f}$  which was already introduced in [Section 2.3.2](#).

In dense gas–particle systems a mean pressure gradient  $\nabla p$ —generally pointing against the main flow direction—arises next to small-scale variations of the fluid–phase stress. The latter originate from the difference between the point variable  $p^\circ$  (i.e., the local pressure, see [Section 2.3.1](#)) and its local mean counterpart  $p$ , as well as the local flow field  $\mathbf{u}^\circ$ . Hence, it is intuitively clear that it will be useful to account for two contributions to the total fluid–particle interaction force  $\mathbf{f}_{f \rightarrow p}$ : (i) one originating from a mean pressure gradient  $\nabla p$  and (ii) one accounting for the remaining variations in the fluid–phase stress.

The mean pressure gradient developing in dense gas–particle suspensions arises naturally when fluid is pushed through the interstices of the particles—this gradient can be readily extracted from PR–DNS. Most important, this pressure gradient is also known in Euler–Euler and PU–EL-based simulations. Hence, one will use this known information on the mean pressure gradient  $\nabla p$  to calculate its contribution to the fluid–particle force in EE or PU–EL simulations (this contribution is typically referred to as buoyancy or generalized buoyancy force). Consequently, a meaningful strategy is splitting off the contribution of the mean pressure gradient in PR–DNS from  $\mathbf{f}_{f \rightarrow p}$  to isolate a remaining force contribution (see [Section 4.2.3](#) for more details regarding this force calculation procedure). Here, the latter force contribution is called the drag force  $\mathbf{f}_{\text{drag},i}$  and needs to be reformulated in a closed form for the governing equations. In the context of PU–EL, i.e., when considering a particle with index  $i$ , the force splitting strategy can be formally expressed as:

$$\mathbf{f}_{f \rightarrow p,i} = -V_i \nabla p + \mathbf{f}_{\text{drag},i} \quad (15)$$

We note in passing that in most dense suspension flows, the drag and mean pressure gradient force dominate fluid–particle interactions—contributions that may be characterized as a lift or added mass force are typically of lower importance. Thus, there is typically no need to perform a further splitting of the remaining force contribution, implying that  $\mathbf{f}_{\text{drag},i}$  lumps all fluid–particle interaction forces that originate from small-scale variations of the fluid–phase stresses into a single term.

### 2.5.1.2 Ensemble-Average vs Per-Particle

Certainly, closure models for the drag force were in the focus of previous developments, with the most prominent examples being the relations proposed by [Wen and Yu \(1966\)](#), Sundaresan and coworkers ([Holloway et al., 2010, 2012](#); [Yin and Sundaresan, 2009](#)), or van der Hoef and coworkers ([Beetstra et al., 2007](#); [van der Hoef et al., 2005](#)). The closure models developed by the latter two groups claim to be suitable for polydisperse suspensions and provide expressions for the *ensemble-average* drag force acting on each particle species (i.e., a class of particles that shares the same size).

A more recent study by [Kriebitzsch et al. \(2013\)](#) considered the fluctuation of the total per-particle fluid–particle force (i.e., the drag force plus the pressure gradient force). These authors found that the average force is only a poor representation of the distribution of forces. Clearly, per-particle and ensemble-average drag coefficient vary appreciably, leading to the need for a closer examination of how to split individual force contributions ([Municchi and Radl, 2017](#)). Also, the “drag like” contributions to the fluid–particle interaction force—explored just recently by [Holloway et al. \(2010\)](#)—focused only on average forces and no closure model for per-particle forces was presented. A similar gap in knowledge can be identified when considering lift forces (both for their average value and the per-particle distribution): while those forces are well understood in dilute suspensions—even for nonspherical particles ([Amini et al., 2014](#); [Di Carlo, 2009](#); [Hölzer and Sommerfeld, 2009](#); [Ouchene et al., 2015, 2016](#); [Stan et al., 2013](#); [Zastawny et al., 2012](#))—this is clearly not the case for dense suspensions (an exception are recent attempts by a French group; [Ouchene et al., 2014](#)).

Next, a classical description of drag forces acting on an ensemble of particles is presented. More recent developments are summarized in [Sections 5.1–5.4](#).

### 2.5.1.3 Drag Force

In the context of suspension mechanics, the drag force acting on particles of species  $i$  is calculated under the assumptions that all neighboring particles move with the same speed. Thus, a “fixed bed” ansatz is followed, which reads:

$$\mathbf{f}_{\text{drag, fixed}, i} = V_{p,i} \beta_{p,i} (\mathbf{u}_i - \mathbf{v}_i). \quad (16)$$

Here  $\beta_{p,i}$  is a particle friction coefficient, which is different from the volume-specific friction coefficient  $\beta_i$  used in the context of EE models.

$V_{p,i}$  is a particle volume. A classical model for the particle friction coefficient in a monodisperse (fixed) bed of particles is (Beetstra et al., 2007):

$$\beta_{p,i} = \frac{18\mu_f}{d_p^2} (1 - \phi_p) [F_0 + G_0], \quad (17)$$

$$F_0 = \frac{10\phi_p}{(1 - \phi_p)^2} + (1 - \phi_p)^2 (1 + 1.5 \sqrt{\phi_p}), \quad (18)$$

$$G_0 = \frac{0.413 Re_p}{24 (1 - \phi_p)^2} \left[ \frac{(1 - \phi_p)^{-1} + 3\phi_p (1 - \phi_p) + 8.4 Re_p^{-0.343}}{1 + 10^{3\phi_p} Re_p^{-(1+4\phi_p)/2}} \right], \quad (19)$$

$$Re_p = \frac{(1 - \phi_p) \rho_f d_p |\mathbf{u}_i - \mathbf{v}_i|}{\mu_f}. \quad (20)$$

Here  $F_0$  and  $G_0$  are dimensionless functions, and  $Re_p$  is a particle Reynolds number. For polydisperse (fixed) particle beds the situation becomes more complicated, and the following has been proposed (Beetstra et al., 2007):

$$\beta_{p,\text{poly},i} = \frac{18\mu_f}{d_p^2} (1 - \phi_p) F_{\text{poly},i}, \quad (21)$$

$$F_{\text{poly},i} = [F_0 + G_0] \left[ (1 - \phi_p) \gamma_i + \phi_p \gamma_i^2 + 0.064 (1 - \phi_p)^3 \right]. \quad (22)$$

Here  $\gamma_i$  is a dimensionless particle size. Note, that in Eqs. (21) and (22) the particle Reynolds number used to compute  $F_0$  and  $G_0$  is defined slightly different than what is shown in Eq. (20). Sundaresan and coworkers (Holloway et al., 2010; Yin and Sundaresan, 2009) proposed another modification to compute drag forces in polydisperse suspensions. They follow the principal idea of Beetstra et al.'s model (Beetstra et al., 2007), but suggest:

$$\beta_{p,\text{YSH,poly},i} = \frac{18\mu_f}{d_p^2} (1 - \phi_p) \left\{ \frac{1}{1 - \phi_p} + \left( [F_0 + G_0] - \frac{1}{1 - \phi_p} \right) (a \gamma_i + [1 - a] \gamma_i^2) \right\}, \quad (23)$$

$$a = 1 - 2.66\phi_p + 9.096\phi_p^2 - 11.338\phi_p^3. \quad (24)$$

Municchi and Radl (2017) find good agreement with Beetstra et al.'s closure model shown in Eq. (21). However, they propose a correction when

applied to EL-based simulations (in order to be consistent with an EL model formulation):

$$F_{\text{poly}, MR, i} = -0.122 + 1.18 F_{\text{poly}, i} + 0.00352 F_{\text{poly}, i}^2. \quad (25)$$

Note, that all above models are valid only for the *ensemble-average* drag force, and strictly speaking not for individual particles (Municchi and Radl, 2017). Thus, when applied to EL-based models, only the average drag force—but not the particle-individual one—can be predicted correctly.

#### 2.5.1.4 Generalized Buoyancy

Buoyancy forces arise due to gradients in the average stress field of the continuous phase. These forces act in addition to the forces originating from small-scale stress fluctuations, i.e., that captured by the drag force closures detailed in the previous paragraph. The generalized buoyancy force closure below accounts for the mean pressure and deviatoric stress field.

$$\mathbf{f}_{\text{buo}, i} = V_{p, i} (-\nabla p_i + \nabla \cdot \boldsymbol{\tau}_f). \quad (26)$$

#### 2.5.2 Scalar Transport

Heat and mass transfer rates are extremely well explored in packed beds consisting of equally sized particles. This is true for both spherical and nonspherical particles (Singhal et al., 2017). Packed beds are examples for densely packed fluid-particle suspensions in which particles are not allowed to move. More scarce are closure models for less dense suspensions, which are often based on the correlation of Gunn (1978). Note, that these correlations are often only valid for Schmidt and Prandtl numbers close to unity. Also, consistency needs to be ensured: The work of Sun et al. (2015) highlights the importance of using the correct fluid temperature. For example, an inconsistency is caused when using the cup-mixing temperature when building a closure (e.g., from data collected in DNS), and a spatially averaged fluid temperature when applying the closure.

Closures for predicting heat and mass transfer rates in polydisperse suspensions are extremely scarce, same as information on the distribution of per-particle heat and mass transfer coefficients. Similarly, for high Reynolds, Schmidt, and Prandtl numbers, as well as high particle concentrations, literature is typically confined to a few studies (Derksen, 2014b). Clearly, a breakthrough in the sense of a rigorously valid correlation for the reliable prediction of heat and mass transfer coefficients is still missing.

### 2.5.2.1 Heat and Mass Transfer

The rate of heat and mass transfer is closed by correlations for the Nusselt ( $Nu$ ) and Sherwood ( $Sh$ ) number, respectively. Specifically, one writes the per-particle transferred amount of heat (and similarly for the mass transfer rate) as:

$$\dot{q}_T = Nu \lambda_f d_p \pi (T_{f,i} - T_{p,i}). \quad (27)$$

The most widely used expression for the Nusselt number in dense fluid–particle suspensions is (Gunn, 1978):

$$Nu = \left( 7 - 10\phi_f + 5\phi_f^2 \right) \left( 1 + 0.7 Re^{1/5} Pr^{1/3} \right) + \left( 1.33 - 2.4\phi_f + 1.2\phi_f^2 \right) Re^{7/10} Pr^{1/3} \quad (28)$$

The appeal of Gunn's relation is that it satisfies four limiting relations (i.e., the low and high Reynolds number limit, the low Reynolds number single-particle limit, and the experimentally established dependencies of  $Nu$  with respect to the Prandtl and Reynolds number for the single-particle and packed-bed limit). Consequently, the shape of the relation shown in Eq. (28) has been widely accepted, and often only coefficients are refitted to new data (Deen et al., 2014; Singhal et al., 2017; Tavassoli et al., 2015).

Two important, but often neglected facts related to the application of Eq. (27) are that:

- (i) the fluid's cup-mixing and local mean temperature are often confused (Municchi and Radl, 2017; Sun et al., 2015). Thus, care must be taken to ensure the correlation to be used is based on the local mean fluid temperature (or concentration) when applying EL models;
- (ii) Available correlations are only able to predict ensemble-average Nusselt and Sherwood numbers. Consequently, one must accept typically large uncertainties when predicting per-particle transfer rates (Municchi and Radl, 2017).

Another detail—though relevant for mass transfer calculations involving wet granular materials only—is that of the available surface area. Often only a fraction of the particle's surface is covered with liquid, and only this wetted area must be considered for calculating mass transfer rates. A thorough description of how to calculate this wetted area fraction has been recently provided (Askarishahi et al., 2017).

All correlations presented above for  $Nu$  (and  $Sh$ ) must be understood as particle- and ensemble-average dimensionless transfer rate coefficients.

Recently, an attempt to improve existing correlations was carried out ([Kravets and Kruggel-Emden, 2017](#)). These authors establish a correlation for the ensemble-average, but angle-resolved heat transfer coefficient in dense suspensions. “Angle-resolved” hereby refers to transfer coefficients that depend on a particle surface coordinate, specifically a parameterization using the angle between the mean flow velocity (i.e.,  $\mathbf{u}$ ) and a position on the particle’s surface expressed in a spherical, particle-centered frame of reference. The useful aspect of the study remains questionable, since per-particle (but angle-averaged) heat transfer coefficients were not presented. However, the recent efforts documented in literature ([Kravets and Kruggel-Emden, 2017](#); [Municchi and Radl, 2017](#)) stress the importance of future research to refine heat and mass transfer closure models to a state at which they are truly applicable to PU-EL-based models. Such efforts are discussed in greater detail in [Sections 5.4.2 and 5.5.3](#).

### 2.5.2.2 Dispersion Coefficients

When considering heat and mass transfer, an additional closure naturally enters the system of equations to be used in a mesoscale model: the dispersion coefficient that characterizes how quickly an inert scalar is distributed randomly in the fluid domain. [Delgado \(2006\)](#) provides an excellent review of closures for packed beds. Dispersion rates of dissolved scalars in the fluid phase of an agitated suspension have been simulated only recently ([Derksen, 2008b](#)). A more recent study considered freely sedimenting suspensions, and additionally analyzed particle self-diffusivities in these systems ([Derksen, 2014a](#)). Both studies were performed for large Schmidt numbers and revealed the key scaling of dispersion coefficients in (sedimenting) suspensions, as well as their anisotropic nature. In summary, the development of closures for dispersion coefficients offers a similarly wide playground compared to that offered by heat and mass transfer rates. Clearly, extensions to (i) polydisperse systems, as well as (ii) systems made of nonspherical particles would be appreciated to provide more general closure models for dispersion coefficients.

## 2.6 Closure Laws Required at the Macrolevel

### 2.6.1 Phenomena That Affect Transport on the Macrolevel

The spontaneous clustering of freely sedimenting suspensions is characterized by strong fluctuations of the particle concentration and velocity. Fox and coworkers ([Capecelatro et al., 2014, 2015](#)) refer to this clustering and its consequences as “cluster-induced turbulence” (CIT). CIT is caused by the inherent instability of the fluidized state of a fluid–particle suspension

(Fullmer and Hrenya, 2017; Sundaresan, 2003). It appears that Jackson made the first attempt to probe the physical origin of CIT as early as 1963 (Jackson, 2000), and Glasser et al. (1998) were the first that simulated the instability that causes CIT with a computer. CIT does also occur in low Reynolds number suspensions (i.e., in systems where the particle-based Reynolds number is  $O(1)$  or less). Most important, spontaneous clustering and CIT are fundamentally different from clustering of inertial particles that is induced by turbulent motion (Calzavarini et al., 2008). This is why one should not connect CIT with classical turbulence theory, but rather with spontaneous clustering phenomena.

CIT has been predicted with Euler–Euler (i.e., continuum-based) models, Euler–Lagrange models (Capecelatro et al., 2015; Radl and Sundaresan, 2014; Radl et al., 2012) (see Fig. 5 for an illustration), as well as PR-DNS (Derksen and Sundaresan, 2007; Uhlmann and Doychev, 2014). For dilute (i.e., 0.5 volume percent) liquid–particle systems, the density ratio and the Galileo number characterize the tendency for clustering (Uhlmann and Doychev, 2014).

### 2.6.2 Momentum Transfer

The primary effect of CIT is that it significantly alters momentum transfer rates between the fluid and the particles. In dilute suspensions only a weak

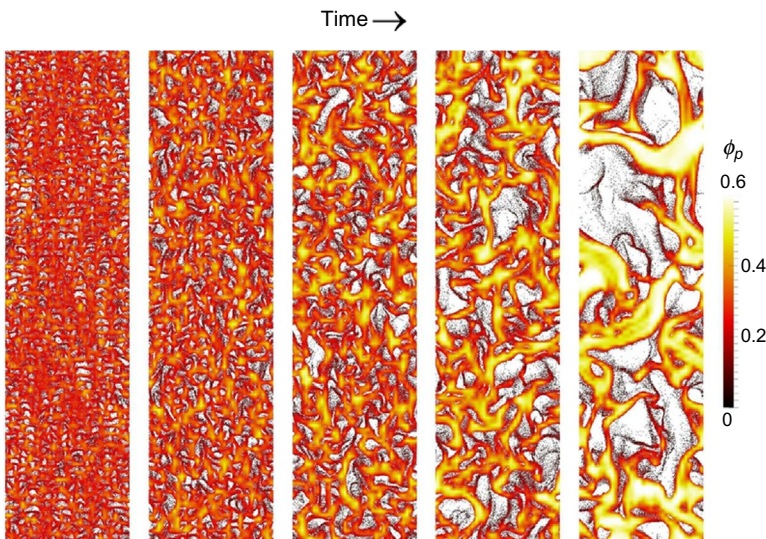


**Fig. 5** Temporal evolution of the local particle volume fraction  $\phi_p$  in a freely sedimenting gas–particle suspension (pseudo two-dimensional simulation using an Euler–Lagrange approach).

increase (i.e., approximately 12%) of the mean fluid–particle slip velocity is observed (Uhlmann and Doychev, 2014). Clustering causes a much more drastic increase (i.e., several hundred percent!) of the slip velocity for intermediate dense to dense suspensions. The latter can be characterized by a decrease of the average drag coefficient of up to 95% (Radl and Sundaresan, 2014). Clearly, there is a strong need to account for this decrease of the average momentum exchange coefficient, which is accommodated by correcting the drag coefficient. The principal shape of such drag modifications is:

$$\bar{\beta}_p = \beta_p \left[ 1 - H\left(\bar{\phi}_p, \Delta, \bar{\xi}\right) \right]. \quad (29)$$

Here  $H$  is a (typically scalar-valued) correction function, and  $\bar{\xi}$  is a placeholder for additional markers that are available on the level of filtered quantities and affect the correction  $H$ . A large collection of potential markers has been tested in literature—mainly by applying filtering tools to cluster-resolved simulation data—with no ultimate consensus so far (Cloete et al., 2017a,b; Igci and Sundaresan, 2011; Milioli et al., 2013; Ozel et al., 2013; Schneiderbauer, 2017).

Correction functions  $H$  for the drag have been carefully analyzed for monodisperse gas–particle suspensions over the past 10 years. Concerning polydisperse systems, some pioneering work has been done by the group of Sundaresan on bidisperse systems (Holloway and Sundaresan, 2014). This group attempted to shed light on the effect of clustering on effective momentum exchange coefficients in sedimenting suspensions, as well as the effective stress. This work also established the framework for a filtered multifluid model (in the context of EE models), that might help to explain segregation phenomena in large-scale devices. Follow-up work following this thought has been already published (Zhou and Wang, 2015). In summary, what has been done for polydisperse suspensions is still far from being sufficient.

### 2.6.3 Stress in the Particulate Phase

Closures that account for the effect of mesoscale phenomena on the particle- and gas-phase stresses are required on the macrolevel (Agrawal et al., 2001; Igci et al., 2008; Sarkar et al., 2016; Schneiderbauer, 2017). In addition to these “mesostresses,” the filtered kinetic theory-based stresses, as well as the filtered frictional stresses, potentially, must be considered.

Several assumptions are generally adopted to limit the number of closures in modelling mesoscale stresses:

- (i) fluid-phase mesoscale stresses are assumed to be small. This is valid as long as the fluid's density is much smaller than that of the particles
- (ii) contributions from the filtered kinetic theory-based stresses—relative to the mesoscale solids stresses—decrease with increasing filter size. Thus, for models on the macrolevel that aim on industrial scale applications, filtered kinetic theory-based stresses can be neglected
- (iii) filtered frictional stresses are relevant only for densely packed regions and have been given a lower amount of attention with only a few exceptions ([Schneiderbauer and Pirker, 2014](#)).

Mesoscale stresses developing in the particulate phase are expected to be the second most important piece of missing information that needs closure in models on the macrolevel. Indeed, a recent study [Schneiderbauer \(2017\)](#) reported that forces due to mesoscale (particle) stresses may even exceed that caused by drag. This clearly indicates that forces due to mesoscale stresses, although smaller than the filtered drag forces on average, are significant. A typical Boussinesq-like ansatz for closing the particle-phase mesoscale stresses in a macroscale model is ([Schneiderbauer, 2017](#)):

$$\boldsymbol{\tau}_{p,\text{meso}} = \mathbf{I} \frac{2}{3} \bar{\phi}_p \rho_p k_p - 2 \bar{\phi}_p \mu_{p,\text{meso}} \bar{\mathbf{S}}_p. \quad (30)$$

The reader should be reminded that an overbar indicates filtered quantities (which are explicitly calculated in the macromodel). Also,  $\mathbf{I}$  is the identity matrix, and  $\mathbf{S}$  is the deviatoric part of the rate of deformation tensor.  $k_p$  (i.e., the kinetic energy of mesoscale velocity fluctuations) and  $\mu_{p,\text{meso}}$  (i.e., the mesoscale viscosity) require closure, for which a variety of options exist. An especially appealing option is considering a balance equation for  $k_p$ . Thus, one first aims at predicting mesoscale velocity fluctuations to close the pressure-like term in the expression for the mesoscale stress. Subsequently, the viscosity can be closed using a simple mixing length assumption. Also, knowing  $k_p$  (and  $k_g$ , i.e., the gas phase mesoscale kinetic energy) greatly helps to close the coefficient for interphase momentum transfer in macroscale models ([Schneiderbauer, 2017](#)).

This approach to close the stress—while certainly at the bleeding edge of development—has the shortcoming that it is inherently assumed that the mesoscale stress state can be characterized with two scalar quantities: a pressure-like term and a viscosity term. This implies isotropy in the subgrid scale velocity fluctuations (and hence implies the absence of normal stress differences), which may not be justified. In [Sections 6.2 and 6.4](#) some recent efforts are documented that make an attempt to overcome this shortcoming.

### 2.6.4 Heat and Mass Transfer

Similar to what is done for the drag, exchange coefficients for heat and mass, as well as heterogeneous reaction rates need to be corrected in case CIT occurs (Agrawal et al., 2013; Cloete et al., 2011; Holloway and Sundaresan, 2011, 2012; Schneiderbauer, 2017; Sundaresan et al., 2013). Modifications to the heat and mass exchange coefficients (denoted here as  $\gamma$ ) are typically closed following the ansatz (Agrawal et al., 2013):

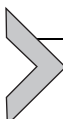
$$\bar{\gamma} = \gamma \left( 1 - Q\left(\bar{\phi}_p, \Delta\right) \right). \quad (31)$$

Here  $Q$  is a correction function that is typically taken to depend on the filtered particle volume fraction and the filter size. However, expansion to other sets of markers can be done similar to what has been discussed in Section 2.6.2.

In analogy to mesoscale stresses in the momentum equations, a dispersive flux due to unresolved velocity and temperature (or species concentration) fluctuations must be considered. This dispersion flux is modeled similar to a diffusion term, with a dispersion coefficient  $D$  approximated by a Smagorinsky-like ansatz (Agrawal et al., 2013; Cloete et al., 2017b). For example, for the particulate phase one can model this mesoscale dispersion with:

$$D_{p,\text{meso}} = C_{p,\text{meso}} \left( \bar{\phi}_p \right) \Delta^2 \|\bar{\mathbf{s}}_p\|. \quad (32)$$

Here  $C_{p,\text{meso}}$  is a Smagorinsky-like parameter that is modeled as a function of the filtered particle volume fraction (Agrawal et al., 2013).



## 3. ALGORITHMIC ASPECTS

### 3.1 Flow Simulators

Simulations of granular and suspension flows started in the late 1970s, a time where physical chemists had already invented the widely used molecular dynamics simulation approach. Specifically, the soft-sphere simulation method (Cundall and Strack, 1979) was published in 1979. Some earlier publications of Cundall in this matter even date back to 1971. This method is now widely referred to as the “discrete element method”, or simply DEM. Nearly at the same time, the second ingredient for modern computational granular rheology, i.e., the Lees–Edwards boundary conditions were published (Lees and Edwards, 1972). Approximately 10 years later, Stokesian dynamics (SD) for studying suspension flows at low Reynolds numbers was developed (Brady and Bossis, 1988; Sierou and Brady, 2001). SD was a key tool for

generating new insight with limited computational resources since it does not require a discretization of the fluid domain. This study nicely illustrates the desperate need for more computational resources that was clearly limiting scientific progress at that time.

What followed was a fast development of tools in the 1990s: one example is the Lattice Boltzmann method (LBM), which was first applied by [Ladd \(1994\)](#) to model suspension flows. Starting around the year 2000, LBM was increasingly used in the community as the data generation workhorse, as an example see the work of [Rohde et al. \(2002\)](#) or [DerkSEN \(2008b\)](#). In addition, conventional finite volume techniques (e.g., IBM, see [Fig. 6](#) for an example) are now extensively used and progressively refined ([Municchi and Radl, 2017](#); [Podlozhnyuk et al., 2016](#); [Sun et al., 2015](#); [Uhlmann and Doychev, 2014](#)).

The above simulators are used to solve microscale models—all details of the flow system on the scale of individual particles are resolved. A plethora of commercial and open-source simulators exists that implement various computational strategies (see [Section 1.3](#)) to evaluate “engineering” models (i.e., EE-based or PU-EL-based models). A more comprehensive summary of such strategies is provided in various review articles (e.g., Section “Mechanistic Process Modelling” of [Rantanen and Khinast \(2015\)](#), as well as [Fullmer and Hrenya \(2017\)](#)).

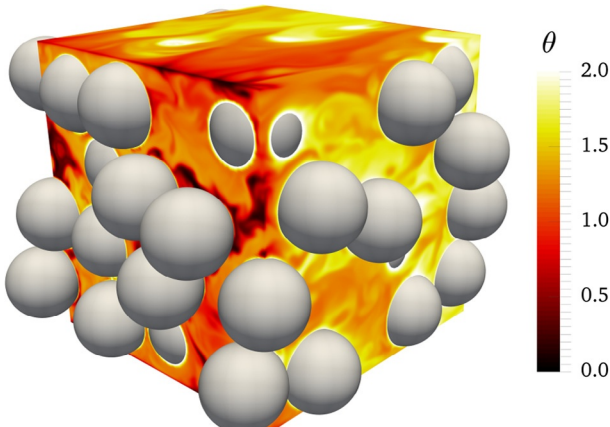


**Fig. 6** Temperature field  $\theta$  in the fluid phase of a gas–particle suspension bound by two infinite parallel adiabatic walls (the Reynolds number is 400, the Prandtl number is 1, and the particle volume fraction is 0.4).

## 3.2 Filtering Tools

### 3.2.1 Requirements and Challenges Associated With Spatial Filtering

At the most fundamental level, PR-DNSs are used to derive coefficients for heat, momentum, and mass transfer in dense particulate systems (Deen et al., 2012, 2014; Feng and Musong, 2014; Tavassoli et al., 2013; Zaidi et al., 2014). Typically, a certain number of realizations for the case studied is needed in order to derive statistically meaningful correlations (Tenneti and Subramaniam, 2014 ; Tenneti et al., 2013). This approach requires to process data from large data sets in order to compute averaged (mean) quantities (which are needed to evaluate transfer coefficient), standard deviations, or other statistics like the distribution of the angle between two vector fields (Kriebitzsch et al., 2013). Also, strategies that rely on the temporal evolution of flow quantities (e.g., the transients of one-dimensional concentration profiles) are in use to evaluate transport coefficients in fluid–particle systems. An example of such a strategy is the work of Derksen, who quantified scalar dispersion rates in sedimenting liquid–particle suspensions (Derksen, 2014b).

The same approach, i.e., considering statistical data of, e.g., the velocity fluctuations, can be used on intermediate length scales when deriving meso- and macroscale models for engineering applications. Typically, this results in an Eulerian grid coarsening approach, e.g., by deriving models for the subgrid-scale fluid–particle agitation (Igci et al., 2008). Favre averaging of relevant fluid variables (e.g., the fluid velocity), and fluid–particle interactions (e.g., the coupling force) is generally adopted to derive these closures. A Favre average refers to the phase mass-based average as detailed in Appendix A.1, and is in its standard form defined as  $\overline{(*)} = \overline{\phi(*)}/\overline{\phi}$  where  $\phi$  is the phase fraction.

In case an Euler–Lagrange approach is followed, the effect of particle coarsening (i.e., each simulated particle is a proxy for a prescribed number of particles named parcel) has to be taken into account as well (Ozel et al., 2016). All these examples document current challenges that need to be met by a universal filtering tool.

In principle, the application of an appropriate filtering strategy is straightforward once the fluid–particle flow simulator is available. However, filtering of scientific data and coarse-graining poses several challenges from the software point of view. For example, spatio-temporal averages have to be computed across different processors for the (typically large) filter sizes. Typically, filter sizes to be used when filtering PR-DNS data have a size of two to five particle diameters. Thus, filtering is typically performed over  $20^3$  to  $50^3$  Eulerian grid cells, often located on different processors. This requires an

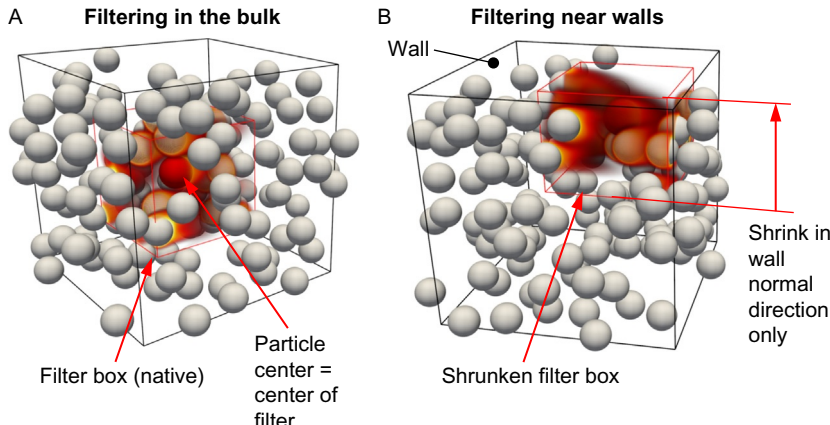


**Fig. 7** Illustration of the shape and size of the filtering region in the bulk (A), as well as in the proximity of walls (B).

algorithm that can deal with parallel communication, and does not require mirroring the full field information on every processor. The latter is of course a feasible approach, however, when aiming on large-scale simulations this would require an excessive use of RAM. At the same time, parallel communication of local field values requires significant network resources due to the large amount of data to communicate. Another issue is the amount of data generated during the simulation run: the implemented algorithms should be able to work on the fly in order to process (i.e., time-average) data from different time steps. Also, there should be a clear separation (in terms of namespaces and classes) between the simulator and the postprocessing utility such that the latter can be linked to different simulators.

Finally, the library should be modular in order to make the addition of new features as easy as possible. For example, filtering near walls might require changing the filter box shape and size (see Fig. 7 for an illustration).

### 3.2.2 The Tool CPPPO

The library CPPPO addresses the above challenges. While most of the existing filtering algorithms documented in literature were developed for image processing applications (Nakariyakul, 2013; Tsai and Yeh, 2012), CPPPO is able to handle three-dimensional data sets in parallel. Specifically, CPPPO can process data sets from complex geometries and unstructured meshes. CPPPO features a flexible code architecture tailored for scientific computations on high-performance clusters. The library is designed to perform three kinds of operations on the data set:

- 1) Filtering: field volume averaging that can be performed on every cell (for the Eulerian filter option) or at specific user-defined locations (for the Lagrangian filter option). The user can customize the kernel function by adding an arbitrary amount of weights (which have to be scalar fields), or by modifying its form in general.
- 2) Sampling: This operation allows to take samples from the domain (results from the filtering operations may be sampled as well) and relate each sampled value with one or more markers. For example, CPPPO can sample a spatially filtered fluid velocity field at every cell using the fluid-phase fraction as marker. Typical sampling operations include: (i) General sampling: This routine draws samples over the whole domain, or just a portion of it. Sampled fields and markers are defined by the user. Also, general sampling allows the use of a formula parser implemented in CPPPO to draw samples of quantities which are not explicitly calculated in the simulator. These formulas include instructions to compute the gradient, the divergence, dot and double-dot products, as well as simple algebraic manipulations. (ii) Angle vector–vector: This routine can sample vector fields using the angle between the original and a second vector field as marker. (iii) Two point correlation: This routine will sample the value of the trace of a two point correlation.
- 3) Binning: Data collected from sampling operations can be collapsed using binning operations. The marker field values are discretized according to the user input, and a conditional averaging calculation is performed on the sampled field. This data collapsing allows reducing the amount of data that needs to be written to disk. Binning is useful in case the user is only interested in correlations between the means of the sampled quantities and one (or more) markers.

For every user-specified filter (i.e., kernel function), the library performs these three operations in sequence (see Fig. 8). This loop is referred to as the “FSB loop” (Filtering, Sampling, and Binning).

CPPPO can be run in parallel with any simulator that splits the computational domain in several box-shaped subdomains. Since CPPPO is designed for spatial filtering, data should be decomposed according to their position in space. This is true in almost the totality of currently available simulators for CFD either using a finite volume approach (e.g., OpenFOAM®, ANSYS FLUENT®, *Code\_Saturne*®, STAR-CCM+®, AVL FIRE®, etc.) or not (e.g., Palabos®, Nektar++®, Nek5000®, etc.). Parallel communication in CPPPO mainly relies on collective MPI operations, since most of the time all processors have to synchronize during the calculations.

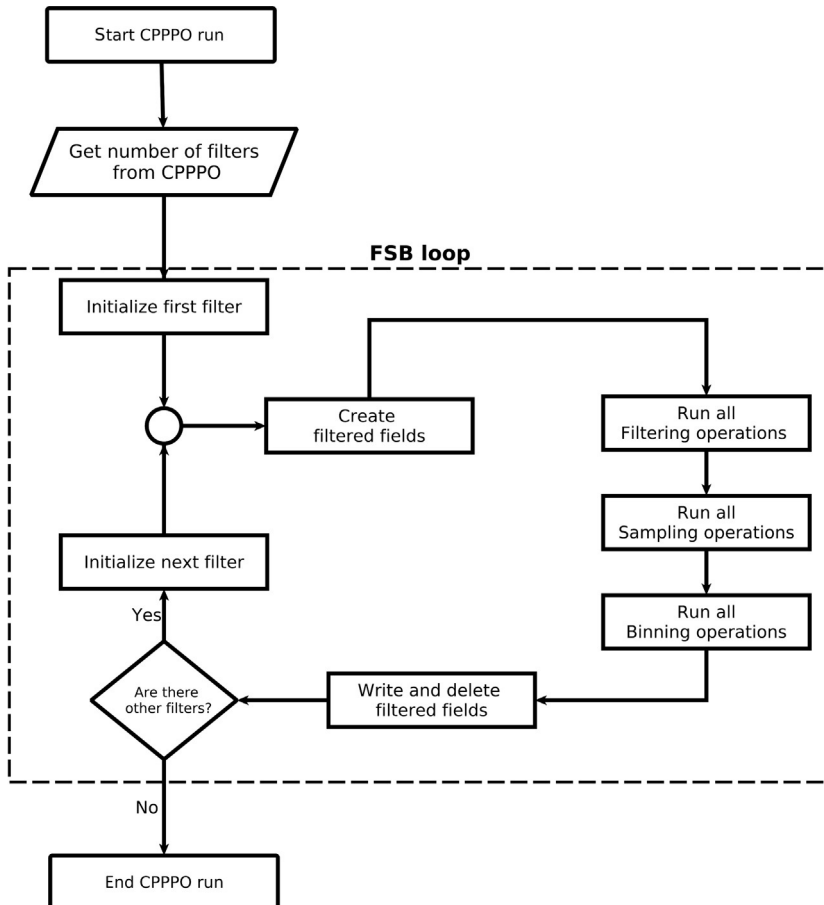


**Fig. 8** The Filtering–Sampling–Binning loop implemented in the filtering tool “CPPPO.” Reproduced from Municchi F, Goniva C, Radl S: Highly efficient spatial data filtering in parallel using the opensource library CPPPO, Comput Phys Commun 207:400–414, 2016.

These MPI routines have shown excellent performance in many applications (Ma et al., 2013; Mamidala et al., 2008) on HPC hardware. The load partitioning in parallel computations with CPPPO is mainly a function of the domain decomposition and the distribution of sampling locations. Hence, it is mostly user dependent. This is particularly true when using Lagrangian filtering operations (i.e., filtering is performed at predefined sampling positions). The reason is that the user affects directly the processor load in such a situation. For example, in case all sampling positions are positioned in a subdomain belonging to the same processor, the calculation would be slow. Thus, all operations would be focused on just one processor.

More details related to the coupling of CPPPO to flow simulators, as well as the implementation of cell selection and parallel filtering routines are provided in a recent publication ([Municchi et al., 2016](#)).

### **3.2.3 Strategies for Computing Averages in Parallel**

Since the calculation of filtered quantities implies long range data exchange operations, processor communication has to be taken into account when designing an algorithm to numerically evaluate the corresponding integrals. On a discrete level these integrals transform to a summation, which can be written as:

$$\overline{\phi}_i = \sum_{j=0}^{j=N_f} V_i \phi_i / V_f. \quad (33)$$

Where the sum is over all  $N_f$  cells inside the filter region,  $V_i$  is the volume of the  $i$ -th cell, and  $V_f$  is the total filter volume. The extension of the above equation to Favre averaging or arbitrary weighted averaging is obvious. The above calculation has to be performed for every cell  $i$  in order to compute a complete field of the filtered quantity. Also, it is necessary to evaluate which cells are inside the filter (i.e., a cell selection is necessary) before the calculation can be started.

The approach described by Eq. (33) is called the *convergent approach* for filtering. This is because, after the list of cells inside the filter is assembled, data from the neighboring cells are passed to the location where the filter is centered. This approach requires (for every location to filter)  $N_f - 1$  summation and multiplication operations, and one division operation. The amount of multiplication operations could be reduced in case the multiplied field values are stored and then communicated. However, this would require additional memory. Also, communication of the cell list and values with other processors has to be performed. As shown in [Fig. 9](#) (left panel), the convergent approach requires the communication of every required cell data owned by another processor. In our case, three values need to be transferred from processor 2 to processor 1. The convergent approach is the most basic approach for spatial filtering, and most of the available filtering algorithms used for image processing are based on it.

In order to reduce the computational load and enhance parallel efficiency, a novel approach named the *divergent approach* was developed. The divergent algorithm does not evaluate the filtered value at any position

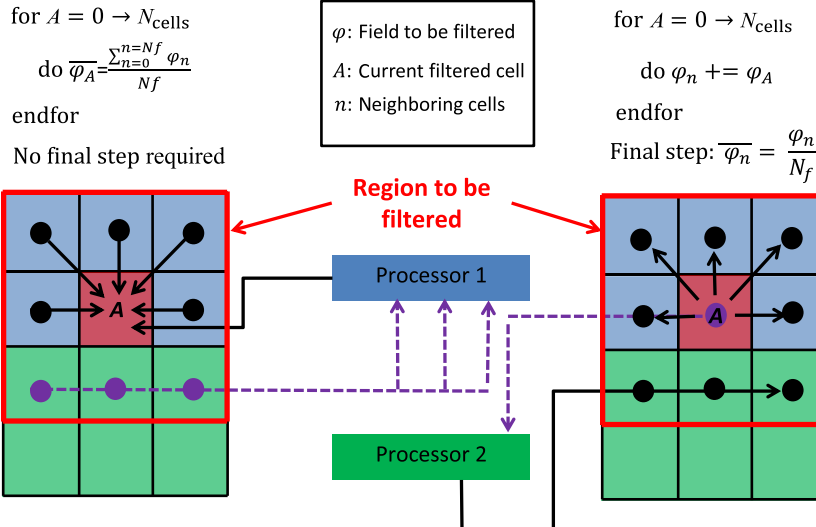


**Fig. 9** Convergent approach (left) and divergent approach (right) for spatial filtering. Continuous arrows represent intraprocessor operations, while dashed arrows indicate data exchange between processors. Processor domains are identified with the owner color, red cells represent the current cell to be filtered. Dots represent cell centres involved in local data operations (black) and parallel data operations (purple).  $N_{\text{cells}}$  is the total number of cells per processor, and  $N_f$  is the number of cells within the region to be filtered.

sequentially, but updates the filtered fields at every step, and ends with a final division step. Specifically, every step consists of:

- i. selecting a cell from the computational domain.
- ii. creating a list of cells located in the region to be filtered around the selected cell.
- iii. multiplying the field value at the selected cell with the required weight (i.e., cell volume or mass density). *Note:* when the filter size tends to the domain size only one cell value needs to be stored and communicated instead of having to allocate and communicate the whole field.
- iv. communicating and adding the multiplied field values to all cells inside the cell list.

The loop has to be repeated for every cell inside the domain. At the end, one last step is needed to divide the values of filtered fields by the filter volume (or by the summed weights in case of Favre averaging). This approach requires (for every cell)  $N_f - 1$  additions, but only one multiplication. The number of divisions in the final step equals the total number of cells. Overall, less multiplication operations are required in the divergent approach compared to a

convergent approach (without allocating memory for the multiplied fields as explained earlier). Most important, the key advantage of the divergent algorithm over the convergent algorithm is the amount of data that needs to be communicated. As shown in Fig. 9 (right panel), in the divergent algorithm the direction of communication is reversed, and just the field value at the current cell needs to be communicated once. The communicated value is then processed locally on the relevant processor (in our case processor 2), which does not involve any communication overhead.

It should be clear that the computational bottleneck for these kind of algorithms is not the number of standard operations, but the number of MPI operations. While image filtering algorithms tend toward a reduction on the number of standard operations, the algorithms implemented in CPPPO have the reduction of the number of MPI operations as the main goal. Since field and mesh data can be very large in terms of the consumed memory, it is often not feasible to rely on massive data copying and thus, processor communications are rather frequent.



## 4. VERIFICATION STRATEGIES

In what follows test cases for the verification of computational tools are summarized. Validation against experimental data is a topic of its own and has been followed quite successfully for a large array of models and closures. The work of [Buist et al. \(2017\)](#) is a representative example of a validation study; more details related to experimental validation strategies are suppressed for brevity in what follows.

### 4.1 Verification Strategy for Filtering Tools

The accuracy of a filtering tool can be tested by considering well-known problems of fluid dynamics: Stokes flow and irrotational (i.e., potential) flow around a sphere. The main objective of these tests is to evaluate the accuracy of the parallel filter routines and to illustrate the dependency of the results on the grid size. Therefore, CPPPO results were compared against analytical solutions of filtered quantities at the particle center ([Municchi et al., 2016](#)). Recalling the analytical solution for Stokes flow (i.e., zero Reynolds number) around a sphere with radius  $R$ , and when considering the velocity component  $u_x$  in the stream-wise (i.e.,  $x$ -) direction, the flow field is described by:

$$u_{x,\text{Stokes}} = U_\infty \left[ \cos^2 \theta \left( 1 + \frac{R^3}{r^3} - \frac{3R}{2r} \right) + \sin^2 \theta \left( 1 - \frac{R^3}{4r^3} - \frac{3R}{4r} \right) \right]. \quad (34)$$

Here,  $\theta$  and  $r$  describe the polar and radial position in a spherical coordinate system, respectively (the solution is symmetric with respect to the azimuthal coordinate).  $U_\infty$  is the flow velocity far from the particle. The corresponding solution for irrotational flow (i.e., a flow characterized by an infinitely large Reynolds number) past a sphere is:

$$u_{x,\text{Irr}} = U_\infty \left[ \cos^2 \theta \left( 1 - \frac{R^3}{r^3} \right) + \sin^2 \theta \left( 1 + \frac{R^3}{2r^3} \right) \right]. \quad (35)$$

Consider now a spherical filter and define a dimensionless filter size as  $\rho = R_f/R$ , where  $R_f$  is the filter radius. Integration of the above equations to obtain the mean (i.e., denoted as  $\bar{u}$ ), and the variance (corresponding to the subgrid stress tensor  $\tau^{\text{sgs}}$ ) of the stream-wise velocity component leads to:

$$\bar{u}_{x,\text{Stokes}} = \frac{2\rho^2 - \rho - 1}{2(\rho^2 + \rho + 1)} U_\infty, \quad (36)$$

$$\tau_{xx,\text{Stokes}}^{\text{sgs}} = \frac{18\rho^5 - 32\rho^4 + 14\rho^3 - 3\rho^2 + 2\rho + 1}{5\rho^3(4\rho^4 + 8\rho^3 + 12\rho^{12} + 8\rho + 4)} U_\infty^2, \quad (37)$$

$$\bar{u}_{x,\text{Irr}} = U_\infty, \quad (38)$$

$$\tau_{xx,\text{Irr}}^{\text{sgs}} = \frac{U_\infty^2}{5\rho^3}. \quad (39)$$

These relations provide a set of cases to verify filtering routines for the situation of a top-Hat filter kernel in spherical coordinates. Corresponding results produced with the tool CPPPO are summarized in Fig. 10 (Municchi et al., 2016).

## 4.2 Selected Verification Cases for Benchmarking Particle-Resolved DNS

Simple verification cases for PR-DNS include drag force and heat transfer from a single sphere. Analytical solutions exist for these cases. However, more relevant for suspension flow simulators are multiparticle configurations that probe all relevant details of the algorithm (e.g., handling of Eulerian cells that are intersected by multiple particle surface). Such cases are summarized next.

### 4.2.1 Creeping Flow Past a Periodic Regular Array of Spheres

To simulate flow past a periodic array of spheres, it is sufficient to simulate the flow past a single sphere in a fully periodic box. This test case allows evaluating the accuracy of the method when two or more particles are close or in contact.

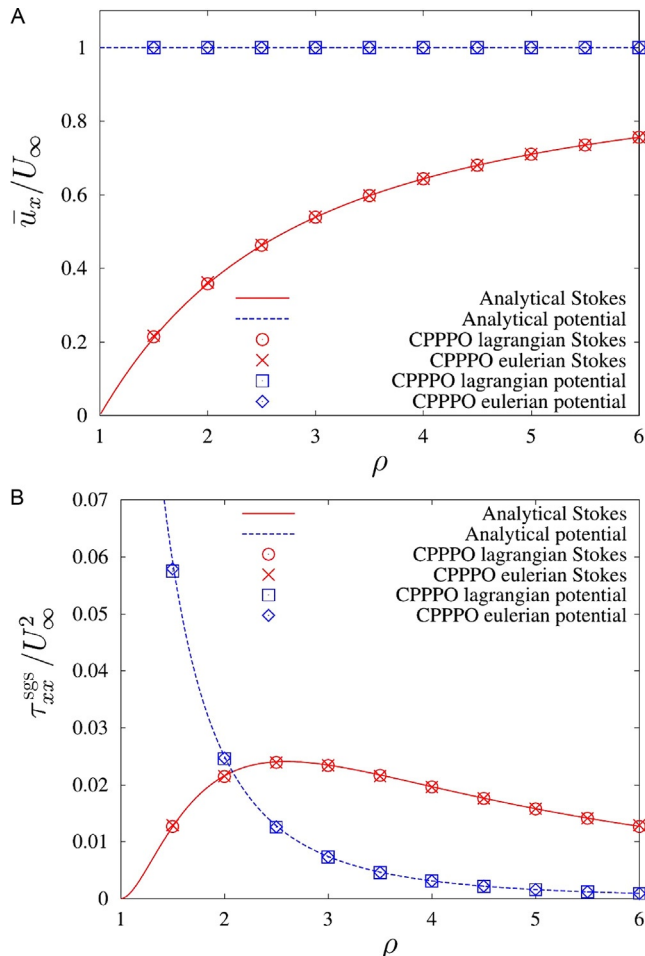


**Fig. 10** Comparison between CPPPO's Lagrangian and Eulerian filtering tools with analytical results for the filtered quantities at the particle centre. Results for the Favre average of the velocity are shown in (A), while in (B) the Favre variance of the velocity was calculated.

Thus, one can assess the effect of a boundary layer reconstruction algorithm that adjusts its order according to the local situation (Municchi and Radl, 2017). For this case, the equations summarized in Section 2.3.1 were solved using a body force to drive a flow field such that the particle Reynolds number is  $2 \times 10^{-5}$  (Municchi and Radl, 2017). The particle diameter was varied for a fixed domain size to adjust the particle volume fraction. Predictions for the dimensionless force (i.e., the force measured from the simulation divided

**Table 2** Relative Deviation of the Magnitude of the Dimensionless Drag Force  $F$  to the Analytical Results of [Zick and Homsy \(1982\)](#)

$\phi_p$	$d_p/\Delta x$	$F_{\text{Zick-Homsy}}$	$\Delta F_{\text{Deen et al.}} (\%)$	$\Delta F_{\text{Municchi-Radl}} [\%]$
0.5236	32	42.14	1.3	1.1
0.450	30.4	28.1	-2.8	1.4
0.343	27.8	15.4	-1.2	2.7
0.216	23.8	7.44	-0.1	-0.8
0.125	19.9	4.292	-0.7	0.3
0.064	15.9	2.81	-1.3	-1.6
0.027	11.9	2.008	-1.9	-2.8

$\Delta x$  is the mesh size. The settings are the same as that employed by [Deen et al. \(2012\)](#).

by the corresponding value for Stokes drag) can then be benchmarked with data from literature (see [Table 2](#)).

#### 4.2.2 Three Particles Aligned With the Main Flow

The case of forced convection past a chain of three spheres is a classical verification case that allows benchmarking predictions for the per-particle Nusselt number and drag coefficient. Recent reference data for this case can be found in literature ([Maheshwari et al., 2006](#); [Tavassoli et al., 2013](#)) for different values of the spacing between the three particles. The flow field predicted by our newly implemented PR-DNS solver ([Municchi and Radl, 2017](#)) is show in [Fig. 11](#). This data, as well as our results for Nusselt number and drag closely match the above literature references.

#### 4.2.3 Densely Packed Random Arrays of Particles

Ensemble-average fluid–particle transfer coefficients (e.g., for momentum and heat) have been widely studied by means of computer simulations for random arrays of particles due to their high industrial significance. Note, that these arrays were typically considered to be periodic and their microstructure to be perfectly isotropic. The setup procedure of such systems is detailed by [van der Hoef et al. \(2005\)](#). The large body of results being now available has been casted in an impressive amount of correlations documenting (i) drag coefficients, as well as (ii) Nusselt (or Sherwood) numbers ([Deen et al., 2014](#); [Municchi and Radl, 2017, 2018](#)).

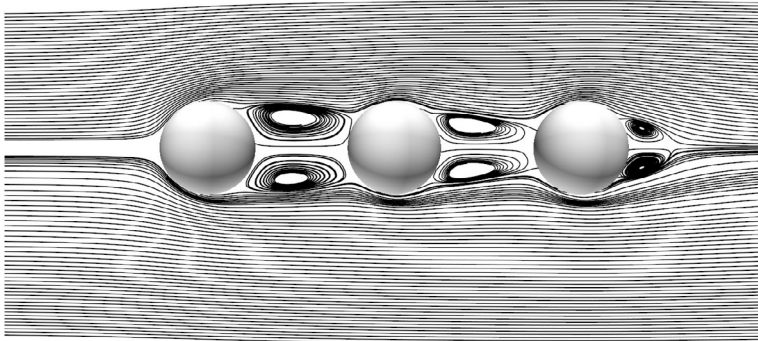


**Fig. 11** Streamlines illustrating the flow field around a chain of particles that is aligned with the main flow direction.

#### 4.2.3.1 A Note on the Drag Force Calculation

With respect to drag, and as outlined in [Section 2.5.1](#), it is important to define the drag force in a meaningful way such that it is correctly separated from the total fluid–particle interaction force. Hence, the question arises how to account for the pressure contribution when computing drag forces from PR-DNS. The standard approach—widely adopted in literature ([Beetstra et al., 2007](#); [van der Hoef et al., 2005](#))—is to rescale the particle-average fluid–particle interaction force with the mean voidage. Alternatively, one can take a more fundamental route and subtract the per-particle buoyancy force (calculated from the mean pressure gradient experienced by an individual particle) from the fluid–particle interaction force. While both approaches yield identical drag forces in the case of a monodisperse bed of particles, differences do exist in case polydisperse beds are considered. The reasons behind this discrepancy have been highlighted just recently ([Municchi and Radl, 2017](#)). They are most obvious in case one considers a single large particle in an infinitely large bed of smaller particles: clearly, in this case the pressure gradient will be set by the small particles. Consequently, the buoyancy force experienced by the larger particle is solely defined by the fluid–particle interaction force of the smaller particles—the fluid–particle interaction force acting on the large particle is of no relevance to the pressure gradient. Thus, subtracting the pressure gradient force for the large particles must account in some way for the size of the smaller particles, which is not the case when using the standard approach. Hence, it is of outmost importance to clarify the exact definition of the drag force during verification studies.

#### 4.2.3.2 Results for Drag

Adopting the widely used standard approach, almost the totality of previous work found excellent agreement of the average drag force with the correlation provided in Section 2.5.1 (Beetstra et al., 2007). This is true for both mono- and bidisperse particle suspensions, and our more recent result (Municchi and Radl, 2017) also agree with this data. Most important, our results indicate that this agreement even holds in case the drag coefficient is evaluated for different filter sizes  $\rho$  (see Fig. 12).

#### 4.2.3.3 Results for Heat Transfer

With respect to heat transfer correlations, a significant amount of reference data has accumulated in literature. In order to make a fair comparison, one should take care when comparing reported Nusselt numbers, since their exact definition matters. The key issue is the definition of the average fluid temperature, for which a (i) spatially filtered or a (ii) flux-averaged value can be used. The difference between these two choices has been carefully evaluated just recently (Sun et al., 2015). When accounting for this difference, our recent work shows that a refitted-version of the popular Gunn correlation (Deen et al., 2014) approximates our data for particle-average heat transfer coefficients well (see Fig. 13; for the largest filter size  $\rho$  the number of samples

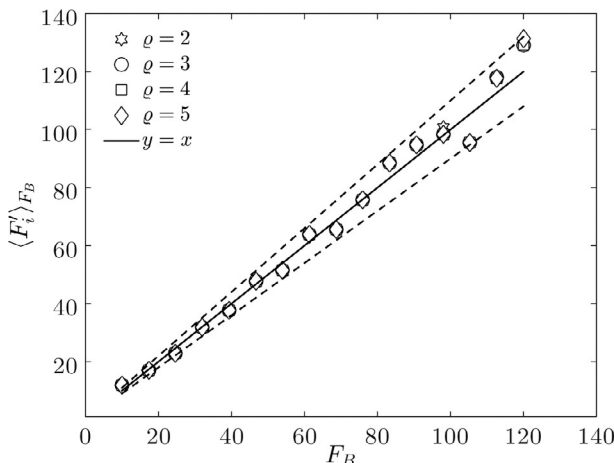


**Fig. 12** Parity plot comparing the normalized average drag force  $\langle F'_i \rangle$  from a recent study (Municchi and Radl, 2017) with the values  $F_B$  predicted by the reference correlation (Beetstra et al., 2007). The dashed lines represent 10% deviation. The drag force was calculated in both cases using the standard approach that relies on a rescaling of the fluid-particle interaction force.

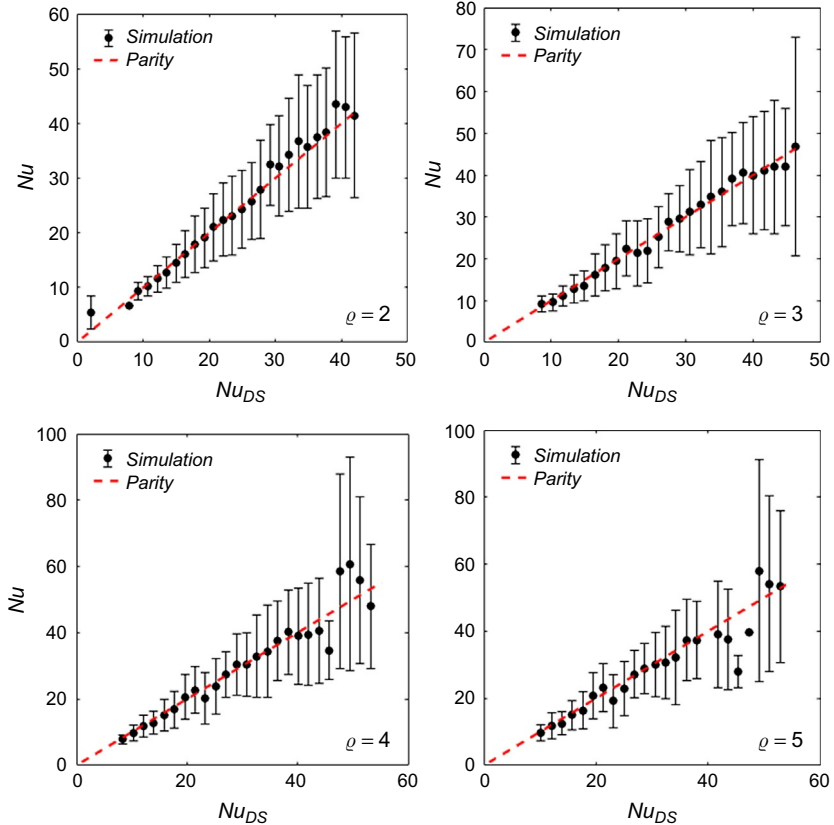


**Fig. 13** Parity plot of average Nusselt number computed in our recent study (Municchi and Radl, 2018, averages are represented as *dots* and the *errors bars* extend to two standard deviations) and a corrected version of a popular correlation (Deen et al., 2014). The definition of the Nusselt number is based on filtered fluid temperatures. Different panels refer to different values of the dimensionless filter size  $\varrho$ .

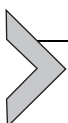
to calculate statistics was lower due to computational reasons, Municchi and Radl, 2018). Thus, it appears that the currently most plausible correlation for the Nusselt number is:

$$Nu = N_{\text{corr}, \text{Sun}} \left[ \begin{aligned} & \left( 7 - 10\phi_f + 5\phi_f^2 \right) \left( 1 + 0.17 Re^{1/5} Pr^{1/3} \right) \\ & + \left( 1.33 - 2.31\phi_f + 1.16\phi_f^2 \right) Re^{7/10} Pr^{1/3} \end{aligned} \right], \quad (40)$$

$$N_{\text{corr}, \text{Sun}} = \left[ 1 - 1.6\phi_p\phi_f - 3\phi_p\phi_f^4 \exp \left( -Re_p^{2/5}\phi_p \right) \right]^{-1}. \quad (41)$$

The above correlations can be used in case spatially filtered data for the fluid temperature are available, i.e., in case PU–EL–based models are used.

We note in passing that an alternative route for correlating heat transfer coefficients is based on relating them to drag coefficients, i.e., assuming an analogy between heat and momentum transfer. Indeed, our previous work ([Municchi and Radl, 2017](#)) indicated that such an analogy exists. Such an analogy approach is especially appealing in case per-particle drag coefficients are available, since it suggests that then also per-particle heat transfer coefficients can be calculated with ease.



## 5. RECENT DEVELOPMENTS FOR CLOSURES DESCRIBING TRANSFER RATES IN MESOSCALE MODELS

### 5.1 Effects Due to Differences in the Mean Particle Speed: The Fluid-Mediated Particle–Particle Drag

It remains to discuss the effect of relative particle motion on the drag force. This is since the closures detailed in [Section 2.5.1](#) are only valid for situations in which all particles move with the same speed. In case particles move relative to each other, and the suspension is characterized by a high Stokes number and low Reynolds number, [Yin and Sundaresan \(2009\)](#) proposed the following modified closure for the drag force:

$$\mathbf{f}_{d,i} = V_{p,i} \left[ \beta_{p,i} (\mathbf{u}_i - \mathbf{v}_i) + \sum_{i \neq j} \beta_{p,\text{FMPP},ij} (\mathbf{v}_j - \mathbf{v}_i) \right]. \quad (42)$$

Here,  $\beta_{p,\text{FMPP},ij}$  is a “fluid-mediated particle–particle” friction coefficient that quantifies the effect of velocity differences between individual particle species. It is important to note that this type of drag modification assumes that particles of the same species move with identical speed. Thus, the “species-based” granular temperature is zero (this is important, since it differentiates the fluid-mediated particle–particle drag from the effects that are discussed in [Section 5.2](#)). Sundaresan and coworkers later showed that the above idea is also valid for nonzero Reynolds numbers ([Holloway et al., 2010](#)). In the same manner as for fixed bed drag closures, the above fluid-mediated force closure has been investigated in the context of EE models. Hence, it is only able to predict the *ensemble-average* drag force acting on particles—not per-particle values for the drag.

## 5.2 Effects Due to Particle Agitation

Along a similar line of thoughts as the discussion in Section 5.1, one can argue that the (average) drag force should be some function of the particle agitation, i.e., the particles' granular temperature. Such an idea was followed recently by two groups: (i) the group around Kuipers suggested adding a "particle mobility" contribution to the drag force coefficient experienced by a static array of particles (Tang et al., 2016). This mobility contribution is linearly dependent on a granular temperature-based Reynolds number. Hence, it is most relevant for intermediate to high Reynolds number flows and always leads to an increase of the drag (compared to that of a fixed bed) in case particles are agitated. (ii) The group around Sundaresan has also investigated the effect of the mobility of particles, but quantified it with a Stokes number (Rubinstein et al., 2016). This group explored rather low Reynolds numbers flows over a large range of Stokes numbers and particle concentrations. Interestingly, this group finds a lower drag for lower Stokes numbers, i.e., a negative correction to the fixed bed drag in case particles are mobile. An opposite trend was predicted by the Kuipers group (Tang et al., 2016).

## 5.3 Cross Effects

Another fact that is often dropped in suspension flow simulations are cross effects: such effects occur in case of extreme heat transfer rates from the particle surface, since then the particle-near fluid may experience significantly higher temperatures (Ganguli and Lele, 2016). This leads to effects caused by buoyancy and the change of physical parameters (e.g., the gas viscosity). Since rigorous closure models are often not available, a carefully conducted preliminary analysis using dimensionless parameters (e.g., the Grashof number) is helpful in such cases. The interested reader is referred to the Appendix of Tenneti et al. for a more detailed discussion of such effects (Tenneti et al., 2013).

In summary, the closure of Beetstra et al. (2007) is still frequently used, often without correction for polydispersity, the particles' relative speed, or cross effects. Moreover, the above drag closures can only predict the average force acting on an ensemble of particles, but not an individual particle. All these limitations should be taken into account when applied to EE or PU-EL models once per-particle drag correlations are established. The next section illustrates a possible pathway to achieve such an improvement.

## 5.4 Variability of the Exchange Coefficients

There has been a recent interest to quantify the variability of the per-particle drag coefficient in dense suspensions with the ultimate goal to establish corresponding closures. An early example of this trend is the work of the Kuipers group (Kriebitzsch et al., 2013). More recently, Deen and Kuipers made an effort to characterize the variability of mass transfer coefficients as well (Deen and Kuipers, 2014b). As outlined in Section 4.2.3, it is of paramount importance to define which average fluid quantity was used to calculate exchange coefficients. In most of the previous works, such quantity was obviously motivated by simple Euler–Euler models: for example, Deen and Kuipers use a slice-based cup-mixing temperature (which would be available in a one-dimensional version of an EE model) to calculate the distribution of mass transfer coefficients (Deen and Kuipers, 2014b). It is not surprising that such a choice leads to a very broad distribution of the heat transfer coefficient, and little sense could be made of such data in the past.

What follows is a summary of our recent activities (Municchi and Radl, 2017) to quantify the variability of exchange coefficients in mono- and bidisperse suspensions using the filtering approach.

### 5.4.1 Drag

With respect to the drag, it is instructive to consider the distribution of a dimensionless per-particle drag force, as well as the trend of the corresponding scaled standard deviation as a function of the average drag on the particles. Such data is shown in Fig. 14 and reveal—surprisingly—no significant

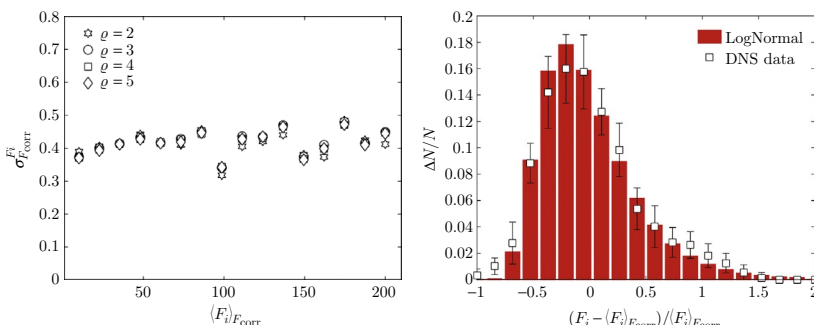


**Fig. 14** Scaled standard deviation of the per-particle drag force (left panel), as well as number-based distribution of the relative deviation of the conditionally averaged drag force from its ensemble average (right panel; the error bar length corresponds to two standard deviations of the samples in each bin).  $\rho$  is the dimensionless filter size (Municchi and Radl, 2017).

dependence of the relative standard deviation from the mean (ensemble-average) drag coefficient  $\langle F_i \rangle$ .

This suggests that the relative deviation of  $F_i$  from  $\langle F_i \rangle$  can be assumed to be approximately constant. Specifically, values for the standard deviation ranged from 32% to 52% which is generally attributed to the presence of preferred pathways for fluid flow through the particle array. We note in passing that this is in line with previous results in the field (Kriebitzsch et al., 2013) as recently discussed in our previous work (Municchi and Radl, 2017).

Also, the lack of a functional dependence on the mean drag coefficient results in a similar distribution for the relative deviations at different average drag coefficients  $\langle F_i \rangle$ . This suggests representing the stochastic fluctuation of the drag force using a modified log-normal distribution. This is in contrast to previous work that considered a Gaussian distribution (Kriebitzsch et al., 2013). Our choice of a log-normal distribution is motivated by the following facts:

- i. A log-normal distribution is defined in the range  $[0, \infty]$  and, thus, naturally predicts a minimum allowed value for the drag coefficient.
- ii. As can be seen from Fig. 14, the distribution of relative deviations is skewed.
- iii. The chosen log-normal distribution can be defined using only one parameter (i.e., the standard deviation), and it was demonstrated that this parameter is approximately constant within the range of parameters used in our study. In fact, physically, the minimum allowable value for the relative deviation of  $-1$  (i.e., zero drag force) and the expectation value is, by definition, equal to zero. This results in a standard log-normal distribution with a mean value equal to 1.

The choice of a log-normal distribution also allows the stochastic drag coefficient model to be efficiently implemented in PU-EL codes: if  $\epsilon_i$  is a randomly generated number between 0 and 1, the value of the fluctuating component of the per-particle drag coefficient can be calculated via an inverse error function that can be tabulated ( $\beta$  is the lower bound of the function and equals  $-1$ ;  $\alpha_F$  is discussed below):

$$F_{i,\sigma} = \beta + \exp \left[ \operatorname{erf}^{-1}(2\epsilon_i - 1)\sqrt{2}\alpha_F \right] \quad (43)$$

In case the coefficients are assumed to be constant (as in our study) the whole expression above can be tabulated before starting the computation. While the above equation can be used to compute the per-particle relative deviations from  $\langle F_i \rangle$ , the important question remains on how this random deviation should be evolved in time. For the time being we note that our

model would allow assigning a specific value for the drag coefficient fluctuation to each particle, and keeping this value throughout a PU-EL simulation.

Finally, the dimensionless drag force acting on a particle  $i$  can be computed from:

$$F_i = F_{i,\text{corr}}(1 + F_{i,\sigma}) \quad (44)$$

However, it should be noted that in the limit of infinite dilution and zero Reynolds number, the above stated simple model for the drag force fluctuation (i.e., a constant value) is predicting a drag force fluctuation between  $-1$  and  $2$ . Clearly, within this limit, the resulting drag should return Stokes drag law (i.e.,  $F_i = 1$ ). A model for the drag force fluctuation—similar to that shown above—is able to consistently take this limit into account only when one ensures that a suitable expression for the standard deviation  $\alpha_F$  is provided. If all the particles tend to experience the same drag force, the modified log-normal distribution must tend to a Dirac delta function, i.e.,  $\alpha_F = 0$ . Future exploration of such a range of parameters is required in order to obtain a suitable expression for  $\alpha_F$ .

Another approach that is less consistent, but perhaps more practical and applicable, consists in calculating the particle-based drag force using the following expression:

$$F_i = 1 + \gamma_F F_{i,\text{corr}} \left( 1 - \frac{1}{F_{i,\text{corr}}} + F_{i,\sigma} \right) \quad (45)$$

Where a simple functional form for the unknown function  $\gamma_F$  would be the relation:

$$\gamma_F = \frac{F_{i,\text{corr}} - 1}{F_{i,\text{corr}}} \quad (46)$$

It is clear that using the above definition for  $\gamma_F$  enforces the Stokes limit, while it approaches the original closure (i.e.,  $F_i = F_{i,\text{corr}}(1 + F_{i,\sigma})$ ) for large values of  $F_{i,\text{corr}}$ . Since only relatively large Reynolds numbers were probed so far by us, future work is needed to justify the above presented drag force model for drag coefficients close to unity.

#### 5.4.2 Heat and Mass Transfer

Examining the distribution of the per-particle Nusselt number reveals an interesting finding: again one can observe that the scaled standard deviation is approximately constant for the Nusselt number (see Fig. 15), and the

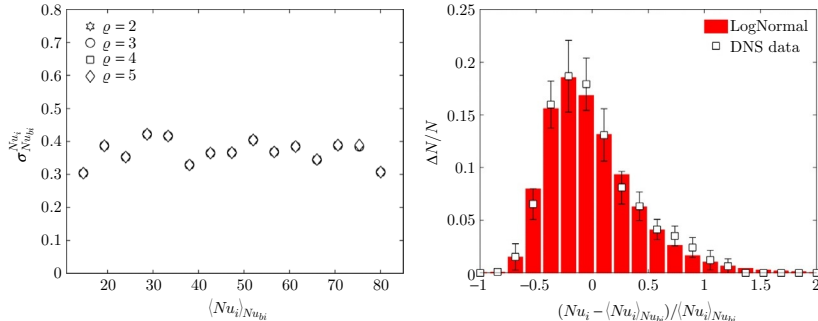


**Fig. 15** Scaled standard deviation of the per-particle Nusselt number (*left panel*), as well as number-based distribution of the relative deviation of the conditionally averaged Nusselt number from its ensemble average (*right panel*; the error bar length corresponds to two standard deviations of the samples in each bin).  $\varrho$  is the dimensionless filter size (Municchi and Radl, 2017).

standard deviation ranges from approximately 30%–45%. Following the same approach as for the drag, one can propose a model for the per-particle Nusselt number based on a log-normally distributed variable (for the fluctuations of the Nusselt number refer to Fig. 15).

Compared to the drag coefficient, the log-normal distribution for the Nusselt number is more peaked (i.e., the standard deviation is smaller), and therefore necessitates the use of an  $\alpha_{Nu}$  parameter instead of the corresponding parameter for the drag. In order to represent our PR-DNS data reasonably well, a value of  $\alpha_{Nu}=0.336$  is recommended.

On a final note, one should highlight the importance of ensuring that the predicted Nusselt number approaches the correct values in the limit of infinite dilution and creeping flow. Ideas on how to ensure this have been provided in a recent publication (Municchi and Radl, 2017).

## 5.5 Wall Effects

Confined suspension flows are a topic of active research since they are of use in a wide range of industrial processes like energy storage, heterogeneous catalytic reactors, or fluid–particle separation processes conducted in micro-channels. Also, one might speculate that confinement effects in suspension flows become even more important in the near future: for example, 3D printing technology aiming on producing materials capable to be used at high temperatures (e.g., metals or ceramics) is already reality. This enables the use of complex geometries with characteristic dimensions closer to that of the suspended particles. In such systems wall effects will play a central role.

In addition, the accurate modelling of momentum, heat, and mass transport in dense gas–particle systems is of pivotal importance for designing chemical reactors (Dixon, 2017).

Fig. 16 illustrates a typical temperature distribution in a confined packed bed. It is clearly visible that the fluid velocity is strongly nonuniformly distributed at the top of the particle bed, leading to the formation of jets that originate from the gaps between particles. Consequently, one might question the validity of established correlations for both drag and heat transfer rates in case

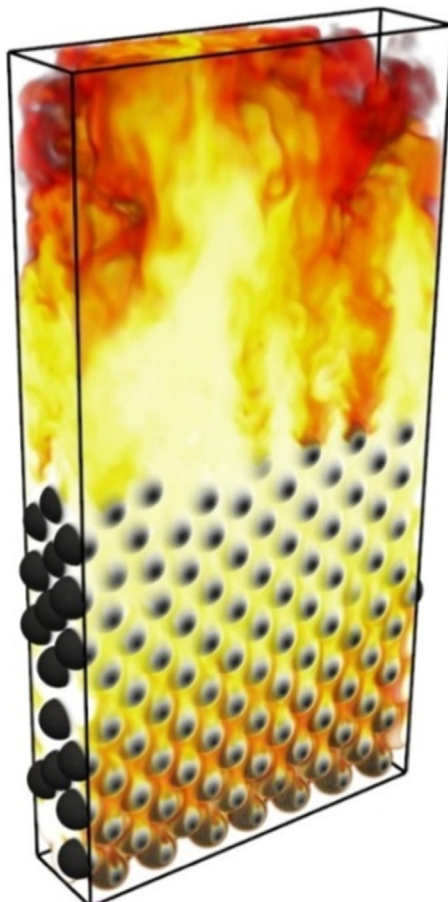


**Fig. 16** PR-DNS data illustrating the fluid temperature field when cooling a bed of particles that is confined by walls (white corresponds to high temperature, dark colors to low temperature).

particles are close to walls. Also, it is clear that suspended particles that are much smaller than that constituting the bed will be transported more quickly in the wall near region due to jet formation. Hence, one could speculate that wall effects are especially important in case of polydisperse suspensions.

A first step to systematically investigate these aspects would be to quantify wall effects in an isolated fashion, i.e., separate them from the curvature effect that is typically included in the analysis (de Klerk, 2003; Mueller, 1992; Theuerkauf et al., 2006; van Antwerpen et al., 2010). Also, little is known for more dilute and moderately dense suspensions, since most previous work explored packed beds only. Considering a wider parameter space is, however, essential when building a robust, generally applicable simulation model. In what follows a brief summary of our recent attempts to perform such a systematic study is presented. The focus was hereby to answer the fundamental question on how one should correct transfer coefficients in PU-EL-based simulations that involve walls. This was achieved by running a large set of PR-DNS. A snapshot of a corresponding simulation result for the temperature distribution is shown in Fig. 17. For details related to this analysis, the interested reader is referred to our latest publication (Municchi and Radl, 2018).

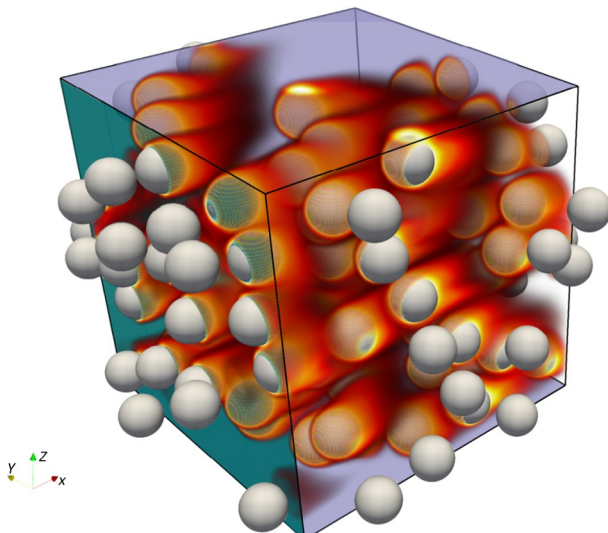


**Fig. 17** Typical result for the temperature distribution in a confined gas–particle suspension (particles are confined by walls in the z-direction; the other directions are periodic; the particles do not move relative to the adiabatic walls; particles are kept at a fixed temperature).

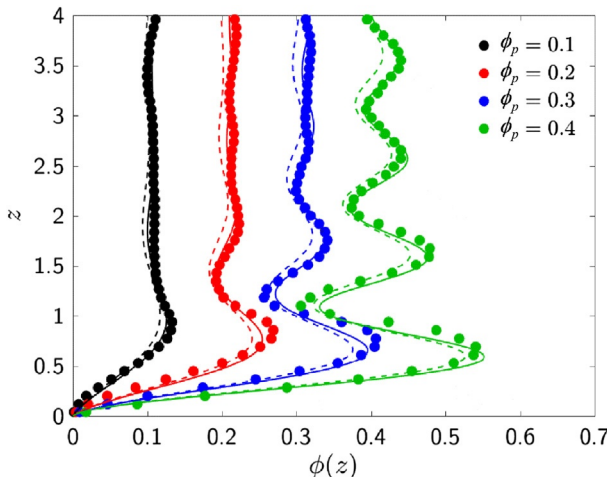


**Fig. 18** Average particle volume fraction as a function of the wall normal distance for various values of the average particle volume fraction in a confined bed of otherwise randomly arranged particles (*dots* indicate simulation data, *continuous lines* use the bulk voidage in the model equation, whereas *dashed lines* use the average voidage; [Municchi and Radl, 2018](#)).

### 5.5.1 Particle Concentration and Flow Profiles

Fig. 18 shows the wall normal profile of the particle volume fraction for different values of  $\phi_p$ , which represents the average particle volume fraction in the domain. In current literature, these profiles are often called *wall radial distribution function* due to the cylindrical geometries employed in their evaluation. In what follows it is useful to consider these profiles as perturbations with respect to the homogeneous (bulk) region. From Fig. 18 one can clearly see that both (i) the absolute amplitude and (ii) the wave number of the perturbation are larger for larger values of  $\phi_p$ . This can be related to the higher degree of order that the particles experience near the wall at higher packing fractions.

This wall-induced perturbation of the particle volume fraction has been studied in literature for the densely packed spheres in cylindrical containers. Several correlations were proposed which are all limited to cylindrical coordinates and high packing fractions. Motivated by the previous considerations regarding the behavior of the voidage ([Mueller, 1992](#)), the following functional form that relaxes this constraint is proposed:

$$\phi(z) = \phi_b \{ 1 - J_0(\kappa_1 z) \exp[-\lambda_1 z] \} \quad (47)$$

$$\kappa_1 = 0.875 + 8.55 \sqrt{\phi_b} \quad (48)$$

$$\lambda_1 = 0.461 + 0.409 \sin(7.42 \phi_b + 0.327) \quad (49)$$

Here  $\phi_b$  is the particle volume fraction far away from the wall. This value is unknown in case of a finite domain size, but can be related to the average particle volume fraction (Municchi and Radl, 2018).

The perturbation to the particle volume fraction shown in Fig. 18 gives rise to statistically inhomogeneous velocity (and temperature) fields. Thus, these flow variables are a function of the wall normal distance. An illustration of this behavior is shown in Fig. 19. An especially interesting trend is observed for the mean temperature: it appears that a layer with almost constant temperature gradient normal to the wall is formed. This “boundary layer” is only weakly pronounced for dilute systems (i.e.,  $\phi_p = 0.1$ ). This is not directly observable from Fig. 19 since the temperature profile is scaled with the bulk temperature. The latter is strongly decreasing for decreasing particle concentrations. Hence, considering the original temperature profiles, one would observe a significantly larger gradient for larger values of  $\phi_p$  compared to  $\phi_p = 0.1$ .

### 5.5.2 Drag

In order to quantify the effect of wall boundaries on the drag coefficient and Nusselt number, relevant statistical data was collected using an approach similar to that used in Section 5.4. However, this time all data was binned with respect to the particles’ wall normal distance, necessitating a much larger amount of raw data to reduce noise in the calculated averages: For each value of the mean particle concentration, data from simulations involving approximately 4000 particles was used. As a key result, it was observed that (as for the wall normal velocity and temperature profiles) the dependence on the

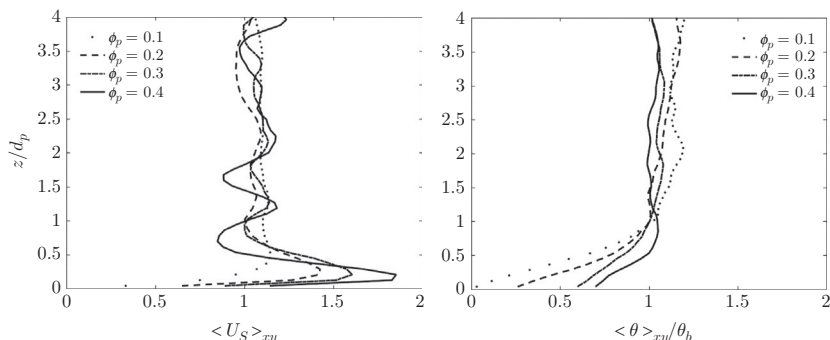


**Fig. 19** Wall normal profiles of the average fluid speed (left panel; the speed is normalized with the global mean speed in the simulation domain), as well as the average fluid temperature (right panel; the temperature is normalized with the fluid’s bulk temperature) for a Reynolds number of 400 (Municchi and Radl, 2018).

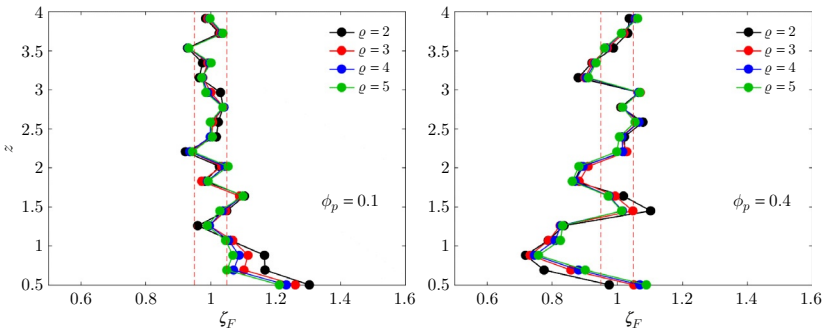


**Fig. 20** Wall correction to the drag coefficient as a function of the filter size  $q$  and the average particle volume fraction  $\phi_p$ . Red dashed lines represent deviations of  $\pm 5\%$  from the bulk value.

Reynolds number can be easily dropped once the drag coefficient and the Nusselt number are related to a typical bulk value (this is true for the investigated range of Reynolds numbers, i.e., 100–400). Hence, a master curve for the drag correction can be constructed, which is shown in Fig. 20. Both wall normal profiles have a maximum corresponding to the first particle layer (i.e.,  $z=0.5$ ). A minimum develops when increasing the average particle concentration  $\phi_p$ . It can also be seen that the intensity of the perturbations becomes larger when increasing  $\phi_p$ , which is related to the stronger perturbation in the particle concentration profile. No significant effect of the filter size  $q$  was observed, hinting to the fact that filtered fluid velocities are almost independent of  $q$ .

### 5.5.3 Heat and Mass Transfer

Results for the wall correction to the Nusselt number are plotted in Fig. 21. Our results indicate that Nusselt number corrections are in general stronger as those for the drag. This can be tentatively explained by the combined effect of flow (i.e., the velocity gradient) and the abnormal temperature distribution experienced by wall-near particles (see Fig. 19, right panel).

Furthermore, the filter size  $q$  has a significant effect on the Nusselt number correction. This effect is extreme for particles closest to the wall, i.e., that located at  $z=0.5$ . The enormous sensitivity to  $q$  observed for the corrections to the Nusselt number is in contrast to the correction for the drag coefficient. The latter are almost insensitive to the filter size. One could speculate that the origin of this difference is again the abnormal temperature distribution in the vicinity of the wall: Depending on the filter size, a different *filtered*

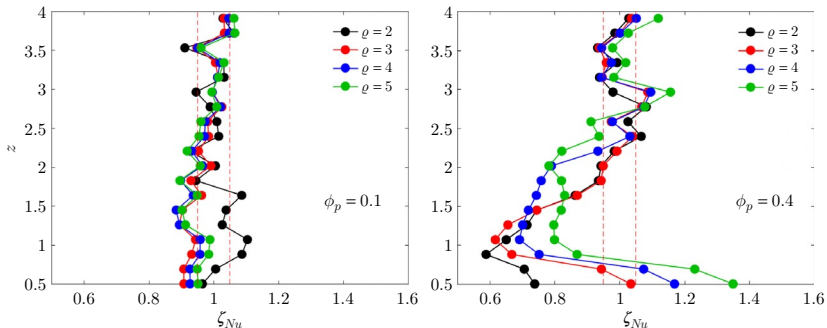


**Fig. 21** Wall correction to the Nusselt number as a function of the filter size  $q$  and the average particle volume fraction  $\phi_p$ . Red dashed lines represent deviations of  $\pm 5\%$  from the bulk value.

temperature is experienced by individual particles. Specifically, smaller filter sizes  $q$  will lead to lower values for the average fluid temperate as can be anticipated from Fig. 19, right panel. This will lead to a larger difference between the particle and fluid temperature, i.e., the driving average temperature difference. In simple words, a smaller filter size (or a smaller grid size) results in wall-near particles experiencing a different fluid temperature in PU-EL models. Thus, for a given fluid-particle heat flux, the Nusselt number must decrease for a decrease in the filter size in case particles are located in the “temperature boundary layer” observable in Fig. 19. Also, this is exactly what was observed for the correction of the Nusselt number (see our data for  $\phi_p=0.4$  in Fig. 21). In case particles are outside of the “temperature boundary layer,” or this layer is only weakly pronounced, the above argument on the filter size effect is expected to break down (see data for  $\phi_p=0.1$  in Fig. 21).

## 6. RECENT DEVELOPMENTS FOR CLOSURES DESCRIBING MESOSCALE PHENOMENA

Simulations of the mesoscale models discussed in Section 5 provide data that is useful to understand flow phenomena on intermediate scales. In what follows, some developments in this fields are summarized that aim on the quantification of such phenomena in order to provide closure information for the next level on the modelling hierarchy, i.e., macroscale models. These developments are documented by four examples that are thought to best illustrate recent trends, and that were triggered by advances in the field of mesoscale simulations.

## 6.1 Sequential Fluid and Particle Coarsening

Model coarsening (i.e., establishing closures for macroscale models based on mesoscale simulation) in the context of fluid–particle suspensions has traditionally aimed on using EE models (Holloway, 2012). The key motivation behind this is twofold: first, EE models require less computational resources to support closure development with data. Second, latest kinetic theory-based EE models can be considered equivalent to EL models, at least with respect to picturing relevant clustering phenomena in noncohesive monodisperse fluid–particle suspensions (Fullmer and Hrenya, 2016). Especially, kinetic theory-based rheological models are well developed and are—at the moment—clearly superior to parcel-based strategies (i.e., EL models that do not track individual particles). The latter are often based on heuristic arguments (Snider, 2001).

Still, coarsening of EL model offer advantages over an EE-based strategy:

- (i) EL-based models can be used to consider wider spectra of physical models, e.g., cohesive interparticle forces, the fluctuation of the per-particle drag force (Kriegeritzsch et al., 2013; Municchi and Radl, 2017), or nonspherical particles. This increases the applicability of model coarsening strategies, since industrially relevant systems may be severely affected by cohesive forces or particle shape. The recent study of Ozel et al. (2017) illustrates this advantage of EL models when deriving models that describe mesoscale phenomena in an excellent way.
- (ii) EL models offer a natural tracking of per-particle quantities, e.g., the particle’s composition, density, liquid content, or intraparticulate concentration and temperature profiles. This is of immediate relevance for applications in the field of reactive suspensions.
- (iii) Coarsening can be performed *sequentially* for the fluid and particle phase when adopting an EL model. As shown in Fig. 22, this offers the key advantage that effects due to fluid and particle coarsening can be separated (Ozel et al., 2016; Radl and Sundaresan, 2014). Such an improved understanding of these two coarsening effects is helpful to improve numerical schemes, or to guide closure development.

When adopting an EL approach for coarsening one arrives formally at an EL-Large Eddy Simulation (LES) approach. Marchioli provides a recent review of EL-LES with a focus on one-way coupled dilute fluid–particle flows (Marchioli, 2017). He correctly states that modelling the fluid velocity seen by the particle is the key challenge for such an approach. Specifically, the challenge is to predict the fluid velocity fluctuation at the particle location, for which a variety of “subgrid-scale” (SGS) closure strategies exist. Unfortunately, Marchioli states that:

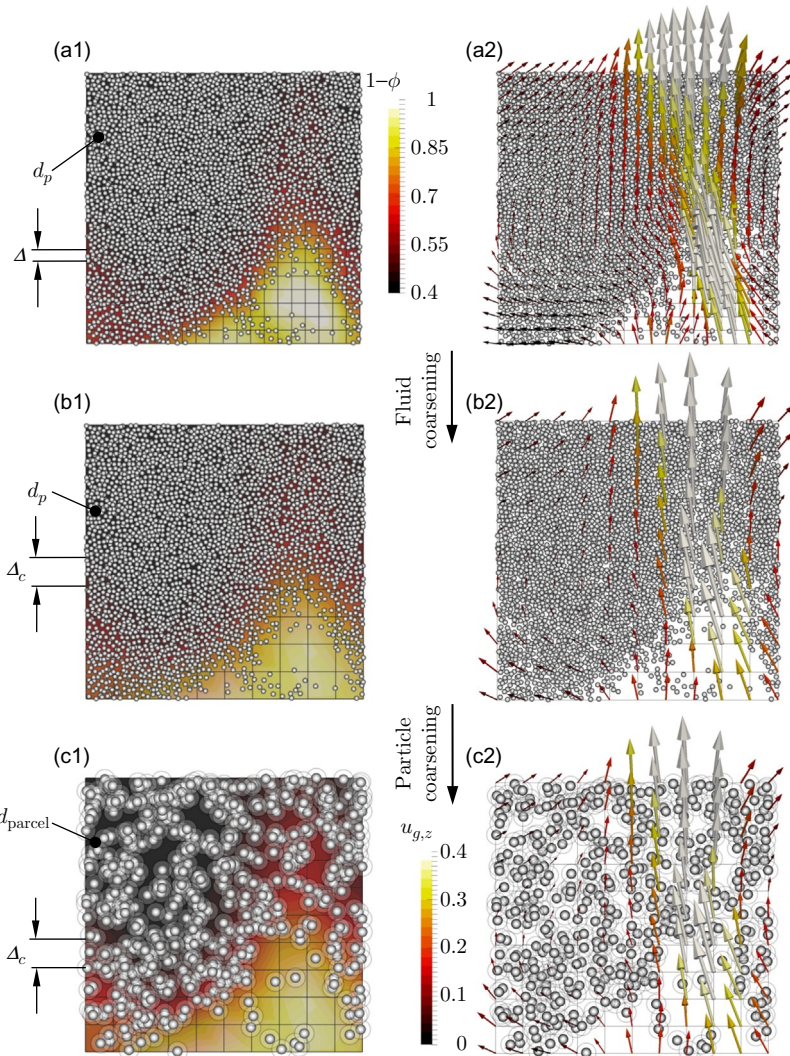


**Fig. 22** The concept of sequential fluid- and particle-coarsening in the context of EL models (a1, b1, c1: colors indicate the local voidage as per the top colorbar; a2, b2, c2: colors indicate the vertical fluid speed as per the bottom colorbar;  $d_{\text{parcel}}$  refers to the diameter of the opaque spheres in panel c1 and c2; the semitransparent circles illustrate the influence region of each parcel,  $\Delta$  identifies a cell size).

“...no particle SGS models have been developed for semi-dilute or dense suspensions, which would require specific source terms to account for two-way coupling (inter-phase momentum exchange) or four-way coupling (collisions) in the governing equations.”

*Marchioli, 2017*

Thus, one cannot adopt EL-LES closure approaches for dense suspensions in a straightforward manner. Instead, one is—more or less—forced to rely on a somewhat more pragmatic approach that has been outlined in [Section 2.6.2](#).

## 6.2 Non-Boussinesq Stress Models

Current models describe mesoscale solids stresses—in analogy to the Boussinesq approximation for turbulent stresses—based on a filtered solids pressure and a filtered solids viscosity. This previously adopted approach is therefore heavily reliant on the assumption that mesoscale velocity fluctuations of the solid phase are isotropic. However, latest developments in the field of multiphase Reynolds stress models (RSMs)—even for comparably dilute particle laden flows—indicate that mesoscale stresses are highly anisotropic ([Capecelatro et al., 2016](#)).

The group around Amini (SINTEF, Norway) has attacked the associated question whether stress models that are beyond the Boussinesq assumption can be built. While limited to a two-dimensional proof of principle study, the first fruits of this research could be harvested just recently ([Cloete et al., under review](#)). One core result is that mesoscale shear stresses do not correlate well with the corresponding components of the filtered shear rate tensor. In other words, the core issue is the assumption inherent to a scalar mesoscale viscosity. Furthermore, it was found that the conventional isotropic mesoscale pressure approach offers a reasonable approximation of the filtered resolved data.

Subsequently, a rigorous marker screening study was performed, and it was found that products of velocity gradients were much better markers compared to the shear rate ([Cloete et al., under review](#)). [Fig. 23](#) illustrates this finding, in which the particle-phase velocity gradient product marker was calculated via:

$$M_{xy} = \overline{\alpha}_s \left( \frac{d\bar{\mathbf{v}}_x}{dx} \frac{d\bar{\mathbf{v}}_y}{dx} + \frac{d\bar{\mathbf{v}}_x}{dy} \frac{d\bar{\mathbf{v}}_y}{dy} \right) \quad (50)$$

This gives new hope that closures for each component of the mesoscale stress tensor can be built with relative ease. Hence, these closures may rely on tensor-valued markers.

## 6.3 Closures for Cohesive Systems

Cohesive forces play a central role in many industrial particle processes, e.g., fluidization of fine dry powders, or wet fluidization (e.g., wet granulation, fluidized bed drying, fluid coking, etc.). Taking the example of

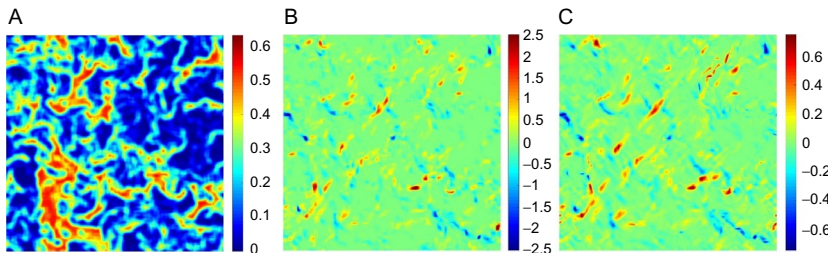


**Fig. 23** Comparison of the particle-phase mesoscale shear stress to its corresponding gradient-based marker for a domain-averaged solids volume fraction of 0.2 and a dimensionless filter size of 3.47. (A) The filtered solids volume fraction, (B) filtered shear stress  $\hat{\Sigma}_{s, \text{fil},xy}$ , (C) gradient-based marker  $M_{xy}$ . Figure by courtesy of Schalk and Jan Hendrik Cloete, as well as Shahriar Amini, SINTEF, Norway.

dry powder fluidization, and focusing on the formation of bubbles, a number of breakthrough computational studies have been published recently. Building on pioneering work in the field (Rhodes et al., 2001; Ye et al., 2004), two recent studies stand out: (i) the work of Galvin and Benyahia showed how particle size distributions and cohesion affect fluidization properties (Galvin and Benyahia, 2014). (ii) Sundaresan and coworkers (Gu et al., 2016a, b) found that even two particle size classes and cohesion are enough to predict the fluidization regime of Geldart A particles. These previous studies were descriptive and supported findings on bubble sizes. While this is not of immediate relevance to improve closures, they contributed to speeding up PU-EL-based simulations by proposing stiffness correction rules. Such rules are of large interest in the field (Hærvig et al., 2017).

Recent developments in the field of wet fluidization were—*inter alia*—based on a more profound understanding of liquid bridge formation dynamics (Wu et al., 2016, 2017). This improved understanding of how liquid bridges form allows to map the physical properties of a wet fluidized bed to its expected fluidization state (Boyce et al., 2017; Wu et al., 2018). Also, a first step toward using simulation data to develop a quantitative description of mesoscale phenomena (i.e., agglomerate formation, and the associated increase in the fluid–particle slip velocity) was already taken (Girardi et al., 2016). More recent studies (Wu et al., 2018) confirm these results of Sundaresan and coworkers. Future work can now expand the ideas that have been introduced with respect to coarsening EL models for wet granular systems via filtering. Thus, there is hope to arrive at macroscale models of wet fluidized systems that are of immediate relevance for industry.

Finally, a note must be made related to cohesive forces developing in electrostatically charged gas–particle suspensions: The complexity inherent to tribocharging has long prevented accounting for electrostatic forces when simulating such systems. Fortunately, some key challenges have been overcome just recently (Kolehmainen et al., 2016, 2017a; Shinbrot et al., 2017). A central result from these studies is that there is now an improved understanding how simulations should be performed, e.g., with respect to stiffness scaling (Kolehmainen et al., 2017b). Still, closures for predicting drag forces or stresses useful for macroscale models have not been distilled so far. Such models are clearly needed as summarized in a recent review (Fotovat et al., 2017). That the development of such mesoscale models for electrostatically charged fluid–particle systems is hindered by the enormous computational cost (of EL models) is clear: as of now, the typical amount of particles that can be studied with high fidelity tribocharging models is in the order of 50,000 (Fotovat et al., 2017). Unless rigorous EE models for modelling cohesion and charge uptake in tribocharged fluid–particle systems are fully developed, this limitation will persist. Fortunately, first steps in developing such EE models have been made just recently (Kolehmainen et al., 2017c).

## 6.4 Closures Based on a Deconvolution Approach

The concept of deconvolution analysis has been widely exploited in the field of single-phase turbulent flow as a promising approach for so-called structural closures in the context of LESs (Sagaut, 2006). This type of closures relies on no a priori knowledge of the flow phenomena described, but is solely based on a formal description of the spatial filtering procedure. The main idea of deconvolution analysis is the inversion of the filtering procedure, i.e., to employ a “defiltering” procedure to obtain unfiltered quantities (e.g., mesoscale stresses) from filtered data. The latter is provided by a macroscale model, and hence available at a comparably coarse computational grid resolution level. “Defiltered” quantities can then be used in a straightforward manner to describe the effect of the phenomenon of interest (e.g., mesoscale stresses caused by particle clustering). Consequently, this information can be used to close the macroscale model equations. Closures based on a deconvolution analysis are typically referred to as “approximate deconvolution models” (ADM), a wording that might be misleading since no (physical) model equations are actually solved.

ADM has been introduced to the field of gas–particle flows already in 2006, however, only in the context of relatively dilute flows (Kuerten, 2006). For dense flows, an attempt to test the virtues and merits of ADM

was made only recently (Schneiderbauer and Saeedipour, 2018). Specifically, deconvolution was applied to analyze the effect of clustering on the interphase momentum exchange rate, as well as on the mesoscale solids stress in vertical channel flow. It was shown that ADM is indeed a promising alternative to strategies that rely on algebraic closures (e.g., those discussed in Section 6.2). However, this was demonstrated only for small spatial extensions of the filter size, corresponding to comparably fine computational grids to be used when simulating a macroscale model.

Despite the current limitations of ADM-based closures, Schneiderbauer and Saeedipour highlighted two key advantages of such an approach when applied to dense fluid–particle flows (Schneiderbauer and Saeedipour, 2018):

- i. The anisotropy of mesoscale stresses is correctly predicted by the ADM-based closure for the situation of a vertical channel flow. This gives hope that solids stresses can be reliably predicted in flow situations involving walls.
- ii. A number of assumptions when closing the filtered drag force can be dropped, most important that of assuming that the mesoscale correction factors for the drag force are scalar valued.

The application of the deconvolution approach may certainly improve the quantitative understanding of mesoscale phenomena, and hence the quality of closures in the field of macroscale models. Unfortunately, for dense gas–particle flows encountered in large-scale engineering applications (e.g., fluidized beds), ADM appears to be less useful at the moment. This is simply due to the (comparably) fine computational grids that need to be used as already discussed earlier, and due to the lack of benchmark simulations for such applications. Also, factors like (i) the numerically efficiency, and hence the affordability when using deconvolution in the context of macroscale models, or (ii) the ability to include more physics (e.g., polydispersity, species transport, chemical reactions) are currently unexplored and may hinder the widespread use of ADM.



## 7. CONCLUSION AND OUTLOOK

The application of data filtering, i.e., spatial averaging, together with advances in computational tools for predicting dense gas–particle flows in high detail, has equipped researchers with powerful tools to investigate these systems. Combined with a thorough theoretical understanding, these tools have been used to develop new closure to be used in meso- and macroscale models. Mostly, this was limited to monodisperse and noncohesive systems made of spherical particles. Since simulators are increasingly based on the

Euler–Lagrange approach, these limitations can be—hopefully—removed in the near future with relative ease. Certainly, success along this way of thoughts depends on the application. It is certain that cohesive forces caused by electrostatics, as well as polydisperse systems with a broad size distribution offer some of the most significant challenges from the point of computations.

There is a plurality of possible research directions that one could follow, and that rely on spatial averaging as their commonality. Fig. 24 provides an overview of such research areas in which one could branch out. Clearly, the development of closures is certainly the broadest field of application of the filtering approach. However, in parallel it will be necessary to update and upgrade existing models to fully exploit new closures: An example is the new generation of tensor-valued closure laws (e.g., for the mesoscale stress as mentioned in Section 6.2) to be used in macroscale models. Without a significant upgrade of the corresponding tools that simulate these macroscale models, it will not be possible to exploit the predictive capabilities of such new closures.

In what follows, three research directions for which clear research tasks can be defined are summarized in greater detail.

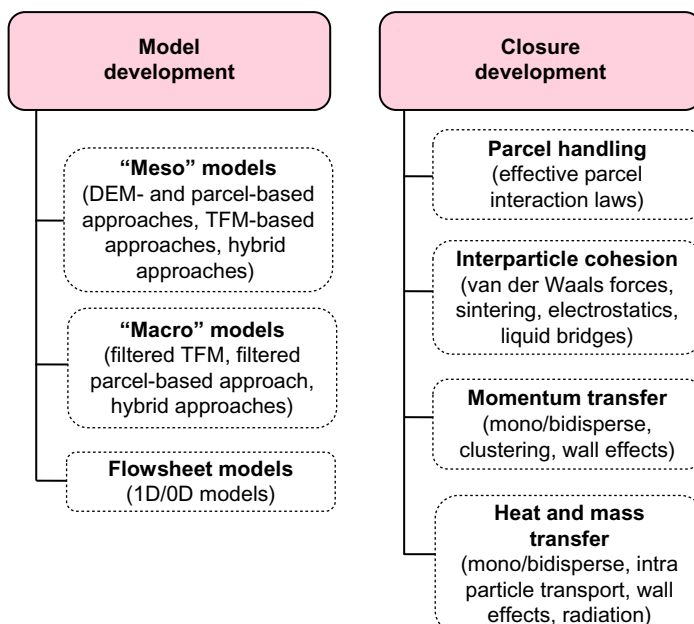


**Fig. 24** Overview of possible future research areas in the field of fluid–particle suspensions that benefit from the development of tools for efficient spatial data filtering.

## 7.1 Research Direction 1: Advanced Euler–Lagrange Models

First and foremost, it would be wise to combine findings between different studies related to fluid–particle drag forces. A prime example are the recent studies of the Kuipers group (Tang et al., 2016) and the Sundaresan group (Rubinstein et al., 2016) on the effect of particle agitation on the drag coefficient. While on a first view, it appears that these studies contradict each other, they most likely probed two different extremes in the large parameter space spanned by sedimenting fluid–particle suspensions. Looking into statistics obtained from spatial data filtering could help to shed light into this possible discrepancy. Some pioneering work has been made that considers the effect of the suspension’s microstructure on the drag (Akiki et al., 2017; Holloway et al., 2012), which could also help to aid in unifying this fuzzy picture. Certainly, such ideas should be extended in the close future.

Second, significant attempts were already made to exploit the key advantages of EL models. These are (i) the ability to study cohesive particulate systems (Girardi et al., 2012, 2016; Greidinger et al., 2014; Ozel et al., 2017), (ii) the natural handling of per-particle and per-contact properties (e.g., size, density, liquid content, liquid bridge volume, (Wu et al., 2014, 2016), or particle temperature), (iii) the ability to resolve intraparticle property profiles (Forgber et al., 2017), (iv) the direct handling of wall collisions, and (v) the direct description of flows involving nonspherical particles.

Macroscale simulations that rely on a verified and validated Euler–Lagrange model would open new research directions, especially for cohesive and polydisperse gas–particle suspensions. Building confidence in such models should mainly focus on improving closure for the drag and the particle–phase stress. Specifically, more robust closures must be build that are applicable to situations involving walls, liquid–particle suspensions, or strongly sheared systems.

## 7.2 Research Direction 2: Broader Application of Filtering Tools

The application of spatial filtering to parameterize closures necessitates the selection of a suitable simulation setup to provide the raw data. So far, mostly periodic domains were chosen. In these systems a nontrivial solution of the governing equations evolves naturally once the initial conditions and the system parameters are appropriately set. For example, in freely sedimenting suspensions such solutions are triggered by an instability mechanism that drives the flow by gravity (Sundaresan, 2003). However, solutions from periodic domains are unsatisfactory to some degree, since it is not known

if these solutions are fully representative of real-world applications. Hence, it would be desirable to compare statistics from periodic domains with “real-world” statistics collected when simulating a specific application. Fortunately, some inspiration for such a future extension can be gained from the related field of turbulent combustion as discussed next. In this field DNS are popular and have become a mainstream already decades ago. The simulation setups used in the field of combustion can be readily mapped to other fields, such as mesoscale EL models of dense suspensions. Specifically, [Moureau et al. \(2011\)](#), as well as [Domingo and Vervisch \(2017\)](#) discuss the state of the art in DNS of turbulent combustion. In these applications, three types of DNS setups are used:

- (i) DNS of canonical flow situations (e.g., forced synthetic turbulence in a periodic domain, [Ten Cate et al., 2004](#)),
- (ii) an “embedded DNS box” approach (i.e., a DNS region is directly coupled to a full LES and runs cocurrently, [Domingo and Vervisch, 2017](#)), and
- (iii) DNS of small domains (this approach is useful for confined particle beds, e.g., see [Singhal et al. \(2017\)](#)).

With respect to (i), the Eswaran–Pope forcing method ([Eswaran and Pope, 1988](#)) is typically employed ([Ten Cate et al., 2004](#)). This approach appears to be suitable also for anisotropic forcing, which is an essential characteristic of gravity-driven instabilities in fluid–particle suspension. An alternative canonical flow situation is simple (turbulent) shear flow as recently demonstrated by the group around Fox ([Baker et al., 2016; Fox et al., 2016](#)). This shear flow setup allows the specification of a mean shear rate as an additional simulation input parameter. Similar pathways could be followed in future, for example, when studying wet fluidized beds. However, one must keep in mind that the parameter space to be explored (e.g., the relative importance of the mean shear rate, or the orientation of gravity relative to mean shear) results in additional challenges with respect to computational effort.

The “embedded DNS box” approach (i.e., item (ii) in the above list) was followed by [Pirker et al. \(2013\)](#) and is also recommended by the recent study of [Domingo and Vervisch \(2017\)](#). This approach was not followed in previous studies that attempted to derive a drag model for clustered gas–particle suspensions. Hence, this approach would offer an interesting alternative to the fully periodic box setup, or the “periodic riser” ([Cloete et al., 2017a, under review; Ozel et al., 2013](#)) approach that is well explored in literature.

The filtering approach discussed in this chapter is certainly not limited to bridging a single gap spanned by two characteristic length scales.

Thus, one may want to use filtering progressively, i.e., obtain filtered models from simulations that already employ a filtered model. However, for such a progressive filtering approach the choice of the simulation domain, including appropriate boundary conditions (and perhaps forcing), is not obvious.

### 7.3 Research Direction 3: Exploration of Intraparticle Transport Phenomena

The new software tool “ParScale” (Radl et al., 2015b) was integrated with the LIGGGHTS® and CFDEM® simulator (results of a typical simulation are shown in Fig. 25). This enhanced simulation platform is now in use to quantify the effect of intraparticle transport phenomena on, e.g., the performance of a heterogeneous reactor. Also, models to predict interparticle heat transfer rates due to radiation are available (Forgber and Radl, 2018). Most important,  $O(10^6)$  particles, each discretized by typically 10 intraparticle grid points,

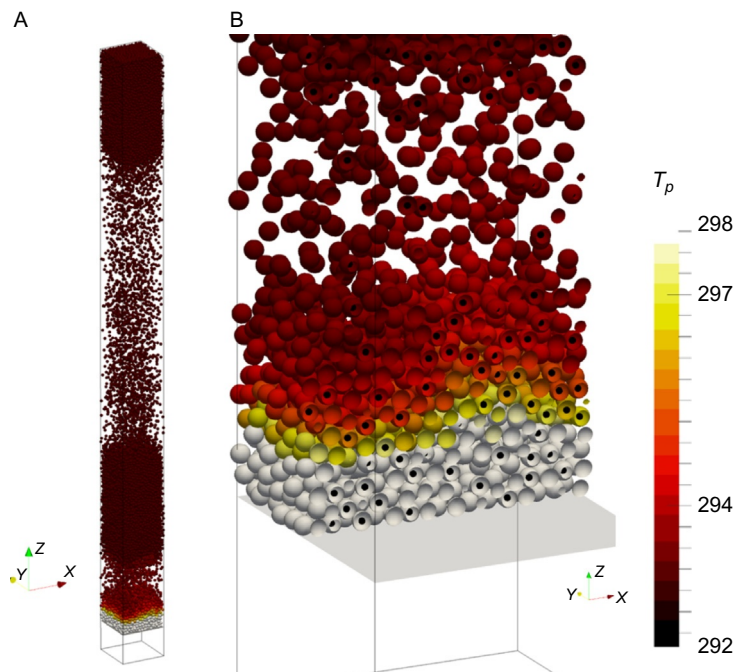


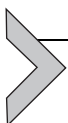
**Fig. 25** Particle temperature distribution  $T_p$  in a heated fluidized bed (Radl et al., 2015a). (A) full system, (B) close-up view near the fluid inlet; 25,000 particles, each particle is discretized using 10 radial grid points; the characteristic Biot number is 16.3, domain width/depth/height:  $15d_p/15d_p/200d_p$ , the domain is  $x$ - and  $y$ -periodic, particle diameter  $d_p = 2$  mm, inlet superficial velocity  $U_s = 2$  m/s, fluid inlet temperature  $T_{in} = 323$  [K].

can be tracked when moving through the simulation domain. The ability to study such a large particle number is achieved by using LIGGGHTS® parallel data containers. These containers solve the issue of efficient data transfer once a particle moves across a processor boundary, and hence a different processor takes over the calculation.

Similar ideas on establishing a similar EL model-based platform were followed by other groups (Oschmann et al., 2016). The latter work used a full (i.e., three-dimensional) discretization of each particle, relying on either a Cartesian or a spherical inner coordinate system. Situations characterized by a small particle Reynolds number (which lead to significant mean temperature gradients in the ambient fluid), as well as situations in which particles are located near walls (Dixon, 2017) may necessitate such a three-dimensional intraparticle discretization. Finally, one must mention the enormous computational expense that is needed to solve EL models with intraparticle discretization. For example, the study of Mahmoudi et al. (2016) considered only a (pseudo) two-dimensional moving bed of particles consisting of a few thousand particles. Clearly, computational efficiency is still a critical bottleneck. It appears that in the coming decade this bottleneck will persist, even though it might be alleviated by the decreasing cost of computing.

## ACKNOWLEDGMENTS

Large parts of our studies cited in this chapter were funded by the European Commission through Grant no. 604656 (NanoSim). The authors of this chapter acknowledge the support of NAWI Graz by providing access to VSC-3 and dcluster for carrying out computer simulations. CFDEM® and LIGGGHTS® are trademarks of DCS Computing GmbH. The authors thank Jakob Redlinger-Pohn (TU Graz) for proof-reading the manuscript.



## APPENDIX. DERIVATION OF AN EULER–LAGRANGE THEORY OF DISPERSED MULTIPHASE FLOWS

In this Appendix, we provide a “bottom-up” derivation of the governing equations for the fluid phase in the frame of an Euler–Lagrange formulation. Specifically, the continuous phase fields are averaged within a volume  $V$  for which no assumption is made with regards to shape or extension. In general  $V = V(\mathbf{x})$ , which defines the spatial coordinate of the averaged fields. In order to simplify the notation, we do not make any distinction between the integration domain and the volume (or mass) enclosed within that domain, i.e.,  $V$  is referred both to the integration domain and its volume.

This Appendix is structured as follows: in [Appendix A.1](#), we define the basic quantities and operators needed to carry out our analysis. Such operators are applied to the microscopic governing equations in [Appendix A.2](#). Finally, in [Appendix A.3](#) we simplify the EL equations through the use of boundary conditions and further assumptions.

## A.1 Definitions and basic results

We define the *mass-based average* (for example, for the velocity field  $u_i$ ) as:

$$\hat{u}_i(\mathbf{x}, t) = \frac{1}{\mathcal{M}_f(\mathbf{x}, t)} \int_{\mathcal{M}_f(\mathbf{x}, t)} u_i(\mathbf{x}', t) d\mathcal{M}_f \quad (\text{A1})$$

Where  $\mathcal{M}_f(\mathbf{x}, t)$  is the fluid mass enclosed in the averaging volume  $V$ . Notice that this quantity is dependent on space and time because (i)  $V$  is a function of the spatial coordinate and (ii) the amount of fluid within  $V$  can change due to the movement of particles and variations in the fluid density.

To find a clearer expression for integral Eq. (A1), we introduce the *phase volume average*  $V_f(\mathbf{x}, t)$ , which is the average over the fraction of the averaging volume that is occupied by the fluid and we apply it to the fluid density field  $\rho(\mathbf{x}, t)$ :

$$\tilde{\rho}(\mathbf{x}, t) = \frac{1}{V_f(\mathbf{x}, t)} \int_{V_f(\mathbf{x}, t)} \rho(\mathbf{x}', t) dV_f \quad (\text{A2})$$

Which, considering that  $\mathcal{M}_f(\mathbf{x}, t) = \tilde{\rho}(\mathbf{x}, t) V_f(\mathbf{x}, t)$ , results in  $d\mathcal{M}_f = \rho(\mathbf{x}, t) dV_f$ , which allows a change of variables in integral Eq. (A1). Notice that  $V_f$  is also a function of space and time, but its time dependence is only due to changes in the dispersion phase, i.e., particles that enter/leave the domain  $V$  or that modify their volume (for example, through shrinking). Therefore, we separate the effect of density variability from the pure geometrical contribution to the total mass of fluid in  $V$ .

Finally, we introduce the *total volume average*, i.e., over the whole filtering volume  $V(\mathbf{x})$ :

$$\bar{\phi}(\mathbf{x}, t) = \frac{1}{V(\mathbf{x})} \int_{V(\mathbf{x})} \phi(\mathbf{x}', t) dV \quad (\text{A3})$$

Where  $\phi(\mathbf{x}, t)$  is the indicator function, which is 1 when  $\mathbf{x}$  lies in the fluid phase and 0 otherwise. Therefore, we can make an additional change of variables, simply by employing  $V_f(\mathbf{x}, t) = \bar{\phi}(\mathbf{x}, t) V(\mathbf{x})$ , therefore obtaining

$dV_f = \phi(\mathbf{x}, t)dV$ . Notice how the time dependence of the integration domain has been removed by introducing  $\phi$ .

In the following, we may use a shorthand notation for the *total volume averaging*

$$\bar{\phi}(\mathbf{x}, t) = \int_V \phi(\mathbf{x}', t) dV \quad (\text{A4})$$

Such notation has the remarkable advantage (over, for example, the classical  $\overline{(*)}$ ) of not hiding the integral nature of the operator while hiding the division by  $V$ , which is not important for the final form of the equations.

All the previous definitions can be employed to highlight how different averaging procedures come into play:

$$\begin{aligned} \frac{1}{\mathcal{M}_f(\mathbf{x}, t)} \int_{\mathcal{M}_f(\mathbf{x}, t)} u_i(\mathbf{x}', t) d\mathcal{M}_f &= \frac{1}{V_f(\mathbf{x}, t)\tilde{\rho}(\mathbf{x}, t)} \int_{V_f(\mathbf{x}, t)} \rho(\mathbf{x}', t) u_i(\mathbf{x}', t) dV \\ &= \frac{1}{V(\mathbf{x})\bar{\phi}(\mathbf{x}, t)\tilde{\rho}(\mathbf{x}, t)} \int_{V(\mathbf{x})} \phi(\mathbf{x}', t) \rho(\mathbf{x}', t) u_i(\mathbf{x}', t) dV = \frac{\bar{\phi}\rho u_i}{\bar{\phi}\tilde{\rho}} = \frac{\tilde{\rho}u_i}{\tilde{\rho}} = \hat{u}_i \end{aligned} \quad (\text{A5})$$

In the following, we will often omit the space-time dependence in order to obtain a compact notation.

We introduce the *surface integral average operator* (i.e., average over the immersed surfaces), which is related to the volume average by:

$$\begin{aligned} \int_V \frac{\partial u_i}{\partial x_i} dV &= \frac{1}{V} \int_V \frac{\partial u_i}{\partial x_i} dV = \sum_{s=0}^{N_s} \frac{1}{V} \int_{S_s} u_i n_{s,i} dS_s = \sum_{s=0}^{N_s} \frac{S_s}{V} \cdot \frac{1}{S_s} \int_{S_s} u_i n_{s,i} dS_s \\ &= \sum_{s=0}^{N_s} \gamma_s \int_{S_s} u_i n_{s,i} dS_s \end{aligned} \quad (\text{A6})$$

Where  $S_s$  is the immersed surface  $s$  ( $N_s$  is the number of immersed surfaces),  $n_{s,i}$  is the  $i$  component of the normal to surface  $s$ , and  $\gamma_s$  is the *specific surface area* of surface  $s$ . Notice that  $N_s$  includes the number of particles  $N_p$  and the other domain boundaries.

Generally, the indicator function can be casted in the following form:

$$\phi(t, x_1, x_2, x_3) = \sum_{i=1}^{N_p} \mathcal{H}[Y_{s,i}(t, x_1, x_2, x_3)] \quad (\text{A7})$$

Where  $N_p$  is the number of particles and  $\mathcal{H}$  is the Heaviside function. The specific shape of an immersed body  $i$  is defined by the function  $\Upsilon_{s,i}$ . Notice that  $\Upsilon_{s,i}$  is zero at the immersed surface and therefore, by the theorem of implicit functions, the gradient of  $\Upsilon_{s,i}$  corresponds to the field of vectors normal to the immersed surface  $i$ .

Therefore, the gradient of  $\phi$  can be evaluated:

$$\oint_V \frac{\partial \phi}{\partial x_j} dV = \sum_{i=1}^{N_p} \oint_V \frac{\partial \Upsilon_{s,i}}{\partial x_j} \delta(\Upsilon_{s,i}) dV = \sum_{i=1}^{N_p} \gamma_i \oint_{S_i} n_{s,j} dS_i \quad (\text{A8})$$

Where  $\delta$  stands for the Dirac delta function.

## A.2 Derivation of the volume-averaged governing equations

In the following, we will perform a “step-by-step” derivation of the coarse-grained governing equations by volume averaging.

### A.2.1 Microscopic equations

We begin by writing down the microscopic equations for mass ( $\rho$ ), momentum ( $\rho u_i$ ), and scalar ( $\theta$ ) balance:

$$\frac{\partial \rho}{\partial t} + \frac{\partial}{\partial x_j} (\rho u_j) = 0 \quad (\text{A9})$$

$$\rho \left[ \frac{\partial u_i}{\partial t} + \frac{\partial}{\partial x_j} (u_i u_j) \right] = - \frac{\partial p}{\partial x_i} + \frac{\partial \tau_{ij}}{\partial x_j} + \rho g_i \quad (\text{A10})$$

$$\frac{\partial \theta}{\partial t} + \frac{\partial}{\partial x_j} (u_j \theta) = \frac{\partial \Phi_j}{\partial x_j} + \Theta \quad (\text{A11})$$

Where  $p$  is the dynamic pressure,  $g_i$  is the gravitational acceleration,  $\tau_{ij}$  is the viscous stress tensor,  $\Phi_j$  is a scalar flux, and  $\Theta$  is a scalar source term. We will also assume a general form for the boundary conditions in the form of  $a_s \psi(s, t) + b_s \partial \psi / \partial n = c_s$  where  $a_s$ ,  $b_s$ , and  $c_s$  are the parameters referring to boundary  $s$  and  $\phi$  can be  $\rho$ ,  $p$ ,  $u_i$ , or  $\theta$ , being  $n$  the normal to the surface. It is easy to show that typically used boundary conditions can be obtained via an appropriate choice of these three parameters.

### A.2.2 Coarse-grained mass balance

1. Multiply by indicator function:

$$\phi \frac{\partial \rho}{\partial t} + \phi \frac{\partial}{\partial x_j} (\rho u_j) = 0 \quad (\text{A12})$$

2. Average over the filtering volume:

$$\oint_V \phi \frac{\partial \rho}{\partial t} dV = - \oint_V \phi \frac{\partial}{\partial x_j} (\rho u_j) dV \quad (\text{A13})$$

3. Use integration by parts:

$$\oint_V \left[ \frac{\partial}{\partial t} (\phi \rho) - \rho \frac{\partial \phi}{\partial t} \right] dV = - \oint_V \left[ \frac{\partial}{\partial x_j} (\phi \rho u) + \rho u_j \frac{\partial \phi}{\partial x_j} \right] dV \quad (\text{A14})$$

4. Use derivative of indicator function and definition of volume surface average for the last RHS term:

$$\oint_V \rho u_j \frac{\partial \phi}{\partial x_j} dV = \sum_{s=0}^{N_p} \gamma_s \oint_{S_s} \rho u_j n_{s,j} dS_s \quad (\text{A15})$$

5. Take derivative out of the integrals:

$$\frac{\partial}{\partial t} (\bar{\phi} \bar{\rho}) - \oint_V \rho \frac{\partial \phi}{\partial t} dV = - \frac{\partial}{\partial x_j} (\bar{\phi} \bar{\rho} \hat{u}_j) + \sum_{s=0}^{N_p} \gamma_s \oint_{S_s} \rho u_j n_{s,j} dS_s \quad (\text{A16})$$

6. Rearranging:

$$\frac{\partial}{\partial t} (\bar{\phi} \bar{\rho}) + \frac{\partial}{\partial x_j} (\bar{\phi} \bar{\rho} \hat{u}_j) = \oint_V \rho \frac{\partial \phi}{\partial t} dV + \sum_{s=0}^{N_p} \gamma_s \oint_{S_s} \rho u_j n_{s,j} dS_s \quad (\text{A17})$$

### A.2.3 Coarse-grained momentum equation

1. Multiply by  $\phi$ :

$$\phi \frac{\partial}{\partial t} (\rho u_i) + \phi \frac{\partial}{\partial x_j} (\rho u_i u_j) = -\phi \frac{\partial p}{\partial x_i} + \phi \frac{\partial \tau_{ij}}{\partial x_j} + \phi \rho g_i \quad (\text{A18})$$

2. Integrate over the filtering volume:

$$\begin{aligned} \oint_V \phi \frac{\partial}{\partial t} (\rho u_i) dV + \oint_V \phi \frac{\partial}{\partial x_j} (\rho u_i u_j) dV &= - \oint_V \phi \frac{\partial p}{\partial x_i} dV \\ &\quad + \oint_V \phi \frac{\partial \tau_{ij}}{\partial x_j} dV + \oint_V \phi \rho g_i dV \end{aligned} \quad (\text{A19})$$

### 3. Time derivative

(a) Use integration by parts:

$$\oint_V \phi \frac{\partial}{\partial t} (\rho u_i) dV = \oint_V \frac{\partial}{\partial t} (\phi \rho u_i) dV - \oint_V \rho u_i \frac{\partial \phi}{\partial t} dV \quad (\text{A20})$$

(b) Exchange integration with derivation:

$$\oint_V \phi \frac{\partial}{\partial t} (\rho u_i) dV = \frac{\partial}{\partial t} (\bar{\phi} \tilde{\rho} \hat{u}_i) - \oint_V \rho u_i \frac{\partial \phi}{\partial t} dV \quad (\text{A21})$$

### 4. Nonlinear term

(a) Integration by parts:

$$\oint_V \phi \frac{\partial}{\partial x_j} (\rho u_i u_j) dV = \oint_V \frac{\partial}{\partial x_j} (\phi \rho u_i u_j) dV - \oint_V (\rho u_i u_j) \frac{\partial \phi}{\partial x_j} dV \quad (\text{A22})$$

(b) Use surface integration:

$$\oint_V \phi \frac{\partial}{\partial x_j} (\rho u_i u_j) dV = \frac{\partial}{\partial x_j} (\bar{\phi} \tilde{\rho} \hat{u}_i \hat{u}_j) - \sum_{s=0}^{N_p} \gamma_s \oint_{S_s} \rho u_i u_j n_{s,j} dS_s \quad (\text{A23})$$

### 5. Pressure term

(a) Integration by parts:

$$-\oint_V \phi \frac{\partial p}{\partial x_i} dV = -\oint_V \frac{\partial}{\partial x_i} (\phi p) dV + \oint_V p \frac{\partial \phi}{\partial x_i} dV \quad (\text{A24})$$

(b) Use phase volume average and derivative of  $\phi$ :

$$-\oint_V \phi \frac{\partial p}{\partial x_i} dV = -\frac{\partial}{\partial x_i} (\bar{\phi} \tilde{p}) + \sum_{s=0}^{N_p} \gamma_s \oint_{S_s} p n_{s,i} dS_s \quad (\text{A25})$$

### 6. Stress tensor

(a) Use integration by parts:

$$\oint_V \phi \frac{\partial \tau_{ij}}{\partial x_j} dV = \oint_V \frac{\partial}{\partial x_j} (\phi \tau_{ij}) dV - \oint_V \tau_{ij} \frac{\partial \phi}{\partial x_j} dV \quad (\text{A26})$$

**(b)** Use phase volume average and derivative of  $\phi$ :

$$\int_V \phi \frac{\partial \tau_{ij}}{\partial x_j} dV = \frac{\partial}{\partial x_j} (\bar{\phi} \tilde{\tau}_{ij}) - \sum_{s=0}^{N_p} \gamma_s \int_{S_s} \tau_{ij} n_{s,j} dS_s \quad (\text{A27})$$

The final volume-averaged momentum equation reads:

$$\begin{aligned} \frac{\partial}{\partial t} (\bar{\phi} \tilde{\rho} \tilde{u}_i) - \int_V \rho u_i \frac{\partial \phi}{\partial t} dV + \frac{\partial}{\partial x_j} (\bar{\phi} \tilde{\rho} \tilde{u}_i \tilde{u}_j - \bar{\phi} \tilde{\tau}_{ij}) = \\ - \frac{\partial}{\partial x_i} (\bar{\phi} \tilde{p}) + \sum_{s=0}^{N_p} \gamma_s \int_{S_s} [p n_{s,i} + (\rho u_i u_j - \tau_{ij}) n_{s,j}] dS_s + \bar{\phi} \tilde{\rho} \tilde{g}_i \end{aligned} \quad (\text{A28})$$

Introducing the usual “a la Leonard” decomposition:

$$\tilde{\rho} \tilde{u}_i \tilde{u}_j = \tilde{\rho} \tilde{u}_i \tilde{u}_j - \tau'_{ij} \quad (\text{A29})$$

And introducing the effective stress tensor:

$$\tau_{ij}^{\text{eff}} = \tilde{\tau}_{ij} + \tau'_{ij} \quad (\text{A30})$$

We obtain the following:

$$\begin{aligned} \frac{\partial}{\partial t} (\bar{\phi} \tilde{\rho} \tilde{u}_i) - \int_V \rho u_i \frac{\partial \phi}{\partial t} dV + \frac{\partial}{\partial x_j} (\bar{\phi} \tilde{\rho} \tilde{u}_i \tilde{u}_j - \bar{\phi} \tau_{ij}^{\text{eff}}) = \\ - \frac{\partial}{\partial x_i} (\bar{\phi} \tilde{p}) + \sum_{s=0}^{N_p} \gamma_s \int_{S_s} [p n_{s,i} + (\rho u_i u_j - \tau_{ij}) n_{s,j}] dS_s + \bar{\phi} \tilde{\rho} \tilde{g}_i \end{aligned} \quad (\text{A31})$$

#### A.2.4 Coarse-grained scalar transport equation

1. Multiply by  $\phi$  and volume average:

$$\int_V \phi \frac{\partial \theta}{\partial t} dV + \int_V \phi \frac{\partial}{\partial x_j} (u_j \theta) dV = \int_V \phi \frac{\partial \Phi_j}{\partial x_j} dV + \int_V \phi \Theta dV \quad (\text{A32})$$

2. Time derivative

**(a)** Use integration by parts:

$$\int_V \phi \frac{\partial \theta}{\partial t} dV = \int_V \frac{\partial}{\partial t} (\phi \theta) dV - \int_V \theta \frac{\partial \phi}{\partial t} dV \quad (\text{A33})$$

**(b)** Use phase volume average:

$$\oint_V \frac{\partial}{\partial t} (\phi\theta) dV - \oint_V \theta \frac{\partial \phi}{\partial t} dV = \frac{\partial}{\partial t} (\bar{\phi}\tilde{\theta}) - \oint_V \theta \frac{\partial \phi}{\partial t} dV \quad (\text{A34})$$

### 3. Advection term

**(a)** Use integration by parts:

$$\oint_V \phi \frac{\partial}{\partial x_j} (u_j \theta) dV = \oint_V \frac{\partial}{\partial x_j} (\phi u_j \theta) dV - \oint_V (u_j \theta) \frac{\partial \phi}{\partial x_j} dV \quad (\text{A35})$$

**(b)** Use phase volume average and derivative of  $\phi$ :

$$\oint_V \frac{\partial}{\partial x_j} (\phi u_j \theta) dV - \oint_V (u_j \theta) \frac{\partial \phi}{\partial x_j} dV = \frac{\partial}{\partial x_j} (\bar{\phi}\tilde{u}_j\theta) - \sum_{s=0}^{N_p} \gamma_s \oint_{S_s} (u_j \theta) n_{s,j} dS_s \quad (\text{A36})$$

Applying the same to the diffusion term and the source term one obtains:

$$\begin{aligned} \frac{\partial}{\partial t} (\bar{\phi}\tilde{\theta}) - \oint_V \theta \frac{\partial \phi}{\partial t} dV + \frac{\partial}{\partial x_j} (\bar{\phi}\tilde{u}_j\theta - \bar{\phi}\tilde{\Phi}_j) = \\ - \sum_{s=0}^{N_p} \gamma_s \oint_{S_s} (u_j \theta + \Phi_j) n_{s,j} dS_s + \bar{\phi}\tilde{\Theta} \end{aligned} \quad (\text{A37})$$

## A.2.5 List of coarse-grained transport equations

Mass balance:

$$\frac{\partial}{\partial t} (\bar{\phi}\tilde{\rho}) + \frac{\partial}{\partial x_j} (\bar{\phi}\tilde{\rho}\widehat{u}_j) = \oint_V \rho \frac{\partial \phi}{\partial t} dV + \sum_{s=0}^{N_p} \gamma_s \oint_{S_s} \rho u_j n_{s,j} dS_s \quad (\text{A38})$$

Momentum conservation:

$$\begin{aligned} \frac{\partial}{\partial t} (\bar{\phi}\tilde{\rho}\widehat{u}_i) - \oint_V \rho u_i \frac{\partial \phi}{\partial t} dV + \frac{\partial}{\partial x_j} (\bar{\phi}\tilde{\rho}\widehat{u}_i\widehat{u}_j - \bar{\phi}\tilde{\tau}_{ij}) = \\ - \frac{\partial}{\partial x_i} (\bar{\phi}\tilde{\rho}) + \sum_{s=0}^{N_p} \gamma_s \oint_{S_s} [p n_{s,i} + (\rho u_i u_j - \tau_{ij}) n_{s,j}] dS_s + \bar{\phi}\tilde{\rho}\widehat{g}_i \end{aligned} \quad (\text{A39})$$

*Scalar transport:*

$$\frac{\partial}{\partial t} (\bar{\phi}\tilde{\theta}) - \int_V \theta \frac{\partial \phi}{\partial t} dV + \frac{\partial}{\partial x_j} (\bar{\phi}u_j\tilde{\theta} - \bar{\phi}\tilde{\Phi}_j) = - \sum_{s=0}^{N_p} \gamma_s \int_{S_s} (u_j\theta + \Phi_j) n_{s,j} dS_s + \bar{\phi}\tilde{\Theta} \quad (\text{A40})$$

### A.3 Approximations of the volume-averaged governing equations

In the following, we will present some standard approximations to the equations derived (in Section A.2) that allow to significantly simplify their solution process and to disregard some terms that would otherwise require modelling.

#### A.3.1 No slip condition at particle surfaces

The use of a “no-slip” condition at particle surface results in the fluid velocity field  $u_i$  to be equal to the particle velocity  $v_i$  at any boundary point. Since  $v_i$  is known from the Newton’s equations, this condition simplifies all the surface integrals.

#### A.3.2 Low Mach number (incompressibility limit)

In this regime, the fluid density  $\rho$  may be regarded as a constant  $\rho_0$ . One important implication is that mass averaged and fluid volume-averaged quantities become identical and there is no distinction between  $\hat{u}_i$  and  $\tilde{u}_i$ .

#### A.3.3 Nondeformable particles

If we consider particles with fixed shape (i.e., not growing or shrinking and unbreakable), then we can simplify the equations by noticing that:

$$\oint_{S_s} \rho_0 v_j n_{s,j} dS_s = 0, \quad \oint_{S_s} \rho_0 v_i v_j n_{s,j} dS_s = 0 \quad (\text{A41})$$

Which is true if  $S_s$  is a closed surface, i.e., if the particle is completely inside  $V$ . However, even in case the particle is only partially within  $V$ , the previous assumptions ensure that the integrals appear in closed form.

#### A.3.4 High Stokes number: “gas–particle system”

Integrals containing the time derivative of the indicator function can be shown to vanish in the limit of infinite Stokes number  $Stk = \tau_p/\tau_f$ , where  $\tau_p$  is the characteristic time of the dispersed phase and  $\tau_f$  is the characteristic time of the fluid phase. Since the terms  $(\partial\phi)/(\partial t)$  are given by the solution

of Newton's equations for the dispersed phase, they are expected to behave like  $1/\tau_p$ . However, time derivatives of the fluid velocity are behaving like  $U_0/\tau_f = U_0^2/d_p$ , being  $U_0$  a reference velocity and  $d_p$  a characteristic particle diameter. Regardless the specific expression for the Stokes number, in case the particle motion is mainly governed by viscous forces  $Stk$  is proportional to the ratio between the particle and fluid density  $\rho_p/\rho_0$ . Therefore, terms involving time derivatives of the indicator function are negligible in most of the case where gas–solid suspensions are studied.

### A.3.5 Simplified equations

We can therefore write a simplified form of the governing equations which employ the aforementioned assumptions:

*Mass balance:*

$$\frac{\partial}{\partial t}(\bar{\phi}) + \frac{\partial}{\partial x_j}(\bar{\phi}\tilde{u}_j) = 0 \quad (\text{A42})$$

*Momentum conservation:*

$$\begin{aligned} \frac{\partial}{\partial t}(\bar{\phi}\tilde{u}_i) + \frac{\partial}{\partial x_j} \left( \bar{\phi}\tilde{u}_i\tilde{u}_j - \frac{1}{\rho_0}\bar{\phi}\tilde{\tau}_{ij} \right) = \\ -\frac{1}{\rho_0}\frac{\partial}{\partial x_i}(\bar{\phi}\tilde{p}) - \sum_{s=0}^{N_p} \gamma_s \oint_{S_s} [\tau_{ij}n_{s,j} - pn_{s,i}] dS_s - \bar{\phi}\mathbf{g}_i \end{aligned} \quad (\text{A43})$$

*Scalar transport:*

$$\frac{\partial}{\partial t}(\bar{\phi}\tilde{\theta}) + \frac{\partial}{\partial x_j}(\bar{\phi}\tilde{u}_j\tilde{\theta} - \bar{\phi}\tilde{\Phi}_j) = -\sum_{s=0}^{N_p} \gamma_s \oint_{S_s} (u_j\theta + \Phi_j) n_{s,j} dS_s + \bar{\phi}\tilde{\Theta} \quad (\text{A44})$$

## REFERENCES

- Abadi M, et al: Tensorflow: Large-scale machine learning on heterogeneous distributed systems: <http://download.tensorflow.org/paper/whitepaper2015.pdf>, 2015.
- Agrawal K, et al: The role of meso-scale structures in rapid gas–solid flows, *J Fluid Mech* 445:151–185, 2001.
- Agrawal K, et al: Filtered models for scalar transport in gas–particle flows, *Chem Eng Sci* 95:291–300, 2013.
- Akiki G, Jackson TL, Balachandar S: Pairwise interaction extended point-particle model for a random array of monodisperse spheres, *J Fluid Mech* 813:882–928, 2017.
- Amini H, Lee W, Di Carlo D: Inertial microfluidic physics, *Lab Chip* 14:2739–2761, 2014.

- Anderson TB, Jackson R: A fluid mechanical description of fluidized beds, *Ind Eng Chem Fundam* 6(4):527–539, 1967.
- Askarishahi M, Salehi M, Radl S: Full-physics simulations of spray-particle interaction in a bubbling fluidized bed, *AIChE J* 63:2569–2587, 2017.
- Baker M, et al: In *RANS modeling of cluster-induced and shear turbulence in particle-laden channel flow*, AIChE annual meet 2016. San Francisco, AIChE, 2016.
- Beck D, et al: Data science: accelerating innovation and discovery in chemical engineering, *AIChE J* 62(5):1402–1416, 2016.
- Beetstra R, van der Hoef MA, Kuipers JAM: Drag force of intermediate Reynolds number flow past mono- and bidisperse arrays of spheres, *AIChE J* 53(2):489–501, 2007.
- Berthold M, et al: KNIME: the Konstanz information miner, *ACM SIGKDD Explor Newsl* 11(1):26–31, 2008.
- Bierwisch C, et al: Three-dimensional discrete element models for the granular statics and dynamics of powders in cavity filling, *J Mech Phys Solids* 57(1):10–31, 2009.
- Boyce CM, et al: Growth and breakup of a wet agglomerate in a dry gas-solid fluidized bed, *AIChE J* 63:2520–2527, 2017.
- Brady JF, Bossis G: Stokesian dynamics, *Annu Rev Fluid Mech* 20(1):111–157, 1988.
- Buist KA, et al: A combined experimental and simulation study of fluid–particle heat transfer in dense arrays of stationary particles, *Chem Eng Sci* 169:310–320, 2017.
- Calzavarini E, et al: Quantifying turbulence induced segregation of inertial particles, *Phys Rev Lett* 101(2):84504, 2008.
- Capecelatro J, Desjardins O: An Euler–Lagrange strategy for simulating particle-laden flows, *J Comput Phys* 238:1–31, 2013.
- Capecelatro J, Desjardins O, Fox RO: Numerical study of collisional particle dynamics in cluster-induced turbulence, *J Fluid Mech* 747:R2, 2014.
- Capecelatro J, Desjardins O, Fox RO: On fluid–particle dynamics in fully developed cluster-induced turbulence, *J Fluid Mech* 780:578–635, 2015.
- Capecelatro J, Desjardins O, Fox RO: Strongly coupled fluid-particle flows in vertical channels. II. Turbulence modeling, *Phys Fluids* 28(3):33307, 2016.
- Cloete S, Amini S, Johansen ST: On the effect of cluster resolution in riser flows on momentum and reaction kinetic interaction, *Powder Technol* 210:6–17, 2011.
- Cloete S, Johansen ST, Amini S: Performance evaluation of a complete Lagrangian KTGF approach for dilute granular flow modelling, *Powder Technol* 226:43–52, 2012.
- Cloete JH, et al: Evaluation of wall friction models for riser flow, *Powder Technol* 303:156–167, 2016.
- Cloete J.H., et al: An anisotropic mesoscale solids stress closure for freely sedimenting gas-particle suspensions, *Powder Technol* 2017a, under revi.
- Cloete JH, et al: The sensitivity of filtered two fluid model to the underlying resolved simulation setup, *Powder Technol* 316:265–277, 2017a.
- Cloete JH, et al: In Olsen JEO, Johansen ST, editors: *Verification of filtered two fluid models for reactive gas-solid flows*, 12th international conference on CFD oil gas, metall process industries. Trondheim, Norway, SINTEF, Norway, 2017b.
- Cundall PA, Strack ODL: A discrete numerical model for granular assemblies, *Géotechnique* 47–65, 1979.
- de Baas AF, Rosso L: *Modelling in FP7 NMP programme materials projects*, Brussels, Belgium, 2015, Brussels, Belgium, European Commission, Directorate-General for Research and Innovation.
- de Klerk A: Voidage variation in packed beds at small column to particle diameter ratio, *AIChE J* 49(8):2022–2029, 2003.
- Deen NG, Kuipers JAM: Direct numerical simulation (DNS) of mass, momentum and heat transfer in dense fluid-particle systems, *Curr Opin Chem Eng* 5:84–89, 2014a.
- Deen NG, Kuipers JAM: Direct numerical simulation of fluid flow accompanied by coupled mass and heat transfer in dense fluid–particle systems, *Chem Eng Sci* 116:645–656, 2014b.

- Deen NG, et al: Direct numerical simulation of flow and heat transfer in dense fluid-particle systems, *Chem Eng Sci* 81:329–344, 2012.
- Deen NG, et al: Review of direct numerical simulation of fluid-particle mass, momentum and heat transfer in dense gas-solid flows, *Chem Eng Sci* 116:710–724, 2014.
- Delgado JMPQ: A critical review of dispersion in packed beds, *Heat Mass Transf* 42:279–310, 2006.
- Derkse J: Mixing by solid particles, *Chem Eng Res Des* 86(12):1363–1368, 2008a.
- Derkse JJ: Scalar mixing by granular particles, *AICHE J* 54(7):1741–1747, 2008b.
- Derkse JJ: Scalar mixing with fixed and fluidized particles in micro-reactors, *Chem Eng Res Des* 87(4):550–556, 2009.
- Derkse JJ: Simulations of scalar dispersion in fluidized solid–liquid suspensions, *AICHE J* 60(5):1880–1890, 2014a.
- Derkse JJ: Simulations of solid–liquid mass transfer in fixed and fluidized beds, *Chem Eng J* 255:233–244, 2014b.
- Derkse JJ, Sundaresan S: Direct numerical simulations of dense suspensions: wave instabilities in liquid–fluidized beds, *J Fluid Mech* 587:303–336, 2007.
- Desjardins O, Fox RO, Villedieu P: A quadrature-based moment method for dilute fluid-particle flows, *J Comput Phys* 227(4):2514–2539, 2008.
- Di Carlo D: Inertial microfluidics, *Lab Chip* 9(21):3038–3046, 2009.
- Di Carlo D, et al: Particle segregation and dynamics in confined flows, *Phys Rev Lett* 102(9):94503, 2009.
- Ding J, Gidaspow D: A bubbling fluidization model using kinetic-theory of granular flow, *AICHE J* 36(4):523–538, 1990.
- Dixon AG: Local transport and reaction rates in a fixed bed reactor tube: endothermic steam methane reforming, *Chem Eng Sci* 168:156–177, 2017.
- Domingo P, Vervisch L: DNS and approximate deconvolution as a tool to analyse one-dimensional filtered flame sub-grid scale modelling, *Combust Flame* 177:109–122, 2017.
- Egholm DL: A new strategy for discrete element numerical models: 1. Theory, *J Geophys Res Earth* 112(B5), 2007.
- Egholm DL, et al: A new strategy for discrete element numerical models: 2. Sandbox applications, *J Geophys Res Earth* 112(B5), 2007.
- Eswaran V, Pope SB: An examination of forcing in direct numerical simulations of turbulence, *Comput Fluids* 257:257–278, 1988.
- Fan FG, Ahmadi G: A sublayer model for wall deposition of ellipsoidal particles in turbulent streams, *J Aerosol Sci* 26(5):813–840, 1995.
- Feng ZG, Michaelides EE: Heat transfer in particulate flows with direct numerical simulation (DNS), *Int J Heat Mass Transf* 52(3–4):777–786, 2009.
- Feng Z-G, Musong SG: Direct numerical simulation of heat and mass transfer of spheres in a fluidized bed, *Powder Technol* 262:62–70, 2014.
- Forgber T, Radl S: A novel approach to calculate radiative thermal exchange in coupled particle simulations, *Powder Technol* 323:24–44, 2018.
- Forgber T, et al: Heat transfer rates in sheared beds of inertial particles at high Biot numbers, *Granul Matter* 19(14), 2017.
- Fotovat F, Bi XT, Grace JR: Electrostatics in gas–solid fluidized beds: a review, *Chem Eng Sci* 173:303–334, 2017.
- Fox RO: A quadrature-based third-order moment method for dilute gas-particle flows, *J Comput Phys* 227(12):6313–6350, 2008.
- Fox RO: Large-Eddy-simulation tools for multiphase flows, *Annu Rev Fluid Mech* 44:47–76, 2012.
- Fox RO: In *Quadrature-based moment methods for fluid-particle flows*, Part Technol Forum (Shell Thomas Baron Award Fluid-Particle System), 2017, pp 28–40.
- Fox RO, et al: In *Clustering in gas-solid flows: how are clusters modified by shear?* AIChE annual meet 2016. San Francisco, AIChE, 2016.

- Fullmer WD, Hrenya CM: Quantitative assessment of fine-grid kinetic-theory-based predictions of mean-slip in unbounded fluidization, *AIChE J* 62:11–17, 2016.
- Fullmer WD, Hrenya CM: The clustering instability in rapid granular and gas-solid flows, *Annu Rev Fluid Mech* 49:485–510, 2017.
- Galvin JE, Benyahia S: The effect of cohesive forces on the fluidization of aeratable powders, *AIChE J* 60(2):473–484, 2014.
- Ganguli S, Lele S: In *Drag of spherical particles in a periodic lattice: heat transfer, buoyancy and non-boussinesq effect*, APS DFD meet 2016. Portland, Oregon, American Physical Society, 2016.
- Gidaspow D: *Multiphase flow and fluidization: continuum and kinetic theory descriptions*, San Diego, California, U.S.A, 1994, Academic Press.
- Girardi M, Radl S, Sundaresan S: In *Liquid distribution in wet fluidized beds*, AIChE annual meet 2012. Pittsburgh, PA, United States, AIChE, 2012.
- Girardi M, Radl S, Sundaresan S: Simulating wet gas-solid fluidized beds using coarse-grid CFD-DEM, *Chem Eng Sci* 144:224–238, 2016.
- Glasser BJ, Sundaresan S, Kevrekidis I: From bubbles to clusters in fluidized beds, *Phys Rev Lett* 81(9):1849–1852, 1998.
- Goniva C, et al: Influence of rolling friction on single spout fluidized bed simulation, *Particuology* 10(5):582–591, 2012.
- Greiderer Z, et al: In *Agglomerate size distribution in wet gas fluidized systems*, AIChE annual meet 2014. Atlanta, U.S., AIChE, 2014.
- Gu Y, Ozel A, Sundaresan S: A modified cohesion model for CFD-DEM simulations of fluidization, *Powder Technol* 296:17–28, 2016a.
- Gu Y, Ozel A, Sundaresan S: Numerical studies of the effects of fines on fluidization, *AIChE J* 62(7):2271–2281, 2016b.
- Gunn DJ: Transfer of heat or mass to particles in fixed and fluidised beds, *Int J Heat Mass Transf* 21:467–476, 1978.
- Hærvig J, et al: On the adhesive JKR contact and rolling models for reduced particle stiffness discrete element simulations, *Powder Technol* 319:472–482, 2017.
- Hagelien T, et al: In Kilappa V, Matilla K, editors: *Porto: a framework for information interchange and multi-scale fluid mechanics simulations*, 3rd work European multi-scale model cluster. Jyväskylä, Finland, University of Jyväskylä, Finland, 2015, pp 1–33.
- Holloway WS: *Continuum modeling of gas-particle flows across multiple scales*, PhD Thesis, 2012, Princeton University.
- Holloway WS, Sundaresan S: In *Filtered models for reacting gas-solid flows*, AIChE annual meet 2011. AIChE, 2011.
- Holloway WS, Sundaresan S: Filtered models for reacting gas-particle flows, *Chem Eng Sci* 82:132–143, 2012.
- Holloway WS, Sundaresan S: Filtered models for bidisperse gas-particle flows, *Chem Eng Sci* 108:67–86, 2014.
- Holloway WS, Yin X, Sundaresan S: Fluid-particle drag in inertial polydisperse gas-solid suspensions, *AIChE J* 56(8):1995–2004, 2010.
- Holloway WS, et al: Meso-scale structures of bidisperse mixtures of particles fluidized by a gas, *Chem Eng Sci* 66(19):4403–4420, 2011.
- Holloway WS, Sun J, Sundaresan S: Effect of microstructural anisotropy on the fluid-particle drag force and the stability of the uniformly fluidized state, *J Fluid Mech* 713:27–49, 2012.
- Hölzer A, Sommerfeld M: Lattice Boltzmann simulations to determine drag, lift and torque acting on non-spherical particles, *Comput Fluids* 38(3):572–589, 2009.
- Horwitz J, et al: In *A direct comparison of fully resolved and point-particle models in particle-laden turbulent flow*, APS DFD meet 2016. Portland, Oregon, American Physical Society, 2016.
- Iddir H, Arastoopour H: Modeling of multitype particle flow using the kinetic theory approach, *AIChE J* 51(6):1620–1632, 2005.
- İgci Y, Sundaresan S: Constitutive models for filtered two-fluid models of fluidized gas-particle flows, *Ind Eng Chem Res* 50:13190–13201, 2011.

- Igci Y, et al: Filtered two-fluid models for fluidized gas-particle suspensions, *AIChE J* 54(6):1431–1448, 2008.
- Jackson R: *The dynamics of fluidized particles*, Cambridge, UK, 2000, Cambridge University Press (Cambridge Monographs on Mechanics).
- Jajcevic D, et al: Large-scale CFD-DEM simulations of fluidized granular systems, *Chem Eng Sci* 98:298–310, 2013.
- Johnson PC, Jackson R: Frictional-collisional constitutive relations for granular materials, with application to plane shearing, *J Fluid Mech* 176:67–93, 1987.
- Kloss C, et al: Models, algorithms and validation for opensource DEM and CFD-DEM, *Prog Comput Fluid Dyn* 12:140–152, 2012.
- Kolakaluri R: *Direct numerical simulations and analytical modeling of granular filtration*, 2013, PhD Thesis, Iowa State University.
- Kolakaluri R, et al: Filtration model for polydisperse aerosols in gas-solid flow using granule-resolved direct numerical simulation, *AIChE J* 61(11):3594–3606, 2015.
- Kolehmainen J, et al: A hybrid approach to computing electrostatic forces in fluidized beds of charged particles, *AIChE J* 62(7):2282–2295, 2016.
- Kolehmainen J, Sippola P, et al: Effect of humidity on triboelectric charging in a vertically vibrated granular bed: experiments and modeling, *Chem Eng Sci* 173:363–373, 2017a.
- Kolehmainen J, Ozel A, et al: Triboelectric charging of monodisperse particles in fluidized beds, *AIChE J* 63(6):1872–1891, 2017b.
- Kolehmainen J, Ozel A, Sundaresan S: In *Gas-solid flows with tribocharging*, AIChE annual meet 2017. Minneapolis, USA, AIChE, 2017c.
- Kong B, Fox RO: A solution algorithm for fluid-particle flows across all flow regimes, *J Comput Phys* 344:575–594, 2017.
- Kong B, et al: Euler-Euler anisotropic Gaussian mesoscale simulation of homogeneous cluster-induced gas-particle turbulence, *AIChE J* 63:2630–2643, 2017.
- Kravets B, Kruggel-Emden H: Investigation of local heat transfer in random particle packings by a fully resolved LBM-approach, *Powder Technol* 318:293–305, 2017.
- Kriebitzsch SHL, van der Hoef MA, Kuipers JAM: Drag force in discrete particle models—continuum scale or single particle scale? *AIChE J* 59(1):316–324, 2013.
- Kuerten JGM: Subgrid modeling in particle-laden channel flow, *Phys Fluids* 18(2):25108, 2006.
- Ladd AJC: Numerical simulations of particulate suspensions via a discretized Boltzmann equation. Part 1. Theoretical foundation, *J Fluid Mech* 271:285–309, 1994.
- Lane WA, et al: Sub-grid models for heat transfer in gas-particle flows with immersed horizontal cylinders, *Chem Eng Sci* 151:7–15, 2016.
- Lees AW, Edwards SF: The computer study of transport processes under extreme conditions, *J Phys Chem* 5:1921–1930, 1972.
- Lekhal A, Glasser BJ, Khinast JG: Impact of drying on the catalyst profile in supported impregnation catalysts, *Chem Eng Sci* 56(15):4473–4487, 2001a.
- Lekhal A, Khinast JG, Glasser BJ: Predicting the effect of drying on supported coimpregnation catalysts, *Ind Eng Chem Res* 40(18):3989–3999, 2001b.
- Lu G, Third JR, Müller CR: Discrete element models for non-spherical particle systems: from theoretical developments to applications, *Chem Eng Sci* 127:425–465, 2015.
- Ma T, et al: Kernel-assisted and topology-aware MPI collective communications on multicore/many-core platforms, *J Parallel Distrib Comput* 73(7):1000–1010, 2013.
- Maheshwari A, Chhabra RP, Biswas G: Effect of blockage on drag and heat transfer from a single sphere and an in-line array of three spheres, *Powder Technol* 168(2):74–83, 2006.
- Mahmoudi AH, et al: Modeling of the biomass combustion on a forward acting grate using XDEM, *Chem Eng Sci* 142:32–41, 2016.
- Mamidala AR, et al: In *MPI collectives on modern multicore clusters: performance optimizations and communication characteristics*, Proceedings of CCGRID 2008—8th IEEE international symposium on cluster computing grid, 2008, pp 130–137.

- Marchioli C: Large-eddy simulation of turbulent dispersed flows: a review of modelling approaches, *Acta Mech* 228(3):741–771, 2017.
- Marchisio DL, Fox RO: *Computational models for polydisperse particulate and multiphase systems*, Cambridge, UK, 2013, Cambridge University Press.
- Milioli CC, et al: Filtered two-fluid models of fluidized gas-particle flows: new constitutive relations, *AIChE J* 59:3265–3275, 2013.
- Moureau V, Domingo P, Vervisch L: From large-eddy simulation to direct numerical simulation of a lean premixed swirl flame: filtered laminar flame-PDF modeling, *Combust Flame* 158(7):1340–1357, 2011.
- Mueller GE: Radial void fraction distributions in randomly packed fixed beds of uniformly sized spheres in cylindrical containers, *Powder Technol* 72:269–275, 1992.
- Municchi F, Radl S: Consistent closures for Euler-Lagrange models of bi-disperse gas-particle suspensions derived from particle-resolved direct numerical simulations, *Int J Heat Mass Transf* 111:171–190, 2017.
- Municchi F, Radl S: Momentum, heat and mass transfer simulations of bounded dense mono-dispersed gas-particle systems, *Int J Heat Mass Transf* 120:1146–1161, 2018.
- Municchi F, Goniva C, Radl S: Highly efficient spatial data filtering in parallel using the opensource library CPPPO, *Comput Phys Commun* 207:400–414, 2016.
- NanoSim—a multiscale simulation-based design platform for cost-effective CO<sub>2</sub> capture processes using nano-structured materials: <https://www.sintef.no/projectweb/nanosim/>, 2017.
- Nakariyakul S: Fast spatial averaging: an efficient algorithm for 2D mean filtering, *J Supercomput* 65(1):262–273, 2013.
- Oschmann T, Schiemann M, Krugel-Emden H: Development and verification of a resolved 3D inner particle heat transfer model for the discrete element method (DEM), *Powder Technol* 291:392–407, 2016.
- Ouchene R, et al: In *Numerical simulation and modelling of the forces acting on single and multiple non-spherical particles*, Proceeding ASME 2014 4th Jt US-European Fluids Eng. Chicago, Illinois, USA, ASME, 2014.
- Ouchene R, et al: Drag, lift and torque coefficients for ellipsoidal particles: from low to moderate particle Reynolds numbers, *Comput Fluids* 113:53–64, 2015.
- Ouchene R, et al: A new set of correlations of drag, lift and torque coefficients for non-spherical particles and large Reynolds numbers, *Powder Technol* 303:33–43, 2016.
- Ozel A, Fede P, Simonin O: Development of filtered Euler–Euler two-phase model for circulating fluidised bed: high resolution simulation, formulation and a priori analyses, *Int J Multiphase Flow* 55:43–63, 2013.
- Ozel A, et al: Fluid and particle coarsening of drag force for discrete-parcel approach, *Chem Eng Sci* 155:258–267, 2016.
- Ozel A, et al: Towards filtered drag force model for non-cohesive and cohesive particle-gas flows, *Phys Fluids* 29, 2017, 103308.
- Padding JT: In Padding JT, editor: *Lecture notes for the course on particle-based simulations*, Delft, 2013, Delft University of Technology.
- Pannala S, Syamlal M, O'Brien TJ, O'Brien TJ, Hershey PA: In Pannala S, Syamlal M, editors: *Computational gas-solids flows and reacting systems: theory, methods and practice*, United States, 2011, Engineering Science Reference.
- Parmentier J-F, Simonin O, Delsart O: A functional subgrid drift velocity model for filtered drag prediction in dense fluidized bed, *AIChE J* 58:1084–1098, 2011.
- Passalacqua A, Fox RO: Advanced continuum modelling of gas-particle flows beyond the hydrodynamic limit, *App Math Model* 35(4):1616–1627, 2011.
- Patankar NA, Joseph DD: Modeling and numerical simulation of particulate flows by the Eulerian-Lagrangian approach, *Int J Multiphase Flow* 27(10):1659–1684, 2001.
- Pirker S, Kahrimanovic D, Aichinger G: Modeling mass loading effects in industrial cyclones by a combined Eulerian-Lagrangian approach, *Acta Mech* 204(3–4):203–216, 2009.

- Pirker S, et al: Application of a hybrid lattice Boltzmann-finite volume turbulence model to cyclone short-cut flow, *Powder Technol* 235:572–580, 2013.
- Podlozhnyuk A, et al: In *Modelling superquadric particles using hybrid fictitious domain-immersed boundary method*, 11th OpenFOAM® Work. Guimaraes, Portugal, University of Minho, Institute of Polymers and Composites, Portugal, 2016.
- Popoff B, Braun M: In *A Lagrangian approach to dense particulate flows*, 6th international conference on multiphase flow, 2007, p 510.
- Radeke C, Glasser BJ, Khinast JG: Large-scale powder mixer simulations using massively parallel GPU architectures, *Chem Eng Sci* 65(24):6435–6442, 2010.
- Radl S, Sundaresan S: A drag model for filtered Euler-Lagrange simulations of clustered gas-particle suspensions, *Chem Eng Sci* 117:416–425, 2014.
- Radl S, et al: In *Parcel-based approach for the simulation of gas-particle flows*, 8th International conference CFD oil gas, metal process industries. Trondheim, Norway, SINTEF/NTNU Trondheim, Norway124, 2011, pp 1–10.
- Radl S, Girardi M, Sundaresan S: In Eberhardsteiner J, editor: *Effective drag law for parcel-based approaches—what can we learn from CFD-DEM?* ECCOMAS 2012—European congress computational methods in applied sciences engineering. Vienna, Austria, 2012, pp 1225–1239.
- Radl S, Krainer F, et al: In *Biot number effects on the local heat and mass transfer rate in fixed and fluidized beds*, AIChE annual meet 2015. Salt Lake City, U.S.A., AIChE, 2015a.
- Radl S, Forgber T, et al: In Onate E, et al, editor: *ParScale—an open-source library for the simulation of intra-particle heat and mass transport processes in coupled simulations*, IV International conference part methods—fundamental application (PARTICLES 2015). Barcelona, Spain, ECCOMAS1–9, 2015b.
- Rantanen J, Khinast J: The future of pharmaceutical manufacturing sciences, *J Pharm Sci* 104(11):3612–3638, 2015.
- Rhodes M, et al: Onset of cohesive behaviour in gas fluidized beds: a numerical study using DEM simulation, *Chem Eng Sci* 56(14):4433–4438, 2001.
- Roadmap chemical reaction engineering: [http://dechema.de/dechema\\_media/Reaktionstechnik\\_Roadmap\\_2017\\_en-p-20002685.pdf](http://dechema.de/dechema_media/Reaktionstechnik_Roadmap_2017_en-p-20002685.pdf), 2017.
- Rohde M, Derkens JJ, Van Den Akker HEA: Volumetric method for calculating the flow around moving objects in lattice-Boltzmann schemes, *Phys Rev E* 65(5):56701, 2002.
- Rourke PJO, Snider DM: A new blended acceleration model for the particle contact forces induced by an interstitial fluid in dense particle/fluid flows, *Powder Technol* 256:39–51, 2014.
- Rubinstein GJ, Derkens JJ, Sundaresan S: Lattice Boltzmann simulations of low-Reynolds-number flow past fluidized spheres: effect of Stokes number on drag force, *J Fluid Mech* 788:576–601, 2016.
- Sagaut P: *Large Eddy simulation for incompressible flows—an introduction*, ed 3, Berlin, Germany, 2006, Springer, Berlin.
- Sakai M, Koshizuka S: Large-scale discrete element modeling in pneumatic conveying, *Chem Eng Sci* 64(3):533–539, 2009.
- Sarkar A, et al: Filtered sub-grid constitutive models for fluidized gas-particle flows constructed from 3-D simulations, *Chem Eng Sci* 152:443–456, 2016.
- Schellander D, Schneiderbauer S, Pirker S: Numerical study of dilute and dense polydispersed gas-solid two-phase flows using an Eulerian and Lagrangian hybrid model, *Chem Eng Sci* 95:107–118, 2013.
- Schmidt R, Nikrityuk PA: Numerical simulation of the transient temperature distribution inside moving particles, *Can J Chem Eng* 90(2):246–262, 2012.
- Schneiderbauer S: A spatially-averaged two-fluid model for dense large-scale gas-solid flows, *AIChE J* 63(8):3544–3562, 2017.
- Schneiderbauer S, Pirker S: Filtered and heterogeneity-based subgrid modifications for gas-solid drag and solid stresses in bubbling fluidized beds, *AIChE J* 60(3):839–854, 2014.

- Schneiderbauer S, Saeedipour M: Approximate deconvolution model for the simulation of turbulent gas-solid flows: an a-priori analysis, *Phys Fluids* 30:23301, 2018.
- Schneiderbauer S, et al: Non-steady state boundary conditions for collisional granular flows at flat frictional moving walls, *Int J Multiphase Flow* 43:149–156, 2012a.
- Schneiderbauer S, Aigner A, Pirker S: A comprehensive frictional-kinetic model for gas-particle flows: analysis of fluidized and moving bed regimes, *Chem Eng Sci* 80:279–292, 2012b.
- Schneiderbauer S, et al: A Lagrangian-Eulerian hybrid model for the simulation of industrial-scale gas-solid cyclones, *Powder Technol* 304:229–240, 2016.
- Shinbrot T, Rutala M, Herrmann H: Surface contact charging, *Phys Rev E* 96(3):32912, 2017.
- Sierou A, Brady JF: Accelerated Stokesian dynamics simulations, *J Fluid Mech* 448:115–146, 2001.
- Singhal A, et al: Heat transfer to a gas from densely packed beds of monodisperse spherical particles, *Chem Eng J* 314:27–37, 2017.
- Snider DM: An incompressible three-dimensional multiphase particle-in-cell model for dense particle flows, *J Comput Phys* 170(2):523–549, 2001.
- Sommerfeld M: Analysis of collision effects for turbulent gas-particle flow in a horizontal channel: part 1. Particle transport, *Int J Multiphase Flow* 29(4):675–699, 2003.
- Stan CA, et al: The magnitude of lift forces acting on drops and bubbles in liquids flowing inside microchannels, *Lab Chip* 13(3):365–376, 2013.
- Stark AK, et al: Towards an advanced reactor network modeling framework for fluidized bed biomass gasification: incorporating information from detailed CFD simulations, *Chem Eng J* 303:409–424, 2016.
- Sun B, Tenneti S, Subramaniam S: Modeling average gas-solid heat transfer using particle-resolved direct numerical simulation, *Int J Heat Mass Transf* 86:898–913, 2015.
- Sundaresan S: Modeling the hydrodynamics of multiphase flow reactors: current status and challenges, *AIChE J* 46(6):1102–1105, 2000.
- Sundaresan S: Instabilities in fluidized beds, *Annu Rev Fluid Mech* 35(1):63–88, 2003.
- Sundaresan S, et al: Coarse-grained models for momentum, energy and species transport in gas-particle flows. In *Proceedings of the 14th international conference on fluidization—from fundamentals to products, 2013, Noordwijkerhout, The Netherlands, 2013*, Engineering Conferences International.
- Tang Y, Peters EAJF, Kuipers JAM: Direct numerical simulations of dynamic gas-solid suspensions, *AIChE J* 62(6):1958–1969, 2016.
- Tavassoli H, et al: Direct numerical simulation of particulate flow with heat transfer, *Int J Multiphase Flow* 57:29–37, 2013.
- Tavassoli H, Peters EAJF, Kuipers JAM: Direct numerical simulation of fluid-particle heat transfer in fixed random arrays of non-spherical particles, *Chem Eng Sci* 129:42–48, 2015.
- Ten Cate A, et al: Fully resolved simulations of colliding monodisperse spheres in forced isotropic turbulence, *J Fluid Mech* 519:233–271, 2004.
- Tenneti S, Subramaniam S: Particle-resolved direct numerical simulation for gas-solid flow model development, *Annu Rev Fluid Mech* 46(1):199–230, 2014.
- Tenneti S, et al: Role of fluid heating in dense gas-solid flow as revealed by particle-resolved direct numerical simulation, *Int J Heat Mass Transf* 58:471–479, 2013.
- Theuerkauf J, Witt P, Schwesig D: Analysis of particle porosity distribution in fixed beds using the discrete element method, *Powder Technol* 165:92–99, 2006.
- Tsai CM, Yeh ZM: Fast spatial averaging filter, international symposium on computer, consumer and control, 1:153–156, 2012.
- Uhlmann M, Doychev T: Sedimentation of a dilute suspension of rigid spheres at intermediate Galileo numbers: the effect of clustering upon the particle motion, *J Fluid Mech* 752:310–348, 2014.

- van Antwerpen W, Toit CG, Rousseau PG: A review of correlations to model the packing structure and effective thermal conductivity in packed beds of mono-sized spherical particles, *Nud Eng Des* 240(7):1803–1818, 2010.
- van der Hoef MA, Beetstra R, Kuipers JAM: Lattice-Boltzmann simulations of low-Reynolds-number flow past mono- and bidisperse arrays of spheres: results for the permeability and drag force, *J Fluid Mech* 528:233–254, 2005.
- van der Hoef MA, et al: Numerical simulation of dense gas-solid fluidized beds: a multiscale modeling strategy, *Annu Rev Fluid Mech* 40(1):47–70, 2008.
- Wen C, Yu Y: Mechanics of fluidization, *Chem Eng Prog Symp Ser* 62:100–111, 1966.
- Whitaker S: *The method of volume averaging*, Dordrecht, NL, 1999, Springer Science + Business Media.
- Wu M, Khinast JG, Radl S: In *Direct simulation of film flow on spheres to investigate liquid bridge*, AIChE annual meet 2014. Atlanta, Vereinigte Staaten (USA), AIChE, 2014.
- Wu M, Khinast JG, Radl S: A model to predict liquid bridge formation between wet particles based on direct numerical simulations, *AIChE J* 62(6):1877–1897, 2016.
- Wu M, Khinast JG, Radl S: Liquid transport rates during binary collisions of unequally-sized particles, *Powder Technol* 309:95–109, 2017.
- Wu M, Khinast JG, Radl S: The effect of liquid bridge model details on the dynamics of wet fluidized beds, *AIChE J* 64:437–456, 2018.
- Wurzenberger JC, et al: Thermal conversion of biomass: comprehensive reactor and particle modeling, *AIChE J* 48(10):2398–2411, 2002.
- Xiong Q, et al: SPH method for two-fluid modeling of particle–fluid fluidization, *Chem Eng Sci* 66:1859–1865, 2011.
- Ye M, van der Hoef MA, Kuipers JAM: A numerical study of fluidization behavior of Geldart A particles using a discrete particle model, *Powder Technol* 139(2):129–139, 2004.
- Yin X, Sundaresan S: Fluid-particle drag in low-Reynolds-number Polydisperse gas-solid suspensions, *AIChE J* 55(6):1352–1368, 2009.
- Yuan C, Fox RO: Conditional quadrature method of moments for kinetic equations, *J Comput Phys* 230(22):8216–8246, 2011.
- Yuu S, Umekage T: Constitutive relations and computer simulation of granular material, *Adv Powder Technol* 19(3):203–230, 2008.
- Zaidi AA, Tsuji T, Tanaka T: A new relation of drag force for high Stokes number mono-disperse spheres by direct numerical simulation, *Adv Powder Technol* 25(6):1860–1871, 2014.
- Zastawny M, et al: Derivation of drag and lift force and torque coefficients for non-spherical particles in flows, *Int J Multiph Flow* 39:227–239, 2012.
- Zhou Q, Wang J: CFD study of mixing and segregation in CFB risers: extension of EMMS drag model to binary gas-solid flow, *Chem Eng Sci* 122:637–651, 2015.
- Zhou ZY, et al: Discrete particle simulation of particle–fluid flow: model formulations and their applicability, *J Fluid Mech* 661:482–510, 2010.
- Zhu L-T, Ye M, Luo Z: Application of filtered model for reacting gas–solid flows and optimization in a large-scale methanol-to-olefin fluidized-bed reactor, *Ind Eng Chem Res* 55:11887–11899, 2016.
- Zick A, Homsy G: Stokes flow through periodic arrays of spheres, *J Fluid Mech* 115:13–26, 1982.